IntechOpen

Powder Technology

Edited by Alberto Adriano Cavalheiro

POWDER TECHNOLOGY

Edited by **Alberto Adriano Cavalheiro**

Powder Technology
http://dx.doi.org/10.5772/intechopen.72370
Edited by Alberto Adriano Cavalheiro

Contributors

Prashantha Kumar H G, Andrei Kolesnikov, Nikolay Alekseev, Andrey Samokhin, Nelly Cecilia Alba De Sánchez, Hector Enrique Jaramillo S., Xizhong An, Yu Liu, Fen Huang, Qian Jia, Ilmars Zalite, Gundega Heidemane, Janis Grabis, Mikhail Maiorov, José Bruno Rojas-Trigos, Yolanda Jiménez-Flores, Víctor Manuel Suárez Quezada, Moseratt Suárez Quezada, Uriel Nogal Luis, Minami Kaneko, Ken Saito, Fumio Uchikoba, Victor Maziuk

Notice

First published in London, United Kingdom, 2018 by IntechOpen
eBook (PDF) Published by IntechOpen, 2019
IntechOpen is the global imprint of INTECHOPEN LIMITED, registered in England and Wales, registration number: 11086078, The Shard, 25th floor, 32 London Bridge Street
London, SE19SG – United Kingdom
Printed in Croatia

British Library Cataloguing-in-Publication Data
A catalogue record for this book is available from the British Library

Additional hard and PDF copies can be obtained from orders@intechopen.com

Powder Technology
Edited by Alberto Adriano Cavalheiro

p. cm.

Print ISBN 978-1-78923-660-6

Online ISBN 978-1-78923-661-3

eBook (PDF) ISBN 978-1-83881-681-0

Meet the editor

Dr. Alberto Adriano Cavalheiro was born in Araraquara, Brazil, in 1969. He graduated and carried out his PhD at the Chemistry Institute of Paulista State University. He is titular professor at Mato Grosso do Sul State University and has a researcher position at the Development Centre in Chemical Technology and in the Postgraduate Program in Natural Resources. Professor Cavalheiro and his research group have concentrated efforts on two fields: phase transition mechanisms through X-ray diffraction and Rietveld refinement and morphological characterization of high-performance adsorbent materials, such as anionic clays. Recently, he began the study of graphene composites with anionic clays to increase the filtration power of contaminated water, aiming at direct human consumption.

Contents

Preface XI

Section 1 Metal and Composite Powders 1

Chapter 1 **Nanopowders Production and Micron-Sized Powders Spheroidization in DC Plasma Reactors 3**
Andrey Samokhin, Nikolay Alekseev, Mikhail Sinayskiy, Aleksey Astashov, Dmitrii Kirpichev, Andrey Fadeev, Yurii Tsvetkov and Andrei Kolesnikov

Chapter 2 **MPFEM Modeling on the Compaction of Al/SiC Composite Powders with Core/Shell Structure 21**
Xizhong An, Yu Liu, Fen Huang and Qian Jia

Chapter 3 **Processing of Graphene/CNT-Metal Powder 45**
Prashantha Kumar HG and Anthony Xavior M

Chapter 4 **Analytical Description of the Pore Structure of Porous Powder Materials 65**
Victor Maziuk

Section 2 Non-Metallic Powders 77

Chapter 5 **Sol-Gel Synthesis of Calcium-Deficient Hydroxyapatite: Influence of the pH Behavior during Synthesis on the Structural, Chemical Composition and Physical Properties 79**
José Bruno Rojas Trigos, Yolanda Jiménez-Flores, Víctor Suárez, Moseratt Suárez-Quezada and Uriel Nogal

Chapter 6 **The Synthesis and Characterization of Nickel and Cobalt Ferrite Nanopowders Obtained by Different Methods 97**
Ilmars Zalite, Gundega Heidemane, Janis Grabis and Mikhail Maiorov

Chapter 7 **Titanium Carbide (TiC) Production by Mechanical Alloying 115**
Héctor Enrique Jaramillo Suárez, Nelly Alba de Sanchez and Julian Arnaldo Avila Diaz

Chapter 8 **Powder Process with Photoresist for Ceramic Electronic Components 133**
Minami Kaneko, Ken Saito and Fumio Uchikoba

Preface

Powder technology is an interdisciplinary area that provides technological solutions to several application fields. Several aspects of powder technology are addressed in the research and development of new materials, especially in engineering and materials science, as a matter of priority. The subject area also covers the physics and chemistry of powders, including synthesis and processing and the consequences of the methodologies used in the final properties of the materials obtained. It also involves other related matters, such as adjustments of equipment design and operation, industrial testing, instrumentation, mathematical modeling, etc. Therefore, the relationship between the various fields of basic and applied science with industrial demands promotes important technological advances.

Powder technology involves several issues, but it focuses on the particulate materials at any stage of production, such as the characteristics of the precursor raw materials, particle size and shape, porosity and specific surface area of the powders, chemical and physical properties in the interface and interphase of components, processes of adhesion and agglomeration, synergy among the phases in composites, compacting, flowing, sintering, and densification processes, parallel reactions during processing, and other properties that influence the final properties of produced materials. The main goal of this book is to outline the current state of the art in powder technology, with emphasis on two generic types of materials: metals and metal-containing composites as well as non-metal materials.

Powder Technology contains eight peer-reviewed chapters organized in two sections. Section 1 contains four chapters concerning metal and metal-containing composites. Chapter 1 presents several results on the synthesis of tungsten and nickel nanopowders by reduction of corresponding oxides in hydrogen–nitrogen and propane–air plasmas. The methodology produces metals with specified properties, including spheroid shapes for nanoparticles, which is of special interest for application in additive technologies.

On the other hand, Chapter 2 describes the use of the multiparticle finite element method as an efficient model to investigate the compaction of aluminum/silicon carbide core–shell composites. Various macro- and microproperties, such as relative density, stress, particle deformation, mass transfer, and interfacial behaviors, were characterized and analyzed. It is shown that the compaction stage follows a densification mechanism driven by particle rearrangement originated from unbalancing low forces among the interparticles. The information available can be a valuable reference for the production of several particulate materials.

In sequence, Chapter 3 reviews methodologies concerning the insertion of graphene and carbon nanotubes in metal matrixes to obtain reinforced composites for industrial applications. The two-dimensional structure and high specific surface area of the graphene make this material type the most appropriate for matrix reinforcements in composite structures, even at very low content addition, mainly if compared to particulate carbon-based materials. It is demonstrated that the use of metallic salts as metallic precursors dissolved into sol-

vents is a good approach to obtain reduced metal nanoparticles deposited on the graphene sheets to form composites directly.

Finally, the section 1 ends with Chapter 4, which introduces theoretical relationships existing between the function of pore distribution and average hydraulic pore size in porous materials, such as the porous bronze alloy. It shows the relationship between the function of pore distribution and average pore size of powder porous materials and how the partial draining of the pore space can affect the calculation of pore size distribution. The true function of pore distribution is obtained as a result of correcting mercury porosimetry data, which are able to improve the calculation accuracies.

Section 2 also contains four chapters, concerning non-metallic powders. Chapter 5 describes the sol–gel synthesis of calcium-deficient hydroxyapatite. In this chapter, the use of different drip rates during synthesis procedures shows the real consequences on the structural, morphological, and textural characteristics of calcium-deficient hydroxyapatite by the precipitation method. The drip rate clearly governs the pH of the suspension during the synthesis process, which leads to significant impacts on the physical–chemical properties of the materials, such as the increasing of calcium and oxygen vacancies in the structure.

This is followed by Chapter 6, which presents the synthesis of single-phase nickel and cobalt ferrite nanopowders through several approaches, such as chemical sol–gel self-propagating combustion, the coprecipitation method, hydrothermal synthesis, the spray-drying method, and high-frequency plasma synthesis. The magnetic properties of synthesized ferrite powders are clearly dependent on the synthesis method, and advantages and disadvantages of each approach are demonstrated concerning the specific surface area and the particle mean sizes, which could be correlated with the measurements of saturation magnetization.

Chapter 7 reports the production of titanium carbide by mechanical alloying and certain aspects of the process are discussed in detail, such as the influence of ethanol as a dispersing liquid, which harms oxygen extraction from the titanium dioxide precursor. It demonstrates the influence of milling time on crystallinity and that the sintering process must be performed to obtain highly densified materials. The low cost of the mechanosynthesis process to obtain titanium carbides from titanium dioxide, graphite, and commercial aluminum precursors opens the possibility of implementing this method as an industrial process.

Section 2 and the book are closed with Chapter 8, which describes the photoresist process combined with both photolithography and printing to produce integrated circuits. Several experimental parameters are changed, such as the conductive and ceramic patterns, use of the photoresist for the mask pattern, and so on. One of those approaches has permitted to achieved the miniature multilayer ceramic inductor that suppresses the minor loop. All of the patterning processes and the fabricated patterns are shown and some adjustments are included in this work as a basis for a new approach to optimization.

The eight chapters in this book each focuses on a particular aspect of the problem, but are able to provide a generic idea of the direction of current and future efforts on the use of particulate materials. Within each chapter, the reader will come into contact not only with different material types, but also with several techniques of synthesis, characterization, and interpretation of results, which can be useful to synthesize and investigate other materials in the form of powder.

Dear reader, with this book you will have access to important subjects on the engineering and science of materials. Chapters can be read in sequence as they are presented or in any sequence that the reader deems appropriate, depending on their priority of interest. You can absorb surprising information, which can be a valuable seed for new and better approaches in the near future. Therefore, you have at hand an excellent book containing several recent topics and the frontier of knowledge on powder technology, which can be consulted not only by experienced researchers but also by students to understand how vast the powder technology area can be.

Alberto Adriano Cavalheiro
State University of Mato Grosso do Sul
Development Centre in Chemical Technologies
Brazil

Section 1

Metal and Composite Powders

Chapter 1

Nanopowders Production and Micron-Sized Powders Spheroidization in DC Plasma Reactors

Andrey Samokhin, Nikolay Alekseev,
Mikhail Sinayskiy, Aleksey Astashov,
Dmitrii Kirpichev, Andrey Fadeev, Yurii Tsvetkov and
Andrei Kolesnikov

Additional information is available at the end of the chapter

http://dx.doi.org/10.5772/intechopen.76262

Abstract

Technology for metal and inorganic compounds nanopowders production in DC arc plasma reactors has been developed. Similar DC arc plasma reactors were used for micron-sized powders spheroidization. Results of experimental studies are presented. Formation of nanoparticles via different mechanisms as well as mass transfer of nanopowders to the reactor cooling surfaces are discussed. Heat flux distribution along the reactor wall and its influence on the evolution of nanoparticles in the deposited layer are investigated. Effects of plasma torch and confined jet reactor operation parameters on the granulometric, phase and chemical composition of nanopowders are discussed. Potential of the confined plasma jet apparatus for micron-sized metal and composite particles spheroidization is demonstrated.

Keywords: thermal plasma, DC arc plasma torch, nanopowder, synthesis, reactor, spheroidization, metals, inorganic compounds

1. Introduction

Nanosized powders of elements and their inorganic compounds are the basis for development of various nanostructured materials. These materials include nanostructured functional ceramics, hard alloys with increased wear resistance and toughness, dispersion hardened and modified structural alloys with enhanced performance characteristics, nanostructured protective

thermo-, corrosion and wear-resistant coatings, polymer composites with fillers and inorganic nanoparticle modifiers for alloys [1–9].

Various techniques are used for nanopowders synthesis, including processing in gas, liquid and solid phases. Such methods employ physical and chemical deposition from gas phase, precipitation from solutions, mechanical grinding, etc. The formation of nanoparticles by homogeneous nucleation in supersaturated vapors followed by nanoparticles growth via condensation and coagulation is the basis of any gas phase nanoparticles manufacturing process. Fast cooling of saturated vapors or gas phase chemical reactions produce supersaturated vapors. Depending on the method used, processes for nanopowders manufacturing in gas phase include flame synthesis, evaporation in high-energy beams (laser radiation, accelerated electrons, focused microwave radiation), and plasmachemical synthesis in DC arc plasma.

Plasmachemical synthesis is the most versatile method for manufacturing of metal and inorganic compounds nanopowders, or nanopowders mixtures using inert, reducing and oxidizing atmospheres with controlled composition. Main advantages of nanopowders plasmachemical synthesis are:

1. Various types of nanopowders (individual elements, compounds and mixtures) can be produced;
2. Physical and chemical characteristics of the nanopowders can be controlled and nanopowders with required parameters (purity, chemical and phase compositions, specific surface) can be produced;
3. Plasma reactors have small dimensions and high production rate;
4. Traditional commonly applied raw materials can be used;
5. Process can be easily scaled-up from laboratory setup to the level of industrial equipment with high productivity.

High efficiency and other technological characteristics of nanopowder production in plasma testify to the competitiveness of the plasma method and wide possibilities for its application. As estimates show, the cost of nanopowders produced using plasma technologies at mass production level should slightly differ from the cost of "traditional" powders of this nomenclature. Plasma technologies can be considered as an effective way of obtaining a wide range of nanopowders. Thermal plasma can be generated using various types of electric discharges [10]. They include DC arc discharge, high-frequency (radio frequency) induction plasma discharge (RF), microwave plasma (UHF), as well as combined discharges.

At present, RF plasma reactors developed and manufactured by TEKNA [11] are widely used for nanopowders production. When operating electrodeless RF and microwave plasmatrons, the impurities (such as electrode's erosion products) in the nanopowders are absent, but it might appear when using DC arc plasma generators. However, it should be borne in mind that the present value of 1 kW of power generated by RF and microwave plasma torches is up to 3 times higher than the cost of plasma generation in DC arc plasma torches [12]. Besides,

the power of modern DC arc plasma torches reaches 3–5 MW with a service life of up to 103 h [13, 14], while the power of existing RF plasmatrons does not exceed 1 MW. The usage of V-shaped DC arc plasmatrons where tungsten electrodes operate in an argon inert gas medium [15] allows to minimize the presence of impurities of the electrode material in the thermal plasma flow and to ensure the production of high-purity target products. Westinghouse Plasma Corporation developed plasmatrons with a power of 300–2400 kW and thermal efficiency of 70–85%. Such devices are used in waste materials processing and metallurgical furnaces operations [14]. DC plasma torches have high energy efficiency and can be used in the realization of high-temperature processes on an industrial scale. This paper provides a review of the research in the field of nanopowders synthesis and processing (spheroidization) of micron sized powders in thermal plasma flows generated by DC arc plasma torches. The research was carried out at the Institute of Metallurgy and Materials Science (IMET RAS) in collaboration with partners over recent years.

2. Plasmachemical reactor

IMET RAS developed DC arc plasma torches with a nominal power of 30–150 kW with self-setting arc length and gas discharge stabilization, as well as plasmatrons with an interelectrode insert. The torches were used for the generation of thermal plasma in IMET laboratories and pilot plants. The plasma torches operated with reducing, oxidizing and inert gases and their mixtures and provided stable generation of plasma jets with an equilibrium temperature of up to 4000–8000 K (for molecular gases) and up to 12,000 K (for monatomic gases). The torches were used for both nanopowder production processes and for spheroidization processes. Plasma synthesis of nanopowders includes a complex set of physicochemical processes occurring in turbulent gas-dispersed non-isothermal flows. At present, plasma reactors with confined jet are widely used for nanopowders production. In confined jet reactor, the plasma jet flows into the volume of the reactor, which is confined by the cooled cylindrical surface. The ratio of the torch nozzle diameter to the reactor's diameter is of the order of 10. The plasma jet can be generated by any type of plasma generator (DC arc discharge, high frequency discharge, microwave discharge). When a plasma jet outflows from plasma torch into reactor's volume, a rapid temperature drop occurs, resulting in supersaturated vapors formation. Vapors condensation leads to the nanoscale particles formation. Evolution of nanoparticles granulometric composition occurs in the reactor's volume because of their condensation and coagulation growth. Phase and chemical compositions of nanoparticles can also change. Control of nanoparticles formation is achieved by variation of such operational parameters as plasma jet chemical composition, enthalpy and flow rate; concentrations of reagents in the reactor; and parameters of the reagents injection into the plasma jet. If solid powder is used as raw material, the initial size of the solid particles has significant effect of nanoparticles formation.

During nanoparticles formation in the volume of plasma reactor, they move toward internal cooled surfaces of the reactor. The layer of nanoparticles is formed at these surfaces. The deposited layer evolution is affected by heat flux from the high temperature gas flow inside

the reactor. The evolution of nanoparticles in the layer is determined by the temperature distribution and lifetime of the layer, and the temperature distribution depends in turn on the temperature of the cooled surface, the density of the mass flux of the deposited nanoparticles, and the density of the heat flux passing through the layer. Under plasmachemical synthesis conditions the layer thickness, as well as its thermal resistance, are increased in time. The unsteady temperature field in the layer can lead to the time changes of the layer's structure, phase and chemical composition. These changes are due to chemical reactions, phase transformations, and particles sintering. All these changes occur when the temperature in the growing layer increases. To obtain the nanopowder with required specifications, where nanoparticles retain the properties determined by the conditions of their formation in the gas stream, it is necessary to exclude or minimize the possibility of physicochemical transformations in the layer of precipitated particles. It is necessary to prevent the layer's temperature rise above certain threshold values. These values are the temperatures of nanoparticles characteristic chemical and phase transformations, and temperatures related to nanoparticles growth due to their contacts in the layer. Nanoparticles are formed in the plasma process inside the reaction zone, but possible nanoparticles transformations in the growing layer on the reactor's surfaces might change the properties of nanoparticles and become a problem. This problem is important for the realization of controlled plasma synthesis of nanopowders with given properties.

An unlimited growth of the nanoparticles layer thickness will inevitably lead to an increase in the layer's temperature resulting in the particles sintering and coarsening, as well as possible change in their phase and chemical composition. These effects will be most pronounced for nanoparticles with a low temperature of possible physicochemical transformations, especially for particles with low melting point. Thus, to obtain the nanopowder with required specifications, the nanoparticles physical and chemical transformations in the deposited layer have to be blocked. To achieve this, the thickness of this layer, formed on the stationary cooled reactor's surface, must be limited to a certain value. For particular target nanoproducts, the size of the precipitating nanoparticles, the initial temperature of the deposition surface and the heat flux density from the high temperature stream to the deposition surface will determine this limiting layer's thickness.

3. Heat transfer to the wall of reactor

The investigations of metal and inorganic compounds nanopowders synthesis included experimental studies of heat and mass transfer in a confined plasma jet reactor [16].

Following topics were studied:

1. heat flux density distribution along the reactor‘s length to the nanoparticle deposition surface
2. mass flux density distribution of deposited nanoparticles along the reactor‘s length

3. physical and chemical properties of nanopowders deposited on the surface in various zones under various process parameters

A cylindrical sectioned plasma reactor with confined jet stream was used. Reactor had diameter and length of 200 and 600 mm correspondently (**Figure 1**) [17]. The length of the sections varied in the range 70–130 mm. DC arc plasma torch with a rated power of 25 kW was used for thermal plasma generation. Nitrogen, hydrogen-nitrogen mixture (22 vol. % H_2), and air were used as plasma-forming gases. The synthesized nanoparticles were deposited on the reactor's walls and partially removed with the exhaust gases into the filtration apparatus.

Figure 1. General view of 30 kW plasma setup.

Following processes were carried out in the reactor:

- Copper nanopowders production via evaporation-condensation of dispersed copper (raw particles less than 40 μm) in a nitrogen plasma;
- Production of tungsten nanopowders by reduction of dispersed tungsten trioxide WO_3 (raw particles less than 40 μm) in hydrogen-nitrogen plasma
- Production of aluminum oxide nanopowders by oxidation of disperse aluminum (ASD-4, raw particles less than 10 μm) in air plasma;
- Production of multicomponent composition in tungsten-carbon system (W-C) via interaction of dispersed tungsten trioxide WO_3 (raw particles less than 40 μm) with methane in hydrogen-nitrogen plasma.

The reactions underlying these processes differ in thermal effects calculated under standard conditions. Copper evaporation-condensation reaction has a zero thermal effect, the reaction of tungsten trioxide reduction by hydrogen is weakly endogenous (0.5 MJ/kg WO_3), and the oxidation of aluminum by oxygen has a strong exogenous character (31 MJ/kg Al).

The experiments were carried out in the following parameters variation range:

Plasma forming gas flow rate	0.85–2 st. m^3/hour,
Plasma torch nozzle diameter	6–12 mm,
Plasma flow enthalpy at the reactor inlet	13–29 MJ/st. m^3,
Plasma flow power	6.6–12.3 kW,
Flow rate of dispersive raw material	1.0–7.0 g/min,
Duration of experiments	5–80 min

It was experimentally observed that when clean (no nanoparticles are present) nitrogen plasma jet enters the reactor, the heat flux density distribution along the reactor's length shows maximum in the attachment region of the high-temperature flow to the reactor wall, which is typical for the separated flows in the channels with sudden expansion. The value of the heat flux density is determined mainly by the plasma flow power at the reactor's inlet and in our experiments it varied in the range 25–45 kW/m^2. The maximum value of the heat flux density exceeds by 2.5–3 times the values at initial and final sections of the reactor. Distribution of normalized heat flux density, i.e. flux related to the magnitude of the maximum, remains practically unchanged in the whole experimental range of input parameters variation (thermal power, flow rate and enthalpy) (**Figure 2A**). The presence of hydrogen in nitrogen practically did not change the heat fluxes values in the reactor. A decrease of the torch nozzle diameter from 10 mm to 6 mm led to the relocation of flow attachment region further downstream from the reactor inlet, and location of maximum wall heat flux changed accordingly.

In experiments when nanopowders of copper, tungsten, and W-C composition were synthesized, it was found that heat flux density distribution along the reactor length also had extremum (**Figure 2B**), as in the case of the flow containing no dispersed particles. But for a two-phase

flow (gas + particles) some increase in the heat flux density at the reactor initial sections was observed. This may be due to the radiation from condensed particles to the wall in the highest temperature zone of the reactor. This zone is located at the initial section of the plasma jet.

When aluminum oxide nanopowder was synthesized by oxidation of aluminum powder in air plasma jet, the significant differences in heat fluxes distribution in comparison with other realized processes were observed (**Figure 3**). With an increase in raw aluminum powder feed

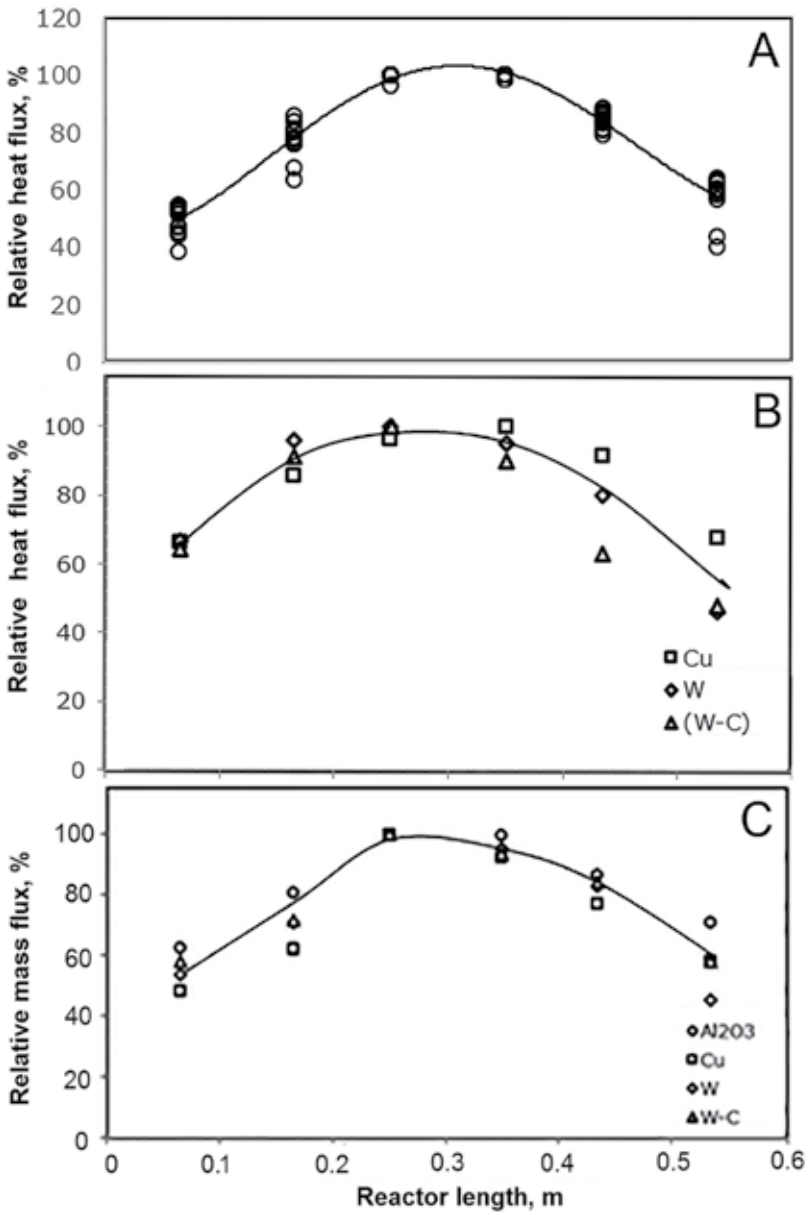

Figure 2. Normalized heat flux and mass flux distributions at plasma reactor wall.

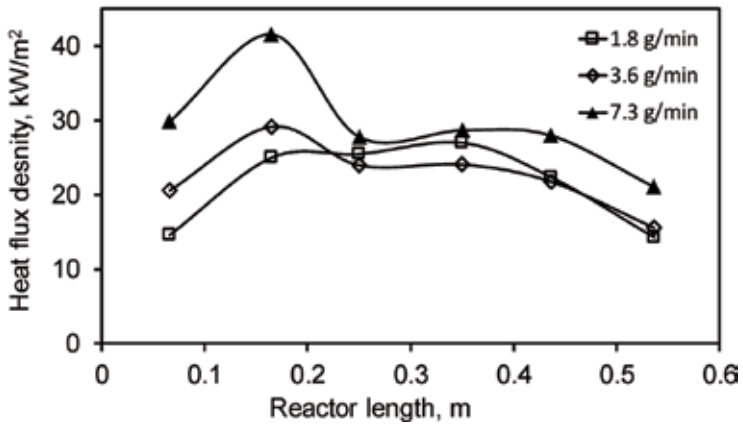

Figure 3. Heat flux density distribution in Al_2O_3 nanopowder synthesis for various Al feed rates.

rate, the maximum heat flux density shifts toward the beginning of the reactor, while its magnitude increases due to additional heat release as a result of the highly exogenous reaction of aluminum oxidation by air oxygen. Depending on the raw material feed rate, the additional power released as a result of this reaction was equal to 10–40% of the plasma jet power. The local heat flux density on the reactor wall in the studied nanopowder syntheses varied in the range 10–40 kW/m^2. It follows from experiments that non-uniform wall heat flux density distribution exists in plasma reactor with a confined jet flow, and the exogenous reactions with a pronounced thermal effect can exert a significant influence on the wall heat flux distribution. Some nanoparticles degradation might occur inside the deposited nanoparticles layer in the area of maximal heat flux.

4. Mass transfer to the wall of reactor and formation of particle's layer

In the near-wall region of the plasma reactor, the nanoparticles transfer occurs under conditions when the average size of the nanoparticles is smaller or commensurable with the mean free path of the gas molecules, so the deposition of nanoparticles onto reactor wall from turbulent non-isothermal flow will be determined by the resulting effect of thermophoresis and Brownian diffusion [18]. The performed experiments have demonstrated that the deposited particles distribution along the reactor length has single extremum (**Figure 2C**), while the location of the maximum particle mass flux density coincides with the location of the maximum heat flux density. A similar particle flux density distribution is observed for all the studied processes, including aluminum oxide synthesis, where heat flux density distribution could have a bimodal character. The mass flow density is determined by the condensed phase mass concentration in the solid–gas flow, with the maximum value of the mass flow density exceeding by up to 2–3 times the mass flow density at the initial and final sections of the reactor.

For all the processes in the studied parameter variation ranges a high degree of nanoparticles deposition on the reactor surface is observed. The deposited mass is equal to 40–80% of the total

http://dx.doi.org/10.5772/intechopen.76262

mass of synthesized nanopowder. Consequently, the final properties of the produced nanopowders are largely determined by the properties of the product that is precipitated exactly in the reactor. The degree of nanoparticles deposition decreases with increasing of the process duration (thickness of the deposited layer of nanoparticles) and with an increase in the raw materials feed rate (processing rate). It follows from analysis of experimentally found heat flux density distributions and mass fluxes density distributions along the reactor wall that the maximum heat flux position coincides with location of maximum mass flux, where growth of the nanoparticle layer occurs at the maximum rate. The effect of heat flux makes possible nanoparticles transformations such as sintering, chemical interaction with the active gaseous medium, and phase transformations most probable exactly in this region of the reactor internal surface.

The layers of deposited nanoparticles had an extremely low bulk density, equal to 3–8% of the theoretical density. The deposited layers thickness varied from 0.05 to 2.7 mm in the experiments. Sintering of deposited nanoparticles near the maximum heat flux density location was noted only for copper nanopowder, where the melting point of the metal is 1360 K. A slight change in the average nanoparticle size inside the deposited layer along the reactor length is noted for other nanopowders (W, Al_2O_3, (W-C)), whose materials have much higher melting point. General list of nanopowder syntheses, performed in confined jet reactor, is given in **Table 1**. Some syntheses (AlN, AlON) were carried out in a combined reactor with disperse raw materials pre-evaporation in a heat-insulated channel followed by gas chemical quenching.

No	Nanopowder	Initial reagents	Plasma forming gas	Properties of nanopowders		
				Phase composition	Specific surface area, m^2/g	Impurities
Metals						
1	W, Mo, Ni, Co, Re	Me_xO_y, H_2, C_3H_8 + air	$H_2 + N_2$, C_3H_8 + air	Me	2–30	[O]
2	Cu	CuCl	$H_2 + N_2$	Cu, Cu_2O, CuO, CuCl	2–5	[Cl], [O]
		$Cu(HCOO)_2$	N_2	Cu, Cu_2O, CuO	2–7	[C]
		$Cu(CH_3COO)_2 \cdot H_2O$	N_2	Cu, Cu_2O, CuO	5–35	[C]
		Cu(re-condensation)	N_2	Cu, Cu_2O, CuO	20–36	[O]
Metal composites						
3	W-Ni-Fe (W – 95 mass %)	WO_3, NiO, Fe_2O_3, H_2	$H_2 + N_2$	W, Ni-Fe	5–12	[O]
4	W-Cu (W - 80 mass %)	WO_3, CuO	$H_2 + N_2$	W, Cu	4–8	[O]
5	Ag-SnO_2	Ag, SnO_2	air	Ag, SnO_2	4–25	
Nitride, carbides, carbonitrides						
6	TiN	Ti, (TiH_2), N_2	N_2	TiN	10–20	$[Ti]_{metal}$
		$TiCl_4$, H_2, N_2	$H_2 + N_2$	TiN	11–39	[Cl]

No	Nanopowder	Initial reagents	Plasma forming gas	Properties of nanopowders		
				Phase composition	Specific surface area, m^2/g	Impurities
7	AlN	Al, NH_3, N_2	N_2	AlN	75–100	$[Al]_{metal}$
8	TiC	$TiCl_4$, H_2, CH_4	H_2 + Ar	TiC	15–45	[Cl]
9	TiCN	$TiCl_4$, H_2, N_2, CH_4	$H_2 + N_2$	TiN	13–23	[Cl]
10	SiC	$SiCl_4$, H_2, CH_4	H_2 + Ar	B - SiC	20–75	[Cl]
11	W – C (C_{total} = 6.2 mass %)	WO_3, CH_4, H_2	$H_2 + N_2$	WC_{1-x}, W_2C, W, C	15–25	
Oxides						
12	Al_2O_3	Al, O_2	Air	$\delta - Al_2O_3$	15–50	
13	Al_2O_3 – MeO (Me = Mg, Co)	Al, Me, O_2	Air	$MeAl_2O_4$ (spinel)	12–16	
14	AlON	Al, NH_3, N_2, O_2	N_2	AlON	20–70	$[Al]_{metal}$
15	TiO_2	$TiCl_4$, O_2	O_2 + Ar	TiO_2 (rutile + anatase)	10–120	[Cl]
16	SiO_2	$SiCl_4$, O_2	O_2 + Ar	amorphous	200–300	[Cl]
17	ZrO_2	$ZrCl_4$, O_2	O_2 + Ar	ZrO_2 (monoclinic + tetragonal)	18–32	[Cl]
18	$ZrO_2 – Al_2O_3$	$ZrCl_4$, Al, O_2	O_2 + Ar	ZrO_2 (tetragonal)	17	[Cl]
19	Y_2O_3	$Y(COOH)_3$, O_2	O_2 + Ar	Y_2O_3 (cubic)	15–25	

Table 1. Nanoparticles syntheses.

5. Particle size distribution and morphology

Granulometric composition is one of the most important nanopowders characteristics, which determines the possibility of their use in solving scientific problems and in practical applications. According to the results of electron microscopy, all nanopowders synthesized in plasma reactor are polydisperse and consist of particles of equiaxial shape (**Figure 4**). The presence of nanoobjects with oriented growth forms is not detected. Formation of nanoparticles under the conditions of plasmachemical synthesis occurs through the macro-mechanisms "vapor–liquid-crystal" (VLC), "vapor-crystal" (VC) and mixed mechanism, including a combination of these mechanisms (VLC-VC). Thermodynamic calculations of the nanopowder equilibrium yield as a function of temperature elucidate the mechanism of nanoparticle formation in a particular process.

Suppose that the substance in question exists in the liquid and solid state, and its yield depends on the temperature. Let us determine T* as the temperature corresponding to the maximum yield of the nanoparticle substance, T_c as the maximum temperature at which the nanoparticle exists in the condensed state, and T_m as the melting temperature of nanoparticle

http://dx.doi.org/10.5772/intechopen.76262

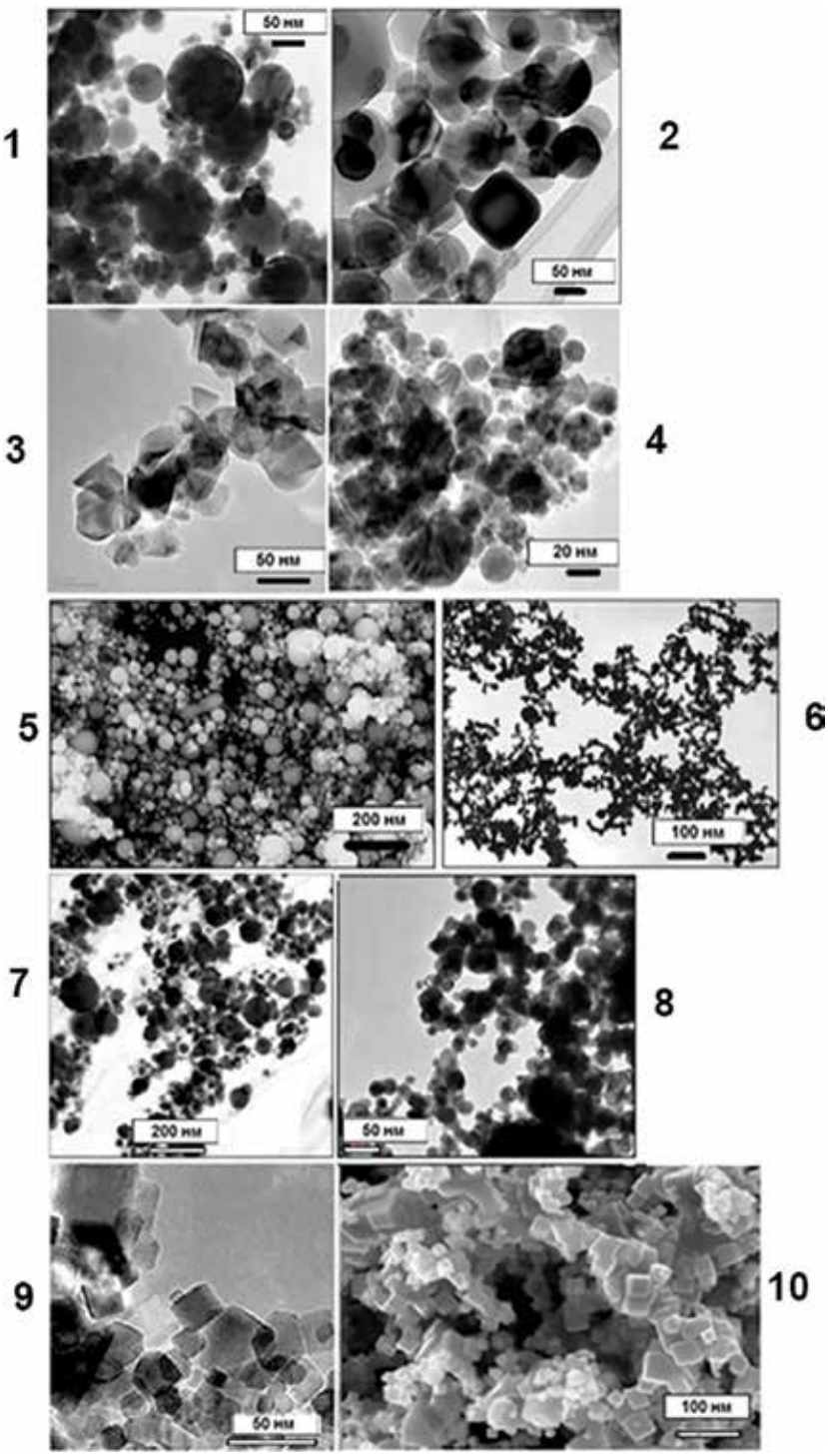

Figure 4. TEM and SEM micrographs. 1—Al_2O_3, 2—TiO_2, 3—SiC, 4—W-C, 5—Cu, 6—W, 7—W-cu, 8—W-Ni-Fe, 9—TiC, 10—TiCN.

matter. Taking into account the fact that the plasma process occurs at a decreasing temperature initially exceeding T_c, the temperature conditions for the nanoparticles formation by the above-mentioned macro-mechanisms can be written as:

mechanism VLC, $T_m < T^* < T_c$, all particles have a spherical habit (**Figure 5a**; **4–1**; **4–5**);

mechanism VC, $T^* < T_c < T_m$, all particles have a faceted habit (**Figure 5b**, **4–2**);

mechanism of VLC-VC, $T^* < T_m < T_c$, particles have both spherical and faceted habit (**Figure 6c**; **4–9**; **4–10**).

The VLC mechanism is realized if, under conditions of a decreasing process temperature, the maximum yield of nanoparticle matter occurs at temperatures above the melting point temperature (**Figure 5a**). The VC mechanism will determine formation of nanoparticles if the formation occurs at the temperatures below the melting temperature of the nanoparticle matter (**Figure 5b**), or the substance does not exist at all in the liquid state.

If during nanoparticles formation temperature is reduced and the substance undergoes crystallization (solidification) before the maximum yield is reached, then nanoparticles formation mechanism changes from VLC to VC, and product will contain both spherical and faceted particles (**Figure 5c**). As follows from the microphotographs of the obtained nanopowders (**Figure 4**), nanoparticles formation in the realized plasma syntheses can occur through all three of these mechanisms (VLC, VC, and VLC-VC). Under plasma synthesis conditions, all of the above mechanisms took place in the formation of Al_2O_3, TiO_2, Cu, W, TiN, TiCN and W-C composition nanoparticles. The micrographs of the nanopowders were used to construct the histograms of the particle size distribution, and statistical analysis was carried out (**Figure 6**) [19].

It was established that the lognormal particle size distribution function (PSDF) reliably (with a correlation coefficient of more than 0.95) describes all the objects under investigation over wide range of changes in the granulometric composition of the investigated nanopowders.

In the PSDF formula d is the diameter of the particle, m is the median of the distribution, and σ is the standard deviation. It should be emphasized, that the validity of lognormal particle size distribution was confirmed earlier for the case of nanopowders obtained in the processes where the formation of particles occurs via coagulation mechanism, i.e. VLC [20]. The experimentally established lognormal particle size distribution in the absence of coagulation growth in accordance

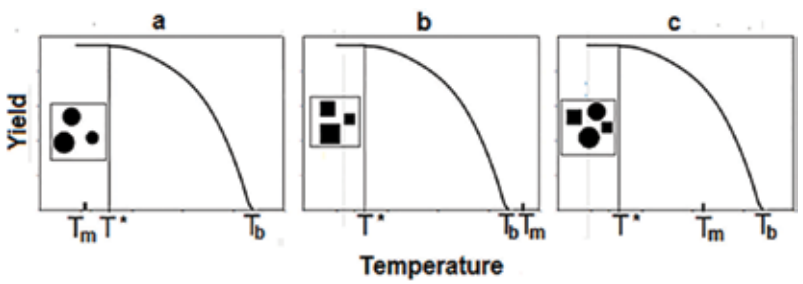

Figure 5. Possible characteristic relations between temperatures, when nanoparticles are formed via different mechanisms.

http://dx.doi.org/10.5772/intechopen.76262

with [21] can be due to the lognormal distribution of the particles residence time in the growth zone. For the nanoparticles syntheses (**Table 1**) where formation of particles occurs through various macro mechanisms, it has been experimentally established that the average size of the nanoparticles increases with increasing concentration of the gas component precursor [22–30].

The effect of the plasma process parameters, as well as effect of the characteristic dimensions of the reactor, was studied in Ref. [24] in case of tungsten and nickel nanopowders synthesis by reduction of WO_3 and NiO oxides in hydrogen-nitrogen and propane-air plasmas. It is shown that the average metal nanoparticle size can be affected by the characteristic dimensions of the

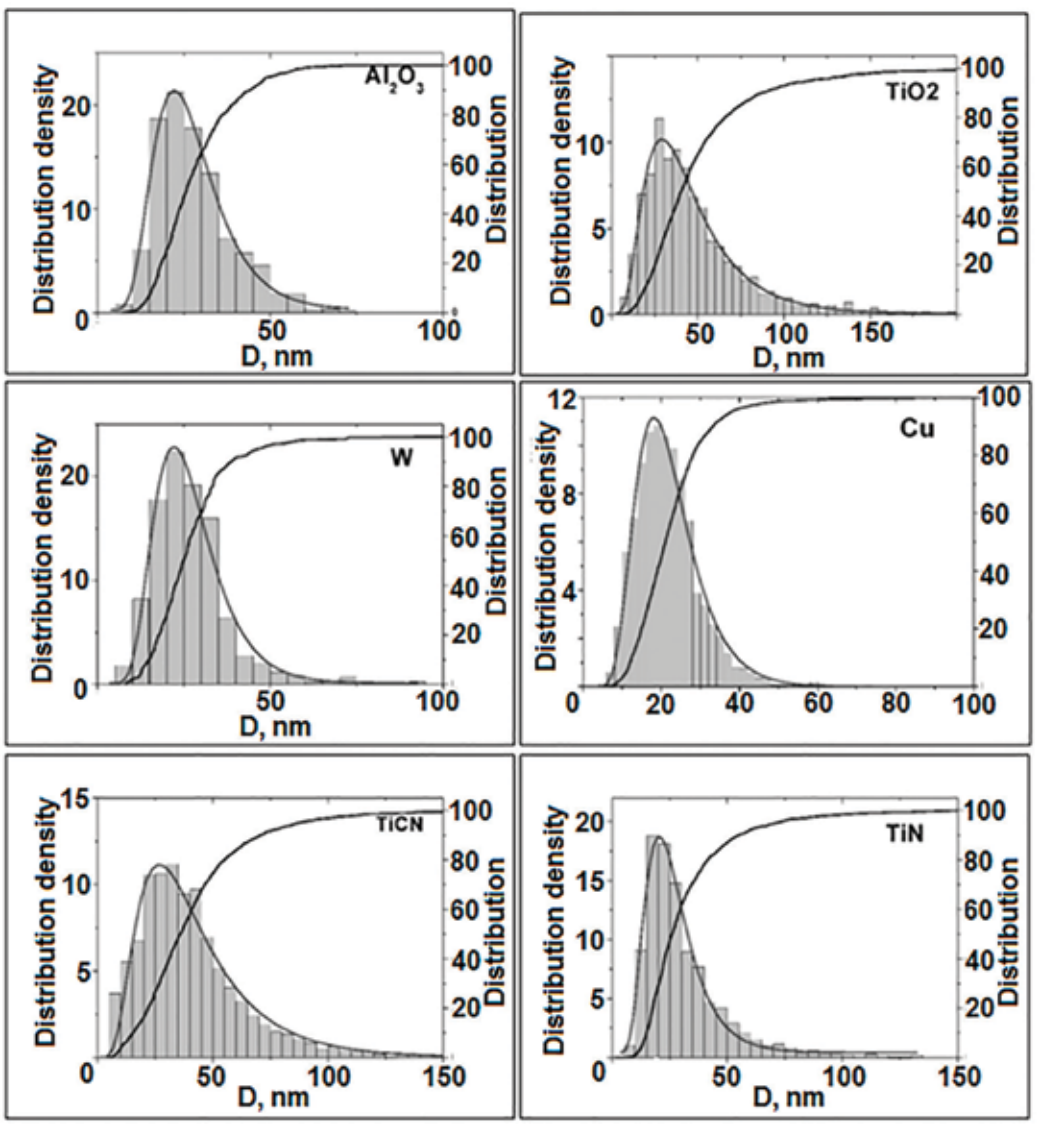

Figure 6. Particles size distributions for Al_2O_3, TiO_2, W, cu, TiCN and TiN nanopowders.

plasma apparatus, such as reactor diameter and plasma torch nozzle diameter. These parameters determine the dimensions of the high-temperature zone where the nanoparticles formation takes place. The chemical processes, occurring at nanoparticle surface, also could influence the regularities of nanoparticle growth. The results of studies of various nanopowders production in the plasma reactor indicate that the influence of the process parameters on the average particle size is a multifactor problem, where the physicochemical features of the process play significant role.

It was found that the average nanoparticle size depends on the synthesis parameters such as the initial precursor concentration, plasma jet enthalpy and velocity. The individual features of the specific process determine the degree of influence of these parameters. Production of nanoparticles of extremely small size in the confined jet reactor can be achieved only if the initial vapor concentration is significantly reduced or the jet velocity is increased. Reducing the initial concentration results in a decrease in the synthesis productivity, and the velocity increase has certain physical and technical limitations. Controlled change of nanoparticles coagulation growth time in the thermal plasma flow manipulates the size of nanoparticles, formed by the VLC mechanism. Additional channel to control the nanoparticle growth time is fast quenching by cold gas injection. Cold gas injection forces cessation of the coagulation growth after completion of vapor–liquid phase transition.

Distributed radial injection of quenching gas was organized at the periphery of the high-temperature flow in the synthesis of alumina nanopowder by oxidation of a metal powder in air plasma flow [25]. Quenching was carried out at the different distances from the reactor inlet, thus varying the particles residence time in the coagulation growth zone. The change of the injection gas flow rate and the injection position allowed the variation of the average particle size in the range of 35 to 75 nm. The obtained results indicate that confined DC plasma jet reactor is capable to produce wide range of individual elements nanopowders as well as nanopowders of inorganic compounds and composites.

6. Spheroidization of metal powders

Spherical powders with a particle size of the order of 10 μm are used as starting materials for the manufacture of products from metals and alloys by the additive technologies methods. Processing of powders with irregular particle shape in thermal plasma flows ensures their fusion, leading to the formation of spherical particles [31].

Titanium powders (fractions of 40–70 μm and less than 40 μm) were processed in the flow of thermal argon plasma, generated by an electric arc plasma torch. The hydrogenation-dehydrogenation process produced raw titanium powders. After plasma processing, the degree of spheroidization has reached 96%. Average sphericity coefficient was equal to 1.01 (**Figure 7**).

Experimental studies of the production of nonporous spherical powders of multicomponent metal alloys have been performed. Ultrafine powder compositions of alloy components, having a particle size of less than 1 μm, have been used as raw material. Model high-alloy Fe-Ni-Cr alloy particles were used as example, and spherical alloy powders with particle sizes in the range from 25 to 50 μm were produced.

http://dx.doi.org/10.5772/intechopen.76262

The process consisted of the following stages: microgranulation of ultrafine powder, heat treatment of microgranules (drying at 100°C, removal of organic binder at 300°C, thermochemical treatment in H_2 at 1000°C, vacuum treatment at 1200°C), classification of heat-treated microgranules with separation of microgranules fraction in the range 25 to 50 μm, spheroidization of the isolated fraction of microgranules in the thermal plasma flow, separation of

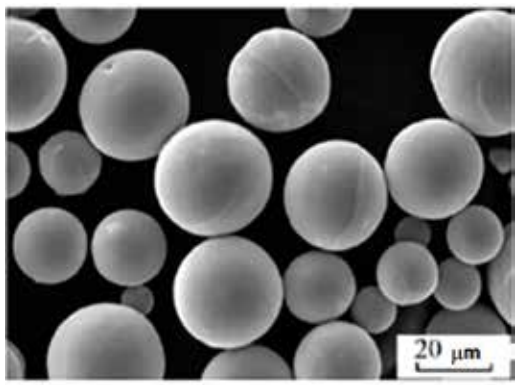

Figure 7. Micrographs of spheroidized titan powder.

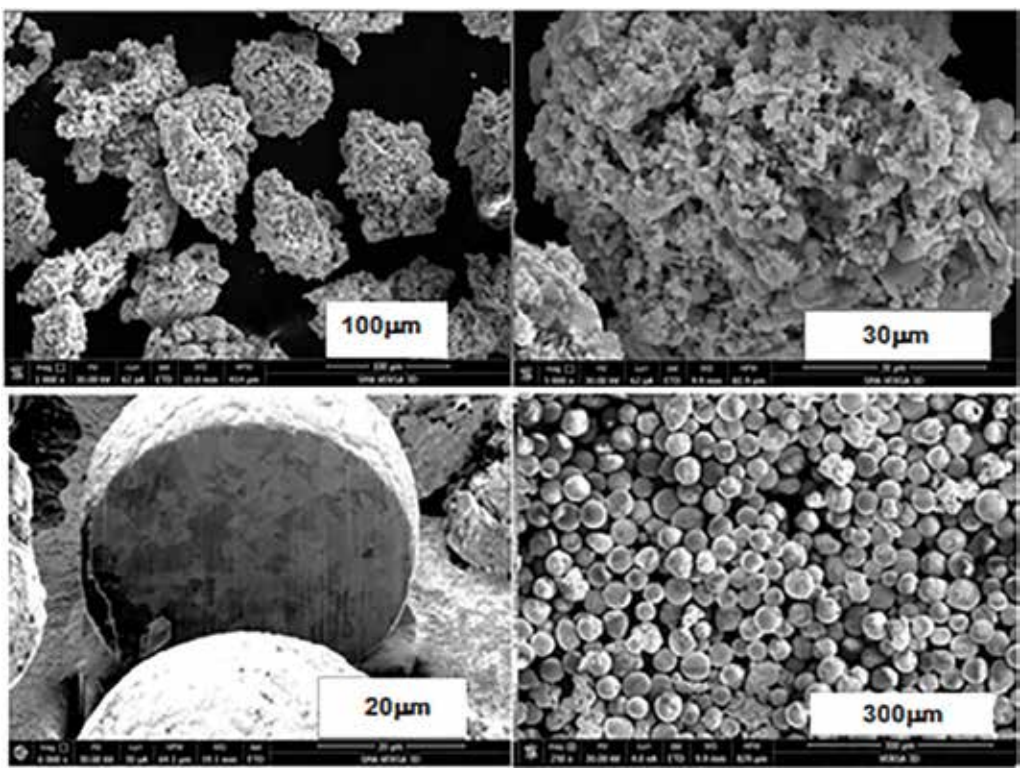

Figure 8. Micrographs of granules. (A) – Initial alloy components, (B) – Spheroidized in plasma.

the micron and submicron fraction. Micrographs of the alloy components microgranules and particles, spheroidized in the plasma flow, are shown in **Figure 8**. The presented experimental results indicate the possibility of metallic and alloys powders spheroidization in a confined DC plasma jet apparatus using various initial powder materials.

7. Conclusion

The presented results of research and development testify to the wide possibilities of plasma processes and devices for obtaining nanopowders of metals and their various inorganic compounds with specified properties. The nanopowders, produced in the plasma reactors, were used in various R&D projects aimed at creation of new materials with special and improved properties. Along with the production of nanopowders, the same plasma reactor with confined jet provides the possibility of metal and alloys powders spheroidizing for their application in additive technologies. The accumulated experience is the basis for the creation of efficient industrial production of powders using plasma reactors based on DC arc plasma torch.

Acknowledgements

This work was supported by the Fund of Applied Researches, Ministry of Education and Science of the Russian Federation (unique identifier of the project RFMEFI57816X0216).

Author details

Andrey Samokhin[1], Nikolay Alekseev[1], Mikhail Sinayskiy[1], Aleksey Astashov[1], Dmitrii Kirpichev[1], Andrey Fadeev[1], Yurii Tsvetkov[1] and Andrei Kolesnikov[2]*

*Address all correspondence to: avkolesnikov@yahoo.com

1 A. Baikov Institute of Metallurgy and Materials Science (IMET RAS), Moscow, Russia

2 Tshwane University of Technology (TUT), Pretoria, South Africa

References

[1] Gogotsi Y, editor. Nanomaterials Handbook. 2nd ed. Boca Raton: CRC Press; 2006. p. 682

[2] Koch CC, editor. Nanostructured Materials: Processing, Properties and Applications. 2nd ed. Norwich: William Andrew; 2006. p. 784

[3] Wang ZL, Liu Y, Zhang Z, editors. Handbook of nanophase and nanostructured materials. vol. IV, Berlin: Springer; 2002. p. 1200

[4] Shaw D, Liu B, editors. Handbook of Micro and Nanoparticle Science and Technology. Berlin: Springer Verlag; 2007. p. 2400

[5] Hosokawa M, Nogi K, Naito M, Yokoyama T, editors. Nanoparticle Technology Handbook. 2nd ed. Amsterdam: Elsevier; 2008. p. 730

[6] Liu LJ, Bashir S. Advanced Nanomaterials and Their Applications in Renewable Energy. Amsterdam: Elsevier Science; 2015. p. 436

[7] Gromov AA, Korotkikh A G, Il'in A, DeLuca LT, Arkhipov VA, Monogarov KA, Teipel U. Nanometals: Synthesis and Application in Energetic Systems. In: Energetic nanomaterials: Synthesis, characterization, and application. Amsterdam: Elsevier Science; 2016. p. 47-63. DOI: 10.1016/B978-0-12-802710-3.00003-9

[8] Altavilla C, Ciliberto E, editors. Inorganic Nanoparticles: Synthesis, Applications, and Perspectives. Boca Raton: CRC Press; 2010. p. 576

[9] Andrievski RA. Nanomaterials based on high-melting carbides, nitrides and borides. Russian Chemical Reviews. 2005;**74**:1061-1072 https://doi.org/10.1070/RC2005v074n12ABEH001202

[10] Toumanov YN. Plasma, High-Frequency, Microwave and Laser Technologies in Chemical and Metallurgical Processes (in Russian). Moscow: Fizmatlit; 2010. p. 968

[11] TEKNANO Nanopowder Synthesis Systems. 2016. Available from http://www.tekna.com/nanopowder-synthesis-systems

[12] Roth JR. Industrial Plasma Engineering, Volume 1: Principles. Boca Raton: CRC Press; 1995. p. 339

[13] Zhukov MF, Zasypkin IM, Timoshevskii AN, Mikhailov BI, Desyatkov GA. Electric Arc Generators of Thermal Plasma (in Russian). Nauka: Novosibirsk; 1999. p. 712

[14] Plasma Torches by Westinghouse Plasma Corporation. 2005. Available from https://www.academia.edu/24044626/Plasma_Torches_by_Westinghouse_Plasma_Corporation

[15] Mikhailov BI. Electric-arc plasmachemical reactors of separated, single-chamber, and combined types. Thermophysics and Aeromechanics (Teplophysica i aeromekhanika). 2010;**17**(3):425-440

[16] Samokhin AV, Astashov AG, Alekseev NV, Tsvetkov YV. Characteristics of heat and mass transfer to the wall of a confined-jet plasma flow reactor in the processes of nanopowder preparation from metals and their compounds. Nanotechnologies in Russia. 2016;**11**(1-2):57-62. DOI: 10.1134/S1995078016010134

[17] Alekseev NV, Samokhin AV, Tsvetkov YuV. Plasma plant for manufacturing of nanodispersed powders (in Russian). RF Patent No 2311225. 2007

[18] Mädler L, Friedlander SK. Transport of nanoparticles in gases: Overview and recent advances. Aerosol and Air Quality Research. 2007;**7**(3):304-342. DOI: 10.4209/aaqr.2007.03.0017

[19] Sinayskiy MA, Samokhin AV, Alekseev NV, Tsvetkov YV. Extended characteristics of dispersed composition for nanopowders of plasmachemical synthesis. Russian Nanotechnologies. 2016;**11**(11-12):110-115. DOI: 10.1134/S1995078016060185

[20] Granqvist CG, Buhrman RA. Ultrafine metal particles. Journal of Applied Physics. 1976;**47**:2200-2219. DOI: 10.1063/1.322870

[21] Kiss LB, Soderlund J, Niklasson GA, Granqvist CG. New approach to the origin of lognormal size distributions of nanoparticles. Nanotechnology. 1999;**10**:25-28. DOI: 10.1088/0957-4484/10/1/006

[22] Alekseev NV, Balikhin IL, Kurkin EN, et al. Formation of ultrafine aluminum oxide powder in confined air plasma jet (in Russian). Fizika I Khimiya Obrabotki Materialov (Physics and Chemistry of Materials Processing). 1994;**4-5**:72-78

[23] Alekseev NV, Balikhin IL, Kurkin EN, Samokhin AV, Troitskaya EV, Troitskii VN. Synthesis of titanium nitride and carbonitride ultradisperse powders in nitrogen plasma jet (in Russian). Fizika I Khimiya Obrabotki Materialov (Physics and Chemistry of Materials Processing). 1995;**1**:31-39

[24] Alekseev NV, Samokhin AV, Grechikov MI. Controlling the granulometric composition of the metal powders produced in plasma reduction processes (in Russian). Fizika I Khimiya Obrabotki Materialov (Physics and Chemistry of Materials Processing). 1997;**6**:54-60

[25] Alekseev NV, Samokhin AV, Kurkin EN, Агафонов КН, Tsvetkov YV. Synthesis of alumina nanoparticles by metal oxidation in thermal plasma flows (in Russian). Fizika I Khimiya Obrabotki Materialov (Physics and Chemistry of Materials Processing). 1997; **3**:33-39

[26] Alekseev NV, Samokhin AV, Tsvetkov YV. Synthesis of titanium carbonitride nanopowder by titanium tetrachloride processing in hydrocarbon-air plasma. High Energy Chemistry. 1999;**33**(3):194-197

[27] Kolesnikov A, Alexeev N, Samokhin A. Controlled synthesis of alumina nanoparticles in a reactor with self-impinging plasma jets. International Journal of Chemical Reactor Engineering. 2007;**5**:A95. DOI: 10.2202/1542-6580.1521

[28] Samokhin AV, Polyakov SN, Astashov AG, Alekseev NV, YuV T. Simulation of nanopowders synthesis in a jet type reactor. II. Formation of nanoparticles (in Russian). Fizika I Khimiya Obrabotki Materialov (Physics and Chemistry of Materials Processing). 2014;**3**:12-17

[29] Samokhin AV, Sinayskiy MA, Alekseev NV, et al. Synthesis of nanoscale zirconium dioxide powders and composites on their basis in thermal DC plasma. Inorganic Materials: Applied Research. 2015;**6**:528-535. DOI: 10.1134/S2075113315050172

[30] Kotlyarov VI, Beshkarev VT, Kartsev VE, et al. Production of spherical powders on the basis of group IV metals for additive manufacturing. Inorganic Materials: Applied Research. 2017;**8**(3):452-458. DOI: 10.1134/S2075113317030157

[31] Samokhin AV, Fadeev AA, Sinayskiy MA, et al. Fabrication of high-alloy powders consisting of spherical particles from ultradispersed components. Russian Metallurgy (Metally). 2017;**7**:547-553. DOI: 10.1134/S0036029517070138

Chapter 2

MPFEM Modeling on the Compaction of Al/SiC Composite Powders with Core/Shell Structure

Xizhong An, Yu Liu, Fen Huang and Qian Jia

Additional information is available at the end of the chapter

http://dx.doi.org/10.5772/intechopen.76563

Abstract

Uniaxial die compaction of two-dimensional (2D) Al/SiC core/shell (core: SiC; shell: Al) composite powders with different initial packing structures was numerically reproduced using DEM-FEM coupled MPFEM modeling from particulate scale. The effects of external pressure, initial packing structure, and SiC content on the packing densification were systematically presented. Various macro and micro properties such as relative density and distribution, stress and distribution, particle rearrangement (e.g. sliding and rolling), deformation and mass transfer, and interfacial behavior within composite particles were characterized and analyzed. The results show that by properly controlling the initial packing structure, pressure, and SiC content, various anisotropic and isotropic Al/SiC particulate composites with high relative densities and uniform density/stress distributions can be obtained. At early stage of the compaction, the densification mechanism mainly lies in the particle rearrangement driven by the low interparticle forces. In addition to sliding, accompanied particle rolling also plays an important role. With the increase of the compaction pressure, the force network based on SiC cores leads to extrusion on Al shells between two cores, contributing to mass transfer and pore filling. During compaction, the debonding between the core and shell of each composite particle appears and then disappears gradually in the final compact.

Keywords: Al/SiC composite powders, compaction, core/shell structure, MPFEM modeling, debonding and rebonding

1. Introduction

Among the advanced particulate reinforced metal matrix composites (PRMMCs), Al/SiC composite is the most commonly studied one due to its potentially high tensile strength and

elastic modulus at room or elevated temperatures, low thermal expansion coefficient, high thermal and electrical conductivity, excellent corrosion resistance, good wear resistance, mechanical properties, ductility, low cost and wide range of applications [1–3]. Normally, two routes (i.e. powder metallurgy (PM) and melt based approach) are used to fabricate PRMMCs with 'net shape' or 'near-net shape' forming. In the fabrication of Al/SiC composites via a melt process, SiC often reacts with molten Al to degrade the reinforcement strength and the interfacial strength [4], and the uniform distribution of SiC particles especially those with nanosizes are difficult to be realized. This deficiency can be largely avoided by PM process which can offer more control over reinforcement distribution and require less energy input than the conventional foundry route. A common PM process of Al/SiC composite consists of cold compaction in a closed-die or in an isostatic pressing followed by sintering. To fabricate Al/SiC composites with superior performances, large amount of physical and numerical work was carried out using PM method in the past few decades.

Physically, many researchers studied the effects of SiC content and particulate sizes using various forming methods. Ling et al. carried out experiments to study the PM fabrication of Al/SiC composites with SiC content ranging from 0 to 30 vol.% (volume fraction), where four PM methods (such as sintered, cold isostatic pressed (CIPed) and sintered, hot isostatic pressed (HIPed), and sintered plus HIPed in the same HIP cycle) were considered and the results of relative density, mechanical properties, and fractography were characterized and compared [1]. They found that the sintered plus HIPed technique can yield the best bulk composites. When the SiC content is within 10 vol.%, the matrix is more likely suffered to ductile failure. With a higher SiC content, the factors such as the interfacial bond strength, pore structure evolution, and the cracking within particles can all determine the mechanical properties of the composite products. For the Al/SiC composite powder comprising 40 vol.% SiC, Sridhar and Fleck respectively performed isostatic and closed-die compaction [5]. They found that for a given SiC powder content, the compaction pressure to achieve a given relative density increases with the decrease of the SiC particle size. The measured yield surfaces after each compaction indicated that the shape depends on the deformation path, with greatest hardening along the loading direction. Tavakoli et al. [2] studied the consolidation behavior of Al/SiC composite powders (with reinforcement SiC up to 50 vol.%) during pressure cycling (ranging from 90 to 360 MPa with 1 Hz) at room temperature in uniaxial compaction experiments to address the effects of compaction mode and SiC content on the densification, microstructure and mechanical properties of Al/SiC composites. And corresponding comparisons were made with monotonic compaction. The results showed that the pressure cycling can enhance the densification of Al/SiC composite powder, and the densification rate increases with the SiC content. Using HIP, Tang et al. [6, 7] studied the consolidation of Al/SiC composite powder with 6.5 vol.% nano-sized SiC particles (25 nm in size) synthesized via cryomilling and followed by hot rolling. Microstructural investigation indicated that the nano-sized SiC particles had been dispersed homogeneously in the reinforced regions in the composites and the tensile strength of the composite was improved greatly. However, coarse-grained SiC_p-free regions were observed to be formed during HIPing, which improved the ductility but to a certain degree decreased the strength. In short, SiC nanoparticles located at grain boundaries can contribute to limiting grain growth, but it is difficult to achieve the complete uniform

distribution of nano SiC particles. Jamaati et al. [8] investigated the effects of SiC particle size (2 and 40 μm, respectively) on microstructure and mechanical properties (tensile strength and elongation) of Al/SiC (with 10 vol.% SiC) composite fabricated by accumulative roll bonding. It was found that the composite strip with 40 μm particle size became uniform with high bonding quality and without any porosity sooner than the strip of 2 μm particle size. For both sizes, different cycles could lead to different tensile strength and tensile elongation.

To determine the compressibility behavior of Al-Cu/SiC composite powder mixtures which include 4 wt.% (weight fraction) Cu and 5–20 wt.% SiC, a double action die compaction with the pressure ranging from 50 to 450 MPa was performed by Ghiţă and Popescu [9]. And empirical equations were proposed to describe densification mechanism of the composite powders and predict the optimal pressure applied. Li et al. [10] carried out physical experiments to study the distributions of SiC particles in different positions of the Al/SiC composite samples (with 35 vol.% SiC) formed by equal channel angular pressing and torsion (ECAPT) and found that the shear strain could create significant influences. And from the compaction stage to the angular pressing stage during ECAPT, the distribution homogeneity of SiC particles increases greatly, implying that this forming method can realize relatively homogeneous SiC distribution. With the addition of nanosized SiC particles (0–7 wt.%), Moazami-Goudariz and Akhlaghi [11] conducted physical experiments on the compaction of Al/SiC composites. In their work, the effects of morphology, microstructure, size, apparent density, flowability, and hardness of the produced powder mixtures on their compaction behavior were investigated. The results showed that the chemical composition and the nano SiC content created effects on the compaction behavior as well as properties of the compact. Al/SiC composites with different contents (up to 15 vol.%) and sizes (3, 6, and 11 μm) of SiC particles were fabricated using conventional PM route [12], where the effects of the size and content of SiC particulates on the microstructural and corrosion behavior of the composite were studied. Meanwhile, El-Kady and Fathy [13] also studied the effects of SiC particle size (70 nm, 10, and 40 μm) and content (5 and 10 wt.%) on both physical and mechanical properties of Al/SiC nanocomposites produced with PM followed by hot extrusion. Majzoobi et al. [14] investigated the tribological properties of Al/SiC nanocomposite prepared by hot dynamic compaction (with the strain rate of 10^3 s^{-1}), where the content of SiC nanoparticles was respectively 0, 5, and 10 vol.%. After compaction, the relative density of the composite compact can be up to 98%.

Recently, the mechanical properties and corrosion behavior of Al/SiC (comprising 20 vol.% SiC) composites fabricated by vacuum hot pressing sintering at 700°C under a pressure of 20 MPa were studied by Zhang et al. [15], in their work the high relative density of 99.65 ± 0.08% for the Al/SiC composite can be obtained. Cold isostatic compaction of Al/SiC composite powders with different content of nano SiC particulates as the reinforcement was experimentally performed by Bajpai et al. [16], where various properties such as hardness, density, porosity, compressive strength, indirect tensile strength and the microstructure of the samples were measured and characterized. The micrograph shows the uniform distribution of nano SiC particles in the aluminum matrix. With micro wave sintering and hot extrusion, Penchal Reddy et al. [17] fabricated nano-sized SiC (0, 0.3, 0.5, 1.0 and 1.5 vol.%) reinforced Al metal matrix composites and studied the structural, mechanical and thermal properties of the developed Al/SiC nanocomposites. Results indicated that hot extruded

Al/SiC nanocomposites (with 1.5 vol.% SiC) exhibited the best mechanical and thermal performance as compared to the other developed Al/SiC nanocomposites.

Aforementioned researches in physical experiments indicate that most of the previous work was mainly focusing on the sintering stage or the forming stage, comprehensive studies on the compaction of Al/SiC composite powders are less conducted. Actually, most of the densification takes place in the compaction stage by rate-independent plasticity [1]. And the relative density (defined as the volume of the powder divided by the volume occupied by the die) and corresponding packing structure of the compact can determine the subsequent sintering process as well as the final properties of the sintered component. Therefore, the researches on the compaction of Al/SiC composite powders when subjected to external energy have increasingly attracted the materials scientists and engineers' interests in the past few years. Nevertheless, even though physical experiments can reproduce the relationship between relative density and compaction pressure and/or temperature, they are unable to quantitatively characterize the local density distribution, stress distribution, and particle motion behavior for pore (or void) filling in situ, especially the nonlinearity features in geometry, materials, and contact during compaction all increase the difficulties of physical experiments [18–22]. Most importantly, it's really hard for researchers to accurately control the uniform distribution (ordered or disordered) of reinforcement (SiC) in the metal (Al) matrix, these disadvantages in physical experiments can be conquered by the so called numerical simulations.

Numerically, various models or methods were proposed or used to simulate powder compaction densification in PM process. For example, a traditional macro continuous FEM (finite element method) simulation model, in which the powder mass is regarded as a continuum with uniform void distribution, was proposed to solve the problems arising from physical experiments. In addition to the relationship between overall relative density and compaction pressure, this method can also be used to analyze local relative density and distribution, stress distribution, and powder displacement in the compact upon compaction from macro continuous scale. Therefore, as reported in the authors' previous researches, the single-action die compaction of pure metal powders [23, 24] and composite powders [25] has been systematically investigated by this method. Even though the traditional FEM can to some extent solve the problems in physical experiments, it is really hard to deal with the important issues like dynamics and contact mechanics from particulate scale based on the aforementioned continuum assumptions. However, this will be overcome by molecular dynamics based DEM (discrete element method) simulation. DEM has been widely applied to generate various packing structures of spherical and non-spherical particles [26–29], but its effectiveness in modeling the compaction of powders is restricted to limited relative density (e.g. $\rho < 0.85$) [30]. For higher relative density and extra large plastic deformation in PM compaction, a new method MPFEM (multi-particle FEM) has been developed and successfully applied in modeling this process [31–43], but less work was conducted on the compaction of Al/SiC composite powders from particulate scale. Recently, using MPFEM the authors successfully modeled the single action die compaction of Al/SiC composite mixtures [44], and the results show that the packing state, size and number of SiC particles in the initial packing structure can significantly influence not only the densification of the Al/SiC composite powders upon compaction but also the properties of the compacts. Even though our previous numerical simulation can reproduce the compaction of

Al/SiC binary powder mixtures, there are still some problems left unsolved, which include: (1) it's really difficult to precisely control the distribution of SiC reinforced particles; (2) it cannot realize full densification especially when SiC particles formed agglomeration or clusters; (3) the local density and stress distributions in the compact are non-uniform. With these problems, a new binary Al/SiC composite constructed by the compaction of powders with core (SiC)/shell (Al) structures were designed and the whole process was simulated by MPFEM method from particulate scale. Currently, no relative literature has been found.

In this chapter, uniaxial die compaction of Al/SiC composite core/shell powders with different initial packing structures was numerically reproduced using DEM-FEM coupled MPFEM modeling from particulate scale. The effects of external pressure, initial packing structure, and SiC content (composition) on the packing densification were systematically presented. Various macro and micro properties such as relative density and distribution, stress and distribution, particle rearrangement (e.g. sliding and rolling), deformation and mass transfer, and interface behavior between particles were characterized and analyzed. Some interesting results have been obtained, which can provide the materials scientists and engineers with valuable references to the realization of fully dense and high performance Al/SiC composite compacts in PM production.

2. Simulation method and conditions

2.1. Simulation method

The simulation method used in current work is MPFEM. In this method, the initial random powder packing is firstly generated by DEM and then imported into FEM model, where each particle is fully discretized into finite element meshes. **Figure 1** respectively gives the schematic diagram of an individual composite particle with core/shell structure and corresponding mesh division as well as the numerically generated initial packing structure in the closed die before compaction when the SiC content is 25 vol.%, where each core (SiC)/shell (Al) composite particle includes respectively 200/1700 nodes and 173/1552 elements. After all the parameters and conditions are determined, the program will be complied and run in the commercialized MSC.Marc software. For simplicity, the details of DEM model are not given here, interested readers can refer to [26–29, 45] for more information. In comparison, each initial ordered binary packing is generated by the intrinsic function in MSC.Marc software based on geometry. The initial random or ordered packing structure was then imported into MPFEM model as the input. **Figure 2** shows the packing morphologies of Al/SiC composite powders before compaction. Here three initial ordered packings, i.e. simple cubic (SC), hexagonal close packed (HCP) and honeycomb structures are considered. The composition of the composite powder can be adjusted by the thickness of Al shell, which is represented by $R - r$, where R and r are respectively the radius of the composite Al/SiC particle and the radius of SiC particle therein. It needs to clarify that the SiC content used in this chapter all refers to volume fraction. For each initial packing structure before compaction, corresponding parameters such as the size ratio between the radius of SiC particle and the radius of the whole composite particle (r/R), SiC content (vol.%), and packing density (or relative density) are listed in **Table 1**.

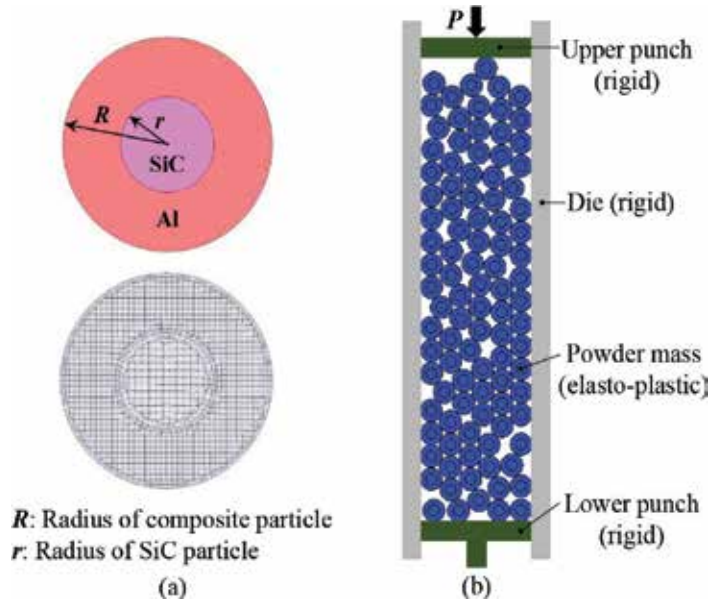

Figure 1. (a) Schematic diagram of an individual Al/SiC composite particle with core/shell structure and mesh division used in MPFEM simulation; (b) DEM generated initial packing structure in a closed die before compaction with 25% SiC.

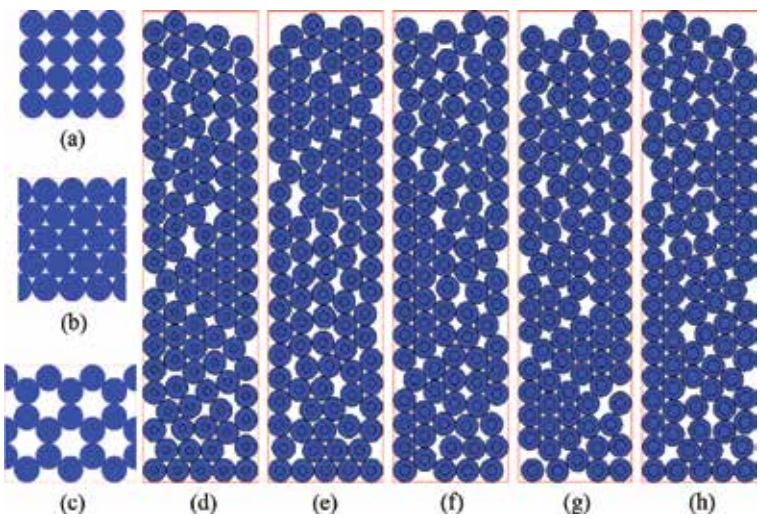

Figure 2. Initial packing structures of Al/SiC composite particles before compaction, where: (a) SC packing; (b) HCP packing; (c) honeycomb packing; (d)–(h) represent random packings with the SiC content of 10, 15, 20, 25, and 30% in volume fraction.

2.2. Simulation conditions

After the generated binary initial packing structure was imported into the MPFEM model in MSC. Marc software, the simulation conditions including material properties, definition of contact,

Initial packing structure	Size ratio (*r*/*R*)	SiC content, vol.%	Packing density
SC	1/2	25	0.7841
SC	2/3	44.4	0.7842
HCP	1/2	25	0.8782
HCP	2/3	44.4	0.8783
Honeycomb	1/2	25	0.6045
Random	1/√10	10	0.7516
Random	√15/10	15	0.7526
Random	1/√5	20	0.7544
Random	1/2	25	0.7424
Random	√3/√10	30	0.7515

Table 1. Corresponding parameters for initial packing structures of composite powders before compaction.

mesh adaptability, and loading cases etc. were then set. In the simulation, the power law model is used to describe the properties of aluminum materials and the yield stress is given by:

$$\sigma_y = \mathrm{A}\left(\varepsilon_0 + \bar{\varepsilon}\right)^{\mathrm{m}} + \mathrm{B}\,\dot{\bar{\varepsilon}}^{\mathrm{n}} \tag{1}$$

where A, B, m, n are material constants; ε_0 is the initial yield strain; $\bar{\varepsilon}$ is the equivalent strain; $\dot{\bar{\varepsilon}}$ is equivalent strain rate. Initially, $\bar{\varepsilon}$ and $\dot{\bar{\varepsilon}}$ are assumed to be zero. Therefore, the initial yield strain can be expressed as:

$$\varepsilon_0 = (E/\mathrm{A})^{1/(\mathrm{m}-1)} \tag{2}$$

where E is Young's modulus. The equivalent strain rate is:

$$\dot{\bar{\varepsilon}} = \left[2/3(\varepsilon_{\mathrm{ij}}\,\varepsilon_{\mathrm{ij}})\right]^{1/2} \tag{3}$$

where $\varepsilon_{\mathrm{ij}}$ is the strain tensor. The material parameters and modeling parameters are respectively given in **Tables 2** and **3**. Here, SiC material was assumed to be elastomer due to its high hardness compared with Al. In the simulation, the upper punch is movable, while the lower

Materials	Young's modulus, *E*/GPa	Poisson's ratio, ν	Strength coefficient, A/MPa	Work hardening index, m
Al	70.00	0.33	225.90	0.05
SiC	470.00	0.142	Elastic-perfectly	

Table 2. Materials parameters used in the simulation.

Contact definition	Loading setup	Operation conditions
Particles: deformable	Iteration method: full Newton-Raphson algorithm	Friction: modified Coulomb friction model
Die and punches: rigid	Convergence criteria: displacement or residual stress control	Large deformation: updated Lagrange function
Friction coefficient between particles: $\mu = 0.2$	Global mesh self-adaptive division: for Al part	Contact method: segment to segment method
Upper punch: velocity control ($v = 1$ mm/s)		

Table 3. Modeling parameters used in the simulation.

punch and the die are fixed. During compaction, the relative density of the compact is calculated by the displacement of the upper punch, and it is not influenced by the strain rate because the materials are set to be not sensitive to this parameter. Meanwhile, each Al granular mesh was set to global mesh self-adaptive to guarantee the accuracy of simulation results. Once all the simulation parameters are determined, the job will be submitted to the server for running.

3. Results and discussion

3.1. Compaction process and property characterization

In PM production, the relationship between the relative density ρ and the pressure P during compaction is always firstly concerned. Here, the compaction curves ($\rho - P$ relations) for different ordered packings of composite Al/SiC powders are shown in **Figure 3**, where the inset images demonstrate the morphologies of the compacts at different compaction stages (marked by A, B, and C) with honeycomb initial packing structure. As can be seen that before compaction, different ordered packing structures correspond to different initial relative densities. For SC and HCP initial packings, both the relative densities increase smoothly with the compaction pressure to a high value. While for the compaction on honeycomb initial packing, the fluctuation of relative density during pressing can be observed when the pressure is very low. This can be explained by: (1) For SC and HCP initial packings, their structures are stable. During compaction the densification is mainly achieved by plastic deformation of Al component, little relative sliding and rolling between Al/SiC composite particles can be observed. Therefore, the compaction curves evolve smoothly; (2) Compared with SC and HCP, honeycomb initial packing structure is less stable. So at the early stage of compaction, the initial ordered packing structure is destroyed (please refer to the evolution of packing morphology in the inset images of **Figure 3(a)** for details, where the arrows indicate the tendency of movement for corresponding particles and the circled areas illustrate the local dense clusters formed after rearrangement), which leads to the rearrangement of the composite particles through sliding and rolling for densification. And this process continues until all the particles are in a stable state. From **Figure 3(a)** one can also find that even the initial

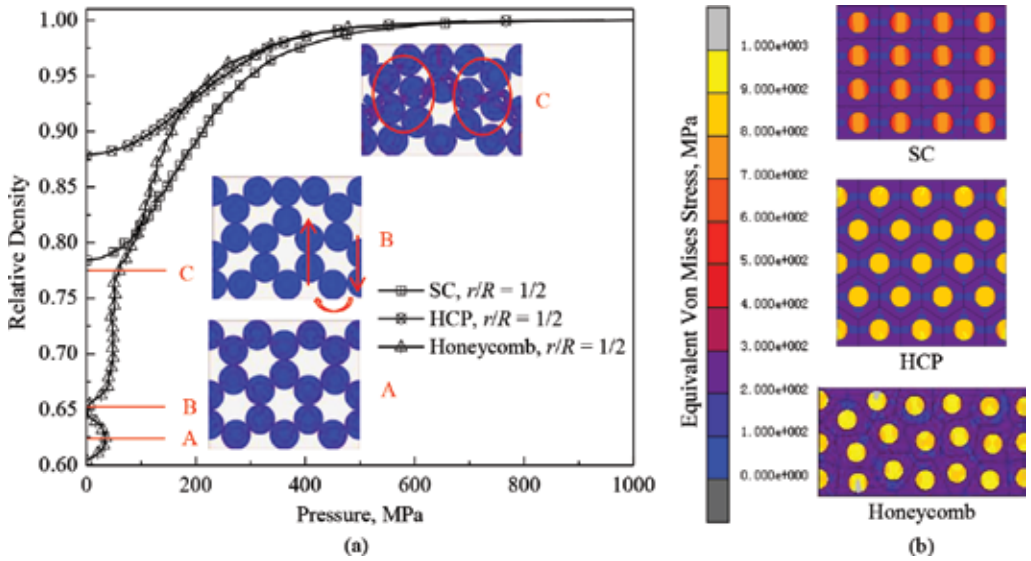

Figure 3. (a) Evolution of relative density with the pressure during compaction of different initial ordered packing structures, where the inset figures are the morphologies of compacts from honeycomb initial packing at different compaction stages; (b) morphologies of final compacts obtained in (a) and corresponding stress distributions.

packing structures are different, the compaction in each case can reach almost full densification with the relative density of about 1.0 for each compact, which exhibits the advantages of the Al/SiC composite powders with core/shell structures. However, the structures of final compacts and the distributions of stresses therein as indicated in **Figure 3(b)** all demonstrate different features. Especially for the compact obtained from honeycomb initial ordered packing, the shape of each composite particle and the distribution of equivalent Von Mises stresses are all non-uniform compared with the former two cases and more like disordered state, which will determine the final performance of the compact.

In comparison with ordered initial packings, the initial random packings of Al/SiC composite powders are frequently encountered in actual PM production. **Figure 4** gives the compaction curves of five initial random packings with different SiC contents and relative densities as well as corresponding model validation. As indicated in **Figure 4(a)**, the compaction curves are quite different from those in **Figure 3(a)**, which can be ascribed to the difference of initial packing structures. For each $\rho - P$ curve during compaction on random initial packing, three stages can be identified: (1) At the initial compaction stage with very low pressure, the densification is mainly implemented by particle rearrangement to fill the large voids or pores. Here, the translational motion and rotational motion of the particles are dominant in densification. (2) Once a stable packing is formed in the first stage, the compaction steps into the second stage for large deformation. At this stage, the relative density of the compact increases continuously with the pressure due to the plastic deformation of Al component for adjacent pore filling, which greatly increases the relative density. (3) When the pressure exceeds a critical value, the increasing rate of the relative density decreases, and each $\rho - P$ curve tends to level off because the large deformation of particles creates work hardening which impedes further

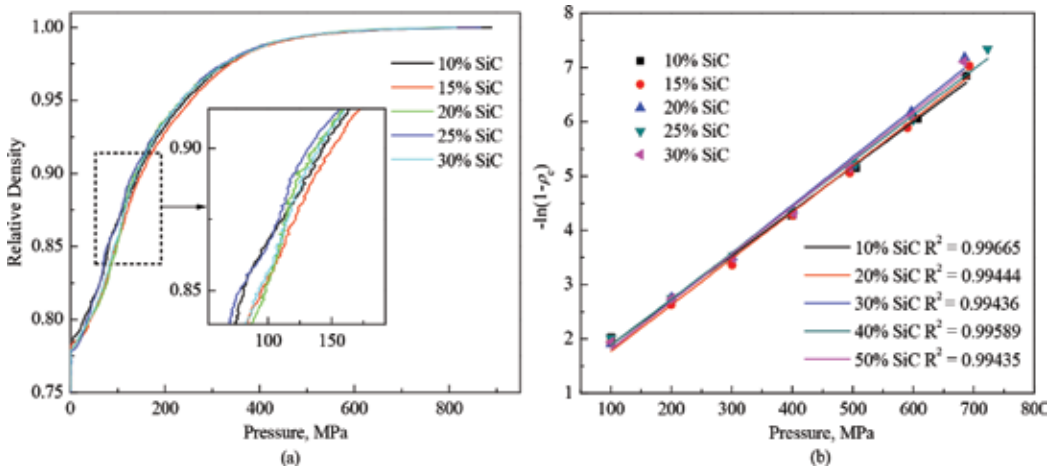

Figure 4. (a) Compaction curves for five initial random packings with different SiC contents, where the inset figure shows the local zoom of the compaction curves; (b) validation of the numerical model by fitting the simulation results with the Heckel equation (b).

deformation unless extra high pressure is applied. In this stage, the powder mass shows a bulk behavior. In order to validate the effectiveness of the model used in the simulation, the numerical results are fitted with Heckel equation given by [46, 47]:

$$\ln\left[1/\left(1-\rho_c\right)\right] = UP + Z \tag{4}$$

where ρ_c is the relative density of the compact; P is applied pressure; U and Z are constants. **Figure 4(b)** demonstrates that the simulation results agree well with the Heckel equation with high confidence (high R^2 value), which proves the robustness of the numerical model and the accuracy of the simulation results. It needs to note that both the differences of compaction curves as shown in the enlarged zoon of **Figure 4(a)** and of the slopes of the fitting lines as indicated in **Figure 4(b)** can be influenced by the initial packing structure and SiC content. But compared with the compaction on ordered initial packing structures, the influences of SiC content on the densification behavior are less significant, which will be discussed in the subsequent sections.

3.2. Initial packing structure effects

Previous results have illustrated that the initial packing structure of the composite powder or the SiC content can create effects on the compaction behavior and property of the compact. To further identify their important role in the densification process, the compaction on SC and HCP ordered initial packings with different SiC contents is shown in **Figure 5**, where **Figure 5(a)** gives the compaction curves and **Figure 5(b)** indicates the morphologies of the compacts under the pressure of 200 MPa and the stress distributions therein. Here, the equivalent Von Mises stress is given by:

$$\bar{\sigma} = \left[(\sigma_1-\sigma_2)^2+(\sigma_2-\sigma_3)^2+(\sigma_3-\sigma_1)^2\right]^{1/2}/\sqrt{2} \tag{5}$$

http://dx.doi.org/10.5772/intechopen.76563

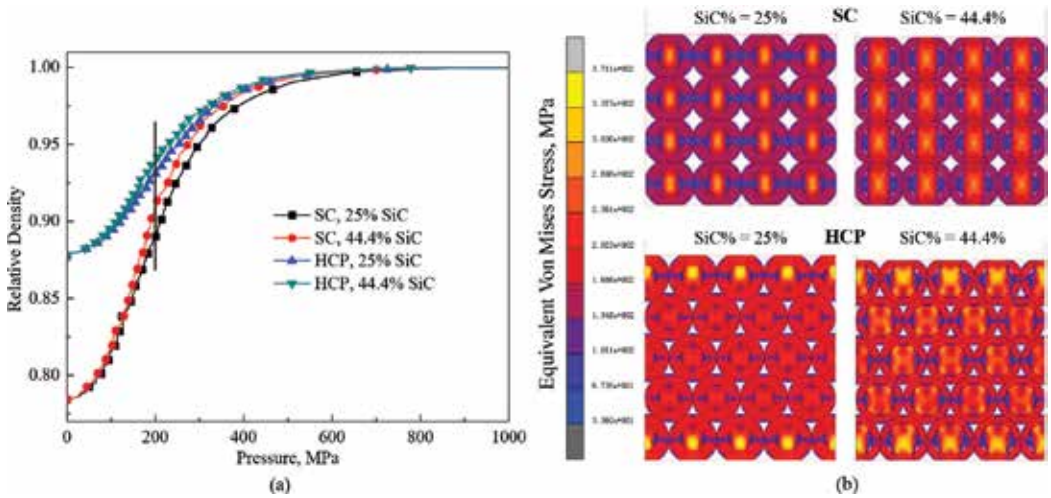

Figure 5. (a) Compaction on SC and HCP ordered initial packing structures with different SiC contents; (b) equivalent Von Mises stress distributions in the compacts formed from SC and HCP initial packings with respectively 25 and 44.4% SiC when the compaction pressure is 200 MPa.

where σ_1, σ_2, σ_3 are the principal Cauchy stresses along three main axes. It can be seen that the compaction on different initial packing structures can lead to different densification behavior and rate. For the same initial packing structure, increasing the SiC content can aid the densification. I.e. with a certain compaction pressure, the relative density of the compact with high SiC content is larger than that with low SiC content. This can be explained by the high efficient stress transmission as indicated in **Figure 5(b)** when P = 200 MPa. One can see that larger stresses are mainly concentrated on SiC particles (cores) in the compacts with higher SiC content, which can accelerate the densification through mass transfer by adjacent Al deformation extruded by neighboring SiC cores. Compared with the compacts obtained from SC initial packing, the stresses in corresponding compacts with HCP structure are larger, which implies the higher densification rate for the latter case. Meanwhile, from **Figure 5(b)** one can also find that debonding at the interface between Al and SiC occurs for both cases when the SiC content is high, the mechanism of this phenomenon can be discussed in the following section.

In addition to the compaction on ordered initial packing structures, the evolutions of morphologies and stresses in the compacts formed by random initial packings with five SiC contents at different compaction stages are also systematically studied. Here, the compaction on the random initial packing with 25% SiC is taken as an example for detailed analysis. **Figure 6** gives the morphology evolution of the compact and corresponding stress transmission/distribution at each compaction stage. As indicated, during compaction both translational motion (including the sliding as indicated by the arrow in the third snapshot of **Figure 6(a)**) and rotational motion are observed, which are mainly occurred in early stage of compaction when the pressure is low. In this case, the densification is mainly due to the rearrangement of the Al/SiC composite particles, and the force chain is formed as a skeleton or network. With the increase of the incremental modeling steps N, the particles that form the force network begin to deform when the pressure exceeds their yield limit. Due to the heterogeneity of the force

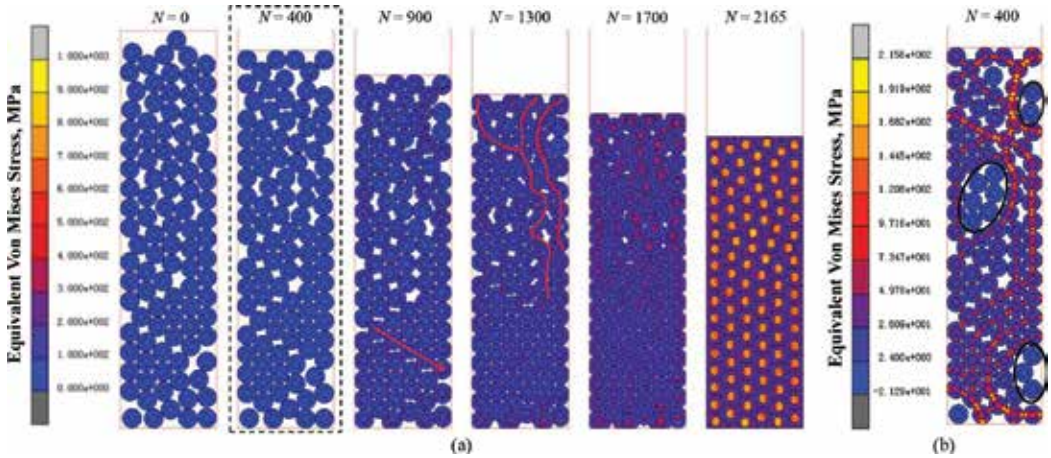

Figure 6. (a) Evolution of equivalent Von Mises stresses during compaction on random initial packing with 25% SiC; (b) force chain structure and stress transmission in the compact when the incremental modeling step is $N = 400$, where the circled local structures are the clusters surrounded by the force chains, within which no or only small stresses can be identified in these particles.

structure, the shape of each composite particle in the final compact is irregular. In the whole process, the force chain structure varies, which dominates the deformation of the particles and the stresses are mainly concentrated on SiC particles. To more clearly demonstrate the force chain structure and explain the irregular deformation of the composite Al/SiC particles, the compact obtained at the incremental modeling step $N = 400$ in **Figure 6(a)** is redisplayed while the scale of the legend is reduced as shown in **Figure 6(b)**. From the figure one can see that not all of the particles in the compact are involved in the force chain, some local clusters as circled are shielded by the force chain which makes them free from deformation, because the forces or stresses on these particles are very small or even nil, which will impede the densification process. On the other hand, the particles in the force chain are easily moved or deformed by the large forces acted on them, which will enhance the densification. On the whole, due to the non-uniformity of the force chain and stress distributions, even though the final compact can be fully dense, the deformation of the composite particles therein is not uniform. This phenomenon has been identified in the MPFEM modeling on the compaction of Fe-Al composite powders [42]. While unlike the compaction on mixed binary Al and SiC composite powders, the reinforced SiC particles are uniformly distributed in the fully dense final compact and the stress distributions are also homogeneous, which indicates the advantages of current process applied in PM production.

3.3. Quantitative analysis on particle rearrangement during compaction

It is known that the densification of composite powders during early stage of compaction is mainly due to the rearrangement of particles through translational motion and rotational motion, while systematic analysis on the particle rotation in the compaction process is less studied because this behavior is difficult to be quantitatively characterized. To achieve this, an algorithm is proposed to calculate the rotation of particles during compaction. **Figure 7(a)**

http://dx.doi.org/10.5772/intechopen.76563

schematically illustrates the particle (here two nodes adjacent to SiC core in Al is selected as the research target) relative position before (e.g. ΔOAB) and after (e.g. ΔOA′B′) rotation, here the coordinates of (x_A, y_A) for point A, (x_B, y_B) for point B, (x_A', y_A') for point A′, (x_B', y_B') for point B′ are known at each time step. Therefore, the rotational angle θ can be calculated by:

$$\theta = \alpha + \beta \tag{6}$$

where:

$$\alpha = \tan^{-1}\left(\frac{y_B - y_A}{x_B - x_A}\right) \tag{7}$$

and

$$\beta = \tan^{-1}\left(\frac{y_B' - y_A'}{x_B' - x_A'}\right) \tag{8}$$

To further study the effects of initial packing structures, three packings with the similar relative densities (≈ 0.74) and SiC (25%) but different structures as shown in **Figure 7(b)** were chosen for analysis. The results are shown in **Figure 8**, where **Figure 8(a)** gives the evolution of average rational angle with the relative density of each initial packing structure during compaction and **Figure 8(b)** indicates the quantitative statistics on the distribution of rotational angles. As can be seen from **Figure 8(a)** that with each case, the average rotational angle increases with the relative density but the increasing rate decreases. And different initial packing structures

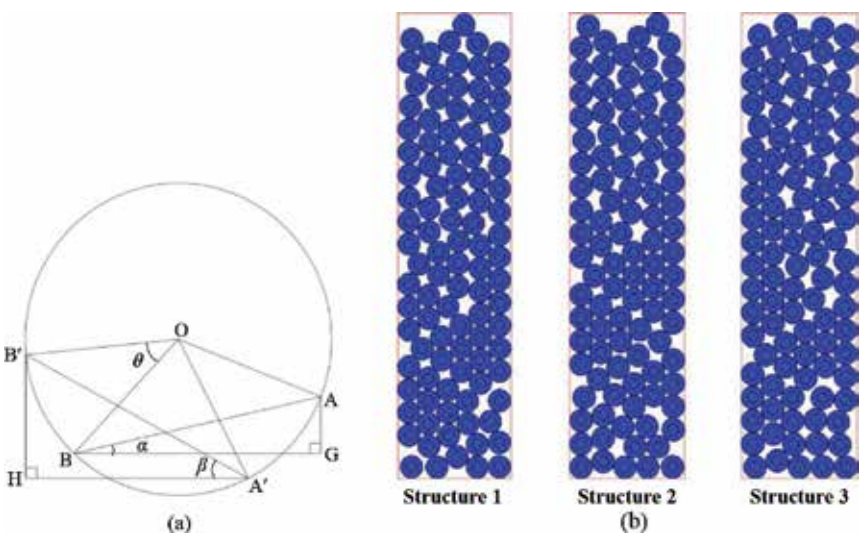

Figure 7. (a) Schematic diagram to calculate the rotation of one particle during compaction; (b) three initial packing structures with similar relative density and SiC content (25%) but different packing structures used for quantitative particle rotation calculation during compaction.

can result in different rotation behavior even the relative density and the composition of the composite powder are similar. Meanwhile, one can also find that the fast increasing region of rational angle is mainly located in the region where the relative density is lower than about 0.82. Previous researches [48] have demonstrated that 0.82 is the relative density of random close packing state with stable structure for 2D disks, beyond which both the translational motion and rotational motion during compaction become difficult. This variation has similar trend with previous results from other packing systems [31]. Besides, the distribution of average rotation angle in **Figure 8(b)** indicate that during compaction most particles rotate with the angle of 1–5°. Large scale particle rotation is mainly formed at the initial rearrangement stage of the compaction when the pressure is low. Because after deformation under high pressure the contact between neighboring particles changes from point to face, which restrains the further rotation of composite particles. From **Figure 8(b)** one can also find that different initial packing structures can lead to different rotation behavior, which will further determine the densification process as well as the resultant properties of the final compacts.

3.4. Debonding and rebonding phenomena

During compaction on composite powders with core/shell structures, a common phenomenon, i.e. debonding can be occurred, which has also been observed at the Al/SiC interface in current MPFEM simulation. Interestingly, after debonding, the separated Al and SiC in a composite particle can rebond again to form a good cohesion and combination at the interface. It needs to clarify that in current simulation only physical interaction at the interface is considered, chemical reactions are not included. Previous results in this chapter have shown that some composite particles are debonded during compaction. Especially for those particles that are close to the punches or close to the large voids, the debonding is more probable. Those composite particles that form local ordered dense packing structure are not likely to

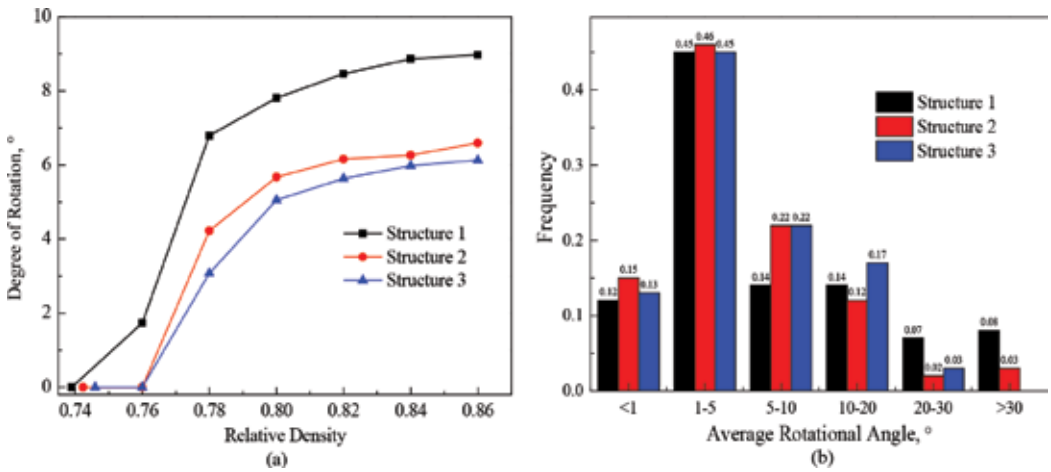

Figure 8. (a) Evolution of average rotational angle with the relative density for each initial packing structure during compaction when the SiC content is 25%; (b) distribution of average rotational angle in the final compacts formed by different initial packing structures.

http://dx.doi.org/10.5772/intechopen.76563

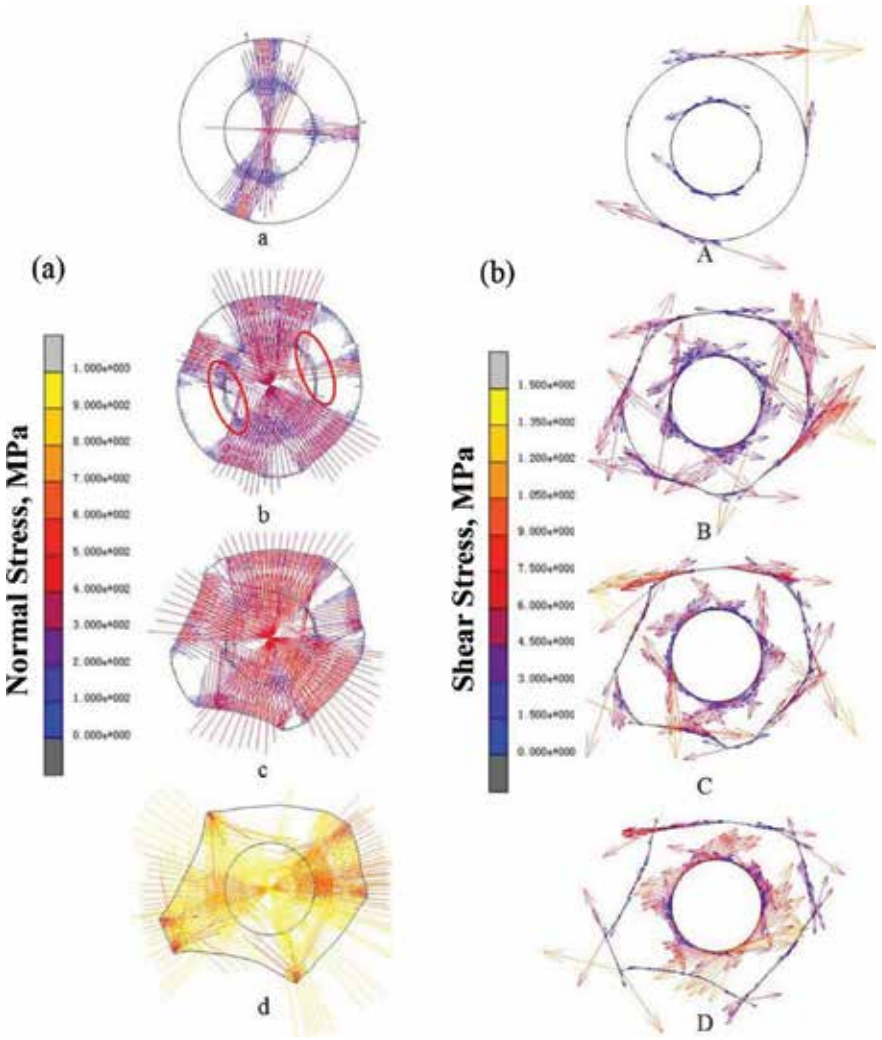

Figure 9. Evolution of (a): normal stress (a–d) and (b): shear stress (A–D) at the interface between Al and SiC of a given core/shell particle when SiC content is 25%. And (a–d)/(A–D) respectively correspond to 800, 1500, 1900, and 2160 incremental modeling steps.

debond unless the SiC content is very large. In order to explain the mechanisms of debonding and rebonding phenomena, a single Al/SiC composite particle in initial random packing is selected for analysis. The evolution of normal stresses and shear stresses in this particle at different stages of compaction is shown in **Figure 9**. As can be imagined from the figure that at the early stage of compaction, composite particles are fully rearranged with the help of relatively low pressure from the upper punch. In this case, no matter the tangential forces or the normal forces between particles or between Al and SiC at the interface are all very small. With the increase of the compaction pressure, the contact forces between composite particles increase. The large extrusion deformation or the shear due to relative sliding induces large tangential stresses at the interface between Al shell and SiC core, when the normal

contact forces or stresses are very small at this region, the debonding occurs. While with the further increase of the compaction pressure, the bulk density of the compact increases. The normal contact forces or stresses at the debonding region increase due to the extrusion from neighboring particles, leading to the rebonding at the interface. Through comparison, one can conclude that the occurrence of debonding phenomenon, which has also been identified in others' work [49], is mainly caused by sufficient tangential forces but insufficient normal forces at the interface. Therefore, the interface should have a certain shear strength and relatively large normal strength, which can not only effectively avoid the possible debonding, but also make the distribution of equivalent strain in the matrix more uniform.

4. Conclusions

DEM-FEM coupled MPFEM modeling on the single action die compaction of Al/SiC core/shell (core: SiC; shell: Al) composite powders with different initial packing structures was conducted from particulate scale in 2D. The effects of compaction pressure, initial packing structure, and SiC content (composition) on the packing densification were systematically presented. Various macro and micro properties such as relative density and distribution, stress and distribution, particle rearrangement through translational motion and rotational motion, deformation and mass transfer, and interfacial behavior between composite particles were characterized and analyzed. Following conclusions can be drawn:

1. MPFEM simulation can effectively reproduce the compaction densification of Al/SiC composite particles with core (SiC)/shell (Al) structures from particulate scale.
2. Beyond a certain Al content, the compaction on both ordered and random initial packings of the composite particles all can realize the full densification, however, the micro properties in these compacts are initial structure sensitive. And the densification rate is also different.
3. The compaction on Al/SiC core/shell composite powders can obtain more uniform relative density and stress distributions than other Al/SiC composite systems.
4. During compaction on random initial packings of Al/SiC composite powders, obvious particle rotations can be observed with the relative density of the compact between 0.74–0.82, and the value of average rotational angles is also affected by the initial packing structure.
5. The debonding between SiC core and Al shell during compaction on random initial packings mainly occurs at the area close to the large pore, where the normal stress is small and the shear stress is relatively large. To avoid it, sufficient normal stress at the core/shell contact area should be satisfied. For the compaction on ordered initial packing such as SC and HCP structures, debonding mainly appears close to the punches when the SiC content is relatively high, and it will be disappeared in the final stage of compaction.

The researches can not only enhance people's understanding on the compaction densification of Al/SiC composite powders with core/shell structures and various initial packing states, but

also provide the materials scientists and engineers with valuable references for the realization of high performance Al/SiC compact in future PM production.

Acknowledgements

The authors are grateful to National Natural Science Foundation of China (No. 51374070) and Fundamental Research Funds for the Central Universities of China (No. N162505001) for the financial support of current work.

Conflict of interest

We declare that we have no conflicts of interest to this work.

Nomenclature

Scalars

A	strength coefficient
B	material constant
E	Young's modulus
m	work hardening index
N	incremental modeling step
n	material constant
O	center of a circle
P	compaction pressure
r	radius of SiC particle
R	radius of Al/SiC composite particle
R^2	relative coefficient
U	constant
v	velocity
x	coordinate on X axis
y	coordinate on Y axis
Z	constant

Greek letters

α	angle
β	angle
Δ	triangle
ε	strain
ε_{ij}	strain tensor
$\dot{\bar{\varepsilon}}$	equivalent strain rate
$\bar{\varepsilon}$	equivalent strain
θ	angle
μ	frictional coefficient
ν	Poisson's ratio
ρ	relative density
ρ_c	relative density of the compact
σ	stress

Subscripts

0	initial time
1	spatial direction
2	spatial direction
3	spatial direction
A	spatial point
A′	spatial point
B	spatial point
B′	spatial point
c	compact
i	integer, ranging from 1 to 3
j	integer, ranging from 1 to 3
p	particulate
y	yield

Acronyms

2D	two-dimensional
CIPed	cold isostatic pressed
DEM	discrete element method
ECAPT	equal channel angular pressing and torsion
FEM	finite element method
HIPed	hot isostatic pressed
MPFEM	multi-particle finite element method
PM	powder metallurgy
PRMMCs	particulate reinforced metal matrix composites
vol.	volume
wt.	weight

Author details

Xizhong An*, Yu Liu, Fen Huang and Qian Jia

*Address all correspondence to: anxz@mail.neu.edu.cn

School of Metallurgy, Northeastern University, Shenyang, PR China

References

[1] Ling CP, Bush MB, Perera DS. The effect of fabrication techniques on the properties of Al-SiC composites. Journal of Materials Processing Technology. 1995;**48**:325-331. DOI: 10.1016/0924-0136(94)01665-N

[2] Tavakoli AH, Simchi A, Seyed Reihani SM. Study of the compaction behavior of composite powders under monotonic and cyclic loading. Composites Science and Technology. 2005;**65**:2094-2104. DOI: 10.1016/j.compscitech.2005.05.016

[3] Prasad Reddy A, Vamsi Krishna P, Narasimha Rao R, Murthy NV. Silicon carbide reinforced aluminium metal matrix nano composites – A review. Materials Today: Proceedings. 2017;**4**:3959-3971

[4] Lloyd DJ, Lagace H, McLeod A, Morris PL. Microstructural aspects of aluminium-silicon carbide particulate composites produced by a casting method. Materials Science and Engineering: A. 1989;**107**:73-80. DOI: 10.1016/0921-5093(89)90376-6

[5] Sridhar I, Fleck NA. Yield behavior of cold compacted composite powders. Acta Materialia. 2000;**48**:3341-3352. DOI: 10.1016/S1359-6454(00)00151-8

[6] Tang F, Hagiwara M, Schoenung JM. Formation of coarse-grained inter-particle regions during hot isostatic pressing of nanocrystalline powder. Scripta Materialia. 2005;**53**:619-624. DOI: 10.1016/j.scriptamat.2005.05.034

[7] Tang F, Hagiwara M, Schoenung JM. Microstructure and tensile properties of bulk nanostructured Al-5083/SiC_p composites prepared by cryomilling. Materials Science and Engineering: A. 2005;**407**:306-314. DOI: 10.1016/j.msea.2005.07.056

[8] Jamaati R, Amirkhanlou S, Toroghinejad MR, Niroumand B. Effect of particle size on microstructure and mechanical properties of composites produced by ARB process. Materials Science and Engineering: A Structural. 2011;**528**:2143-2148. DOI: 10.1016/j.msea.2010.11.056

[9] Ghiţă C, Popescu IN. Experimental research and compaction behavior modelling of aluminium based composites reinforced with silicon carbide particles. Computational Materials Science. 2012;**64**:136-140. DOI: 10.1016/j.commatsci.2012.05.031

[10] Li P, Zhang X, Xue KM, Li X. Effect of equal channel angular pressing and torsion on SiC-particle distribution of SiC_p-Al composites. Transactions of the Nonferrous Metals Society of China. 2012;**22**:s402-s407. DOI: 10.1016/S1003-6326(12)61738-5

[11] Moazami-Goudarzi M, Akhlaghi F. Effect of nanosized SiC particles addition to CP Al and Al-Mg powders on their compaction behavior. Powder Technology. 2013;**245**:126-133. DOI: 10.1016/j.powtec.2013.04.025

[12] Zakaria HM. Mocrostructural and corrosion behavior of Al/SiC metal matrix composites. Ain Shams Engineering Journal. 2014;**5**:831-838. DOI: 10.1016/j.asej.2014.03.003

[13] El-Kady O, Fathy A. Effect of SiC particle size on the physical and mechanical properties of extruded Al matrix nanocomposites. Materials & Design. 2014;**54**:348-353. DOI: 10.1016/j.matdes.2013.08.049

[14] Majzoobi GH, Atrian A, Enayati MH. Tribological properties of Al7075-SiC nanocomposite prepared by hot dynamic compaction. Composite Interfaces. 2015;**22**:579-593. DOI: 10.1080/09276440.2015.1055955

[15] Zhang L, Xu HQ, Wang Z, Li QG, Wu JY. Mechanical properties and corrosion behavior of Al/SiC composites. Journal of Alloys and Compounds. 2016;**678**:23-30. DOI: 10.1016/j.jallcom.2016.03.180

[16] Bajpai G, Purohit R, Rana RS, Rajpurohit SS, Rana A. Investigation and testing of mechanical properties of Al-nano SiC composites through cold isostatic compaction process. Materials Today: Proceedings. 2017;**4**:2723-2732

[17] Penchal Reddy M, Shakoor RA, Parande G, Manakari V, Ubaid F, Mohamed AMA, Gupta M. Enhanced performance of nano-sized SiC reinforced Al metal matrix nanocomposites synthesized through microwave sintering and hot extrusion techniques. Progress in Natural Science. 2017;**27**:606-614. DOI: 10.1016/j.pnsc.2017.08.015

[18] Biswas K. Comparison of various plasticity models for metal powder compaction processes. Journal of Materials Processing Technology. 2005;**166**:107-115. DOI: 10.1016/j.jmatprotec.2004.08.006

[19] Khoei AR, Azami AR, Azizi S. Computational modeling of 3D powder compaction processes. Journal of Materials Processing Technology. 2007;**185**:166-172. DOI: 10.1016/j.jmatprotec.2006.03.122

[20] Eksi AK, Yuzbasioglu AH. Effect of sintering and pressing parameters on the densification of cold isostatically pressed Al and Fe powders. Materials & Design. 2007;**28**:1364-1368. DOI: 10.1016/j.matdes.2006.01.018

[21] Tahir SM, Ariffin AK, Anuar MS. Finite element modelling of crack propagation in metal powder compaction using Mohr-coulomb and elliptical cap yield criteria. Advanced Powder Technology. 2010;**202**:162-170. DOI: 10.1016/j.powtec.2010.04.033

[22] Diarra H, Mazel V, Busignies V. FEM simulation of the die compaction of pharmaceutical products: Influence of visco-elastic phenomena and comparison with experiments. International Journal of Pharmaceutics. 2013;**453**:389-394. DOI: 10.1016/j.ijpharm.2013.05.038

[23] An XZ, Xing ZT, Jia CC. Cold compaction of copper powders under mechanical vibration and uniaxial compression. Metallurgical and Materials Transactions A: Physical Metallurgy and Materials Science. 2014;**45**:2171-2179. DOI: 10.1007/s11661-013-2160-6

[24] An XZ, Zhang YL, Zhang YX, Yang S. Finite element modeling on the compaction of copper powder under different conditions. Metallurgical and Materials Transactions A: Physical Metallurgy and Materials Science. 2015;**46A**:3744-3752. DOI: 10.1007/s11661-015-2929-x

[25] Han P, An XZ, Zhang YX, Zou ZS. FEM modeling on the compaction of Fe and Al composite powders. Journal of Mining and Metallurgy, Section B: Metallurgy. 2015;**51**:163-171. DOI: 10.2298/JMMB150210020H

[26] An XZ, Yang RY, Dong KJ, Zou RP, Yu AB. Micromechanical simulation and analysis of one-dimensional vibratory sphere packing. Physical Review Letters. 2005;**95**:205502-1-205502-4. DOI: 10.1103/PhysRevLett.95.205502

[27] Yu AB, An XZ, Zou RP, Yang RY, Kendall K. Self-assembly of particles for densest packing by mechanical vibration. Physical Review Letters. 2006;**97**:265501-1-265501-4. DOI: 10.1103/PhysRevLett.97.265501

[28] Wu YL, An XZ, Yu AB. DEM simulation of cubical particle packing under mechanical vibration. Powder Technology. 2017;**314**:89-101. DOI: 10.1016/j.powtec.2016.09.029

[29] Zhao B, An XZ, Wang Y, Qian Q, Yang XH, Sun XD. DEM dynamic simulation of tetrahedral particle packing under 3D mechanical vibration. Powder Technology. 2017;**317**:171-180. DOI: 10.1016/j.powtec.2017.04.048

[30] Martin CL, Bouvard D. Isostatic compaction of bimodal powder mixtures and composites. International Journal of Mechanical Sciences. 2004;**46**:907-927. DOI: 10.1016/j.ijmecsci.2004.05.012

[31] Procopio AT, Zavaliangos A. Simulation of multi-axial compaction of granular media from loose to high relative densities. Journal of the Mechanics and Physics of Solids. 2005;**53**:1523-1551. DOI: 10.1016/j.jmps.2005.02.007

[32] Frenning G. An efficient finite/discrete element procedure for simulating compression of 3D particle assemblies. Computer Methods in Applied Mechanics and Engineering. 2008;**197**:4266-4272. DOI: 10.1016/j.cma.2008.05.002

[33] Lee KH, Lee JM, Kim BM. Densification simulation of compacted Al powders using multi-particle finite element method. Transactions of the Nonferrous Metals Society of China. 2009;**19**:s68-s75

[34] Zhang J. A study of compaction of composite particles by multi-particle finite element method. Composites Science and Technology. 2009;**69**:2048-2053. DOI: 10.1016/j.compscitech.208.11.020

[35] Frenning G. Compression mechanics of granule beds: A combined finite/discrete element study. Chemical Engineering Science. 2010;**65**:2464-2471. DOI: 10.1016/j.ces.2009.12.029

[36] Jerier JF, Hathong B, Richefeu V, Chareyre B, Imbault D, Donze FV, Doremus P. Study of cold powder compaction by using discrete element method. Powder Technology. 2011;**208**:537-541. DOI: 10.1016/j.powtec.2010.08.056

[37] Harthong B, Imbault D, Dorémus P. The study of relations between loading history and yield surfaces in powder materials using discrete finite element simulations. Journal of the Mechanics and Physics of Solids. 2012;**60**:784-801. DOI: 10.1016/j.jmps.2011.11.009

[38] Harthong B, Jérier JF, Richefeu V, Chareyre B, Dorémus P, Imbault D, Donzé FV. Contact impingement in packings of elastic-plastic spheres, application to powder compaction. International Journal of Mechanical Sciences. 2012;**61**:32-43. DOI: 10.1016/j.ijmecsci.2012.04.013

[39] Gustafsson G, Häggblad HÅ, Jonsén P. Multi-particle finite element modelling of the compression of iron ore pellets with statistically distributed geometric and material data. Powder Technology. 2013;**239**:231-238. DOI: 10.1016/j.powtec.2013.02.005

[40] Güner F, Cora ÖN, Sofuoğlu H. Numerical modeling of cold powder compaction using multi particle and continuum media approaches. Powder Technology. 2015;**271**:238-247. DOI: 10.1016/j.powtec.2014.11.008

[41] Zhang YX, An XZ, Zhang YL. Multi-particle FEM modeling on microscopic behavior of 2D particle compaction. Applied Physics A: Materials Science & Processing. 2015; **118**:1015-1021. DOI: 10.1007/s00339-014-8861-x

[42] Han P, An XZ, Zhang YX, Huang F, Yang TX, Fu HT, Yang XH, Zou ZS. Particulate scale MPFEM modeling on compaction of Fe and Al composite powders. Powder Technology. 2017;**314**:69-77. DOI: 10.1016/j.powtec.2016.11.021

[43] Han P, An XZ, Wang DF, Fu HT, Yang XH, Zhang H, Zou ZS. MPFEM simulation of compaction densification behavior of Fe-Al composite powders with different size ratios. Journal of Alloys and Compounds. 2018;**741**:473-481. DOI: 10.1016/j.jallcom.2018.01.198

[44] Huang F, An XZ, Zhang YX, Yu AB. Multi-particle FEM simulation of 2D compaction on binary Al/SiC composite powders. Powder Technology. 2017;**314**:29-48. DOI: 10.1016/j.powtec.2017.03.017

[45] An XZ, Yang RY, Zou RP, Yu AB. Effect of vibration condition and inter-particle frictions on the packing of uniform spheres. Powder Technology. 2008;**188**:102-109. DOI: 10.1016/j.powtec.2008.04.001

[46] Heckel RW. Density-pressure relationships in powder compaction. Transactions of the Metallurgical Society of the American Institute of Mechanical Engineers. 1961;**221**:671-675. DOI: 10.1016/0026-0657(92)90966-1

[47] Ramberger R, Burger A. On the application of the Heckel and Kawakita equations to powder compaction. Powder Technology. 1985;**43**:1-9. DOI: 10.1016/0032-5910(85)80073-5

[48] German RM. Particle Packing Characteristics. 2nd ed. Princeton: Metal Powder Industries Federation; 1989. pp. 34-38. DOI: 10.1016/0032-5910(90)80071-6

[49] Haddadi H, Teodosiu C. 3D-analysis of the effect of interfacial debonding on the plastic behavior of two-phase composites. Computational Materials Science. 1999;**16**:315-322. DOI: 10.1016/S0927-0256(99)00074-9

Chapter 3

Processing of Graphene/CNT-Metal Powder

Prashantha Kumar HG and Anthony Xavior M

Additional information is available at the end of the chapter

http://dx.doi.org/10.5772/intechopen.76897

Abstract

In recent days, the demand for powder metallurgy components has increased due to unusual combination of properties. Carbon allotropes such as graphene and CNT are the novel material to enhance the properties of powder metallurgy component. However, processing of such materials is in infancy stage due lack of advance processing technique. This can be addressed through integration of several fabrication techniques to meet the industrial demands. The processing method and its important parameter will define the final property of the component. Such materials have found its applications in various fields like, sports, bio implants, aerospace and automobile sector.

Keywords: graphene, CNT, powder technology, sintering, metal matrix composite (MMC)

1. Introduction

Combinations of two or more physically and chemically distinct materials that results in improved properties compared to individual materials are termed as "composites." Due to the adequate combination of such distinct materials, the properties of composites can be enhanced due to the presence of various materials. Composite materials bring the additional strength, stiffness apart from reducing the overall density compared to monolithic and non-aggregates allowing considerable reduction in the weight. Additionally, composites possess unidirectional properties (specific tensile strength) and increased fatigue endurance. The reinforcement plays an important role by providing the additional strength, stiffness and tribological properties in the composite. In many cases, the important properties of the reinforcement are strength, hardness and stiffness which are normally higher than the matrix

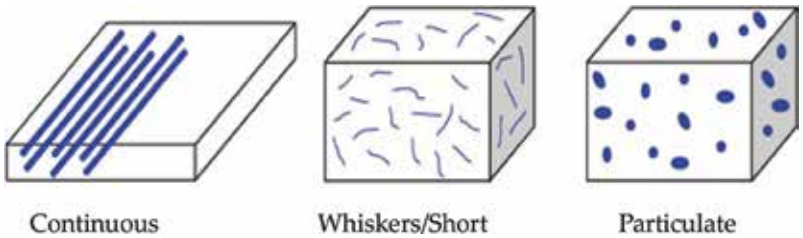

Figure 1. Type of reinforcements used for the composites.

materials. Today, the most man made engineered composites includes mortar; concrete; reinforced plastics; ceramic composites and metal composites. Particulates, whiskers/short fibers are the common type of reinforcements (**Figure 1**) used successfully for the fabrication of composite. Particulates are available in platelets, spherical and various regular or irregular shapes which may be having equal geometry in all directions. The particulate reinforcement was limited to 30–40 vol% in the composite due to its brittleness and fabrication difficulties. Fiber glasses were the first modern composites and are used for sports materials, car bodies, ship and other structural applications. But, due to the advancement in the composite technology, carbon fibers replaced the glass reinforcement in the composite and were used for many expensive sporting equipment and aircrafts structures. Carbon nanotube is being used successfully in these days for making of stronger and lighter composites. Another advantage of any composite material is that their properties are tailorable to certain extent along any direction. Further, these developed composite materials have design—flexibility, close tolerance, high durable, chemical inert and corrosive resistance. Also, the innovation in the fabrication techniques and combination of advanced materials resulted in superior thermal stability, high temperature retention and outstanding electrical properties. Composite materials are used for various applications such as building blocks, structures, bridges, automobile components, race car bodies, aerospace structural materials, space crafts and more.

2. Metal matrix composites (MMCs)

Metal matrix composites (MMCs) comprises lightweight and low-density materials (aluminum, magnesium, copper, etc.) reinforced with fiber or particulate of ceramic (silicon carbide, alumina, graphite, etc.). MMCs gave the opportunity to tailor the desire properties for specific applications. The important properties of metal matrix composites are stiffness, specific strength at elevated operating temperature and high tribological performance. On the other hand, fabrication cost of MMCs found to be higher for high performance application such as space and military and conceding the ductility and toughness. Also, MMCs have wide applications and are used in jet engines, aircrafts, satellite materials, and piston materials, cutting tools and space shuttle (NASA). MMCs with high strength and specific stiffness could be used in high speed machinery tools, robots, ships and rotating shaft where weight is an important criterion. MMCs also exhibit good wear resistance with high specific strength which is favorable for brake and engine components. Further, flexibility in tailorable thermal conductivity

and thermal expansion, MMCs are very good candidate for precision machinery, lasers and electronic packaging. In order to make use of MMCs in all the production areas and commercially attractive, prioritized research and development should be made on highly reliable manufacturing process with lowering the processing costs. Also, advanced processing techniques in powder metallurgy, plasma spraying, liquid metal infiltration, innovative casting methods and innovative combination of advanced reinforcing materials is needed very much. Further, functionalization and coating on the matrix/reinforcement are very much necessary which can prevent the deleterious chemical reaction at higher operating temperature conditions.

3. Powder metallurgy process

Powder metallurgy consists of a sequence of activities where, a feedstock in powder form μm to nm is used for fabricating the components of several shape and structures. **Figure 2** shows the general sequence of operations involved in a typical powder metallurgy production technology to obtain a finished component. Mechanical alloying, milling, electrolytic decomposition and gas atomization are the few metal powder techniques. Metal or alloy powder comes in various shapes and sizes which are dependent on the production method and parameters. Mixing of powders involves the introduction of various metal/alloy powders along with calculated quantity of reinforcement materials. Thus obtained powder mixtures are subjected to consolidation using rigid tool set comprising of die and punches. Thus obtained green compacts are sintered to make the particle bonding, (**Figure 3**) enhance the strength and the integrity which is usually done in protective atmosphere. The powder metallurgy process exists for the past 100 years, over the past years it has become a superior method to produce high-quality realistic industrial components with integration of novel reinforcements during preprocessing stage.

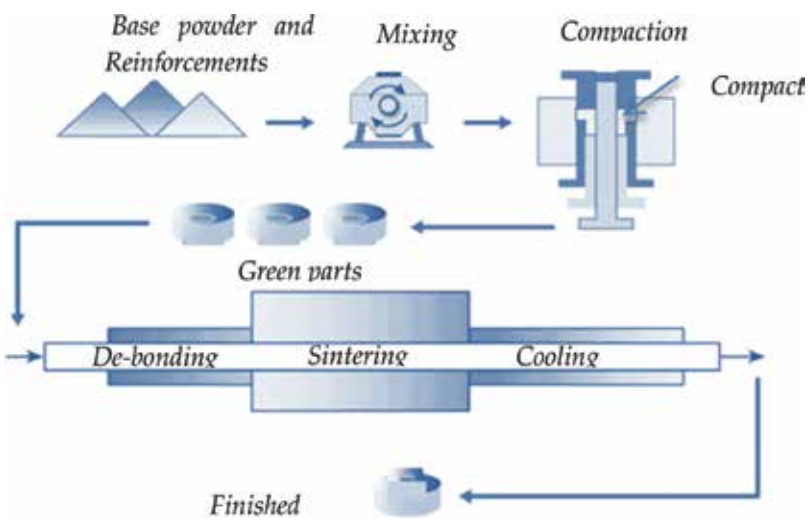

Figure 2. Conventional powder metallurgy process.

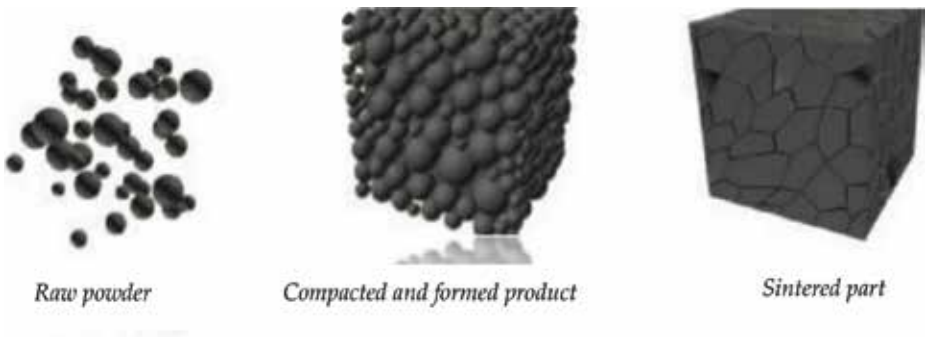

Figure 3. Powder to bonded structure during sintering.

With the several advantages of powder technology it become highly sustainable processing method over many conventional metal forming methods in producing complex shape, effective raw material utilization and the high tolerance. In the recent years, powder metallurgy process has been upgraded to consolidate pores or fully dense structures. Out of several new methods like hot isostatic pressing (HIP), metal injection molding (MIM), composites produced using powder forging (PF) and metal additive manufacturing (AM) have gained much popularity. **Figure 4** shows some of the structures produced through powder metallurgy route. Most of the powder metallurgy parts include filtration systems, magnetic assemblies, automobile components and structural parts. Gears, bushes and bearings produced through powder metallurgy process exhibit the more porous but they naturally reduce the noise. Powder metallurgy is also a very feasible technique for producing parts with magnetic properties. Further, magnetism can be enhanced by varying the sintering parameters.

3.1. Advantages of powder metallurgy process

The main advantage of powder metallurgy process is its ability to compress the powder into final size of closed dimensions and there is no need of any other subsequent forming process. Further, the process utilizes the 100% raw materials to get final component there by reducing the production cost compared to other conventional process (5–10% wastage). In the powder metallurgy process metal or alloy will not melt completely. So, there will not be any impurities by oxidation or deoxidizing or impurities from the crucible. Also, the process enables the production of high purity materials where, sintering is carried out in vacuum or gas atmosphere which will remain as the unique atmosphere throughout the process. Powder metallurgy enables the correctness of the material composition/weight/volume ratio and its homogeneity and it is suitable for mass production of same shape components.

3.2. Post processing of powder metallurgy

According to the specific densification requirements, sintered metal or alloy compacts are subjected to post processing treatments which includes impregnation, repressing, heat treatment, surface treatment and extrusion. Impregnation is performed by dipping oil or plastic into molten metal. The specific purpose of this process is to improve the self- lubrication,

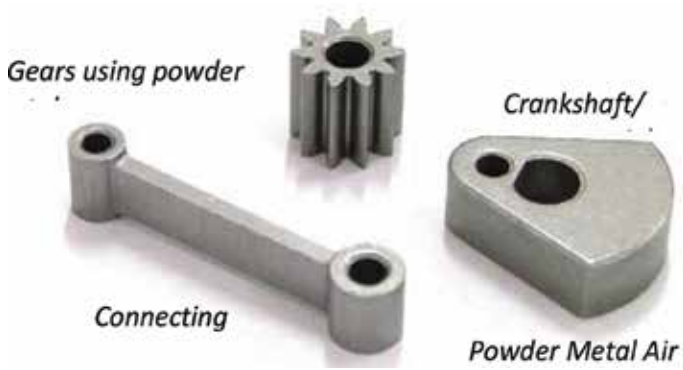

Figure 4. Complex structures produced through powder metallurgy.

wear resistance, strength and rusting proof. Repressing is carried out to improve the various mechanical properties, surface roughness and physical properties. In order to improve the product performance, sintered components are heated to a certain temperature and cooled with controlled temperature. Thermomechanical treatment, chemical treatment and heat hardening are the commonly used methods. Heat treated parts exhibits the well refined grain structure, high strength and high fracture toughness. Surface heat treatment methods such as steam treatment, galvanizing, plating, etc., are performed to make pores free and dense surface. In addition, extrusion, forging, welding and special processing method are used to obtain a desired shape, improved mechanical properties and high tolerance sintered structures of the final requirement to improve the product quality and its performance.

4. Allotropes of carbon

Carbon (C) is a chemical element with atomic number 6 and having [He] 2s22p2 electron configuration [1]. It is the fourth most abundant chemical element on the earth by mass. Diamond, amorphous carbon, graphite, and fullerenes are the well-known allotropes of the carbon. **Figure 5** shows the various crystallographic physical structures of these allotropes. Diamond is well known for its high hardness, which consist of pure sp3 hybridized carbon atoms with the strong covalent bonding among carbon atoms (**Figure 5**). Diamond is frequently used as cutting and polishing tools [2]. Graphite is made up of layers of carbon atoms in a planar structure (**Figure 5b**). The carbon atoms are organized in a hexagonal lattice. Graphite is the softest structure in which the carbon atoms are sp2 hybridized and the layers are hold by van der Waals force of attraction. Graphite is mainly used in industrial lubrication purposes. Other allotropic form is the amorphous carbon. It is soot and black carbon which does not have any crystalline structure (**Figure 5**). Amorphous carbon can be used as inks, paints, and industrial rubber filler [3]. Fullerene is the fourth allotrope of carbon at nanoscale. **Figure 5d–f** demonstrates the structures of fullerene family members. It includes the ellipsoidal fullerenes, spherical fullerene (buckyball), cylindrical carbon nanotubes, and planar graphene. In the buckyball (C60) all the carbon atoms are arranged in the three adjacent carbon atoms

with covalent bonding (**Figure 5d**) and these are having promised applications in polymer as filler to increase the mechanical strength. Ellipsoidal fullerenes; C70 (**Figure 5e**), C84, C72 and C76, icosahedral fullerene; C540 is also synthesized in the laboratories [4]. Carbon nanotubes (CNTs) (**Figure 5f**) and the graphene are discussed in the next sections.

4.1. Carbon nanotube (CNT)

In 1991 CNTs were first discovered by a scientist Sumio Iijima (NEC Company, Tsukuba, Japan) [5]. The discover looks like concentric carbon tube called as multi walled carbon nanotube as shown in **Figure 6**. At the later stages another form of CNT called single walled carbon nanotube (SWCNT) was discovered. One dimensional fullerene with tubular structure of carbon atom is called as SWNT which poses a lower aspect ratio compared to SWCNT and also have different mechanical and electrical properties. CNT poses excellent thermal conductivity which is equal to diamond [1]. In the recent years, carbon nanotubes (CNTs) are known to be one of the most efficient nanomaterials making next generation engineering and industrial revolution. Extraordinary properties of CNTs are of high demand mainly in semi-conductors, electronics and aerospace fields, etc. **Figure 6** shows the various types of CNTs which are depending on the number of carbon single atom layers (x). CNTs are referred to as SWCNTs (**Figure 6a**) if x = 1 (single layer of carbon atom), DWCNTs (**Figure 6b**) if x = 2 (double layer of carbon atom) and MWCNTs (**Figure 6c**) if x < 2 (multilayer of carbon atom). The diameter of CNTs is in nanometric scale and the length will be several micrometers to millimeter. CNTs exhibit unique properties such as high tensile strength (up to 100 GPa) and young's modulus (up to 1500 GPa) [6].

The quality of produced CNTs highly relies on the method of synthesis. Arc discharge method, laser ablation and chemical vapor deposition technique (CVD) are the three main methods to manufacture CNTs. However CVD method got the immense attraction due better quality, high purity and better control during the synthesis [7]. CNTs which are produced through this methods is very much ideal to use for composite due to high purity during production. All other methods will induce the some percentage of impurities such as graphite, fullerenes and other various catalysts during production. Thus synthesized individual CNTs will have agglomerated, interwoven and entwined. So, dispersion of such CNTs becomes a crucial challenge while processing CNTs—metal matrix composite. Moreover, due to van der Waals force of attraction of carbon surfaces also will increases the much difficulty in CNTs dispersion [8]. An independent separated CNT is the main objective of the dispersion where it can orient in one dimension or as two dimensional (as a flat sheet) or like a three dimensions (as a bulk solid). Dispersion of CNTs was carried out through chemical or mechanical processing. Dispersion through mechanical means was done by ultrasonic liquid processor (ULP); whereas, chemical dispersion is carried out through functionalizing the surface energy of CNT. Advantage of functionalization will help in adhesion characteristics to the matrix, which imparts the reduction in agglomerations. Ultrasonication method usually results in improvement of the uniform and homogeneous dispersion of the CNTs by shortening the size of CNT. Also, the disadvantage of this technique involves the risk of tube wall damage or breakage, removal of outer one layer in MWCNTs and shortens [9]. A study showed that, ≈70–≈90% purification take place during ultrasonication of CNTs [15]. Ball milling is the other option for the CNTs dispersion, to modify the aspect ratio, to obtain CNTs nanoparticles and for

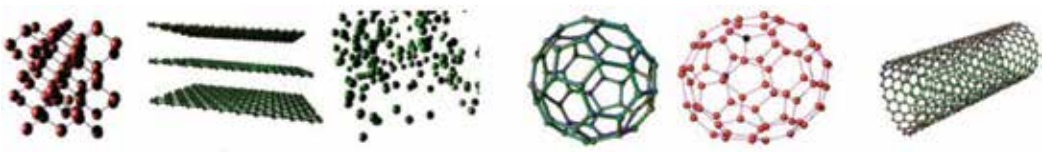

Figure 5. Allotropes of carbon (a) diamond (b) graphite (c) amorphous carbon (d) spherical fullerene, C60 (e) ellipsoidal fullerene, C70. (f) SWCNT.

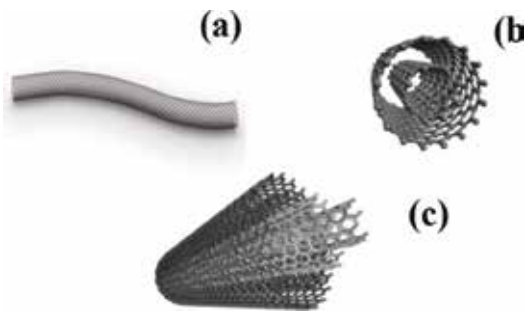

Figure 6. Different types of CNTs based on their number of carbon single atom cylinders: (a) single wall CNT (SWNT); (b) double wall CNT (DWCNT); and (c) multi wall CNT (MWCNT).

functionalizing. Various chemical-mechanical reactions are initiated during ball milling of CNTs. During ball milling CNTs are subjected to severe mechanical strain and may break the structure depending on the milling ratio.

4.2. Graphene

Graphene is a two dimensional sp^2 hybridized, one-atom-thick planar sheet of carbon atoms form a honeycomb crystal lattice (**Figure 7**). The graphene sheet exists in hexagonal structure in which each atom possesses three bands (σ bonds) which are together with its adjacent neighbor [10]. The term graphene was derived as combination graphite with the suffix "–ene" which describes the single layer of carbon [11].

Graphene is the basic structural element for all the allotropes of carbon and it is reflected as the mother of all graphitic forms group. Graphene can be wrapped and structured into buckyball (0D), rolled into carbon nanotube (1D), and can be stacked into graphite (3D) as shown in the **Figure 8**. Distance between the two adjacent graphene sheets is approximately 0.3 nm and these are held together with the weak van der Waals forces [12]. Graphite has been studied extensively for decades but experiments on graphene are on infancy stage. This might be due to difficulty in dispersion or isolation of single layer of graphene.

4.3. Carbon nanotube: metal matrix composite

Due to the astonishing properties, CNTs received the attention of the researchers in utilizing it for developing composites. The research took place in polymer, ceramic and metal-based composite. But, major research was carried out on polymer composites due low stress

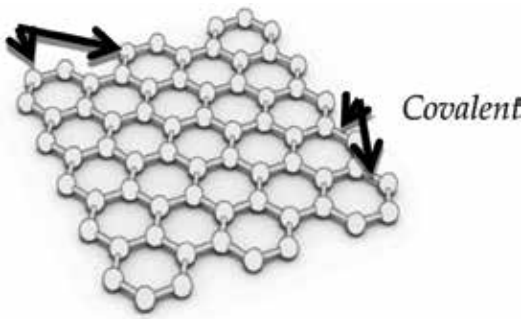

Figure 7. Molecular model (single sheet) of a graphene.

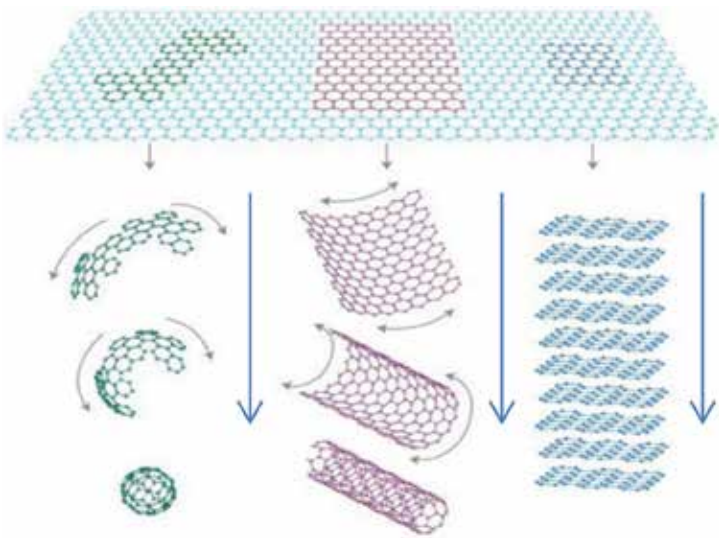

Figure 8. Graphene is a building material (2D) for other carbon-based dimensionalities [36] such as buckyball 0D (left), rolled into nanotubes 1D (middle) or stacked into graphite 3D (right).

and low temperature operating conditions compared to ceramic or metal matrix composites. Metal matrix composite processing requires high pressure, high temperature and the process should be carried out in a controlled atmosphere. CNT reinforced metal matrix composites exhibited enormous improvement in the strength and stiffness. But, there are still several challenges in development of CNT-metal matrix composites to make use of its compete properties. The primary challenge is obtaining a uniform and homogeneous dispersion. CNT always tends to agglomerate cluster formation due to large surface area and tubular structure. Also, it exhibits a non-wetting property with the molten metal which leads to agglomeration. Other challenge of CNT is retaining its structure along with the chemical stability when processed at high temperature and stressed condition. But CNTs are capable of producing a stronger material to the human mankind for many applications have been reported in terms of mechanical and functional material.

Uniform distribution of carbon nanotube in the metal matrix is the main criteria for the successful processing and it includes minimal damage to CNTs physical structure. The retention of its structure is subjected to operating temperature and the applied stress. At elevated temperature, CNT is subjected to react with the molten metal/alloy and leads to carbide formation. Formation of carbides within the matrix material may have some advantages but it is not favorable when concentrating for particular application. Alignment of the CNT during processing will constitute the overall property of the developed composite. It is also possible to achieve unidirectional properties depending upon the sequence and method of processing. Currently, CNTs with various combinations of matrix such as aluminum (Al), nickel (Ni), copper (Cu), magnesium (Mg), titanium (Ti), silicon (Si), cobalt (Co), and zinc (Zn), etc., are successfully developed. Among metals, aluminum with CNTs combination constitutes a major literature followed by copper and magnesium [13].

4.4. Processing methods of CNT-metal matrix composite

Casting process has been used to fabricate Mg-CNT composites. CNT was coated by Ni electroless deposition method for better wetting with the Mg before adding to the Mg, which was melted at 700°C followed by pouring of CNTs to the melt by stirring and cast into ingots. Thus produced Mg-CNTs composites exhibited 150% improvement in the tensile strength and 30% improvement in the ductility for only addition of 0.67 wt% CNT. Also, mechanical properties are deteriorated at higher concentrations of CNTs due to agglomeration [14].

Powder metallurgy technique has been widely used for synthesis of aluminum and copper-CNTs composites majorly. It is also been used to fabricate Ni, Mg, Ti, Au, Sn and its alloys with CNT reinforcement. The powder metallurgy technique becomes very flexible to fabricate CNTs composite because its quality of dispersion and its manly depends on the matrix particle size. Liquid media can be used for the processing of matrix and the CNT where it prevents the oxidation and controls the heat generation during processing. The consolidation of these powder precursors was carried out through various methods. Cu-CNT composite processed through ball milling followed by isostatic pressing and sintering at 800°C for 2 h are found to be least porosity (2.4%). Ball milling process shown to be effective process in producing an Al-CNT composites [15, 16] and also this process is used for process Si-CNT composite powders for Li-ion batteries [17]. Silver-CNT composites were blended and compacted at 320 MPa and sintered at 700°C. Thus developed composites exhibited uniform distribution of CNTs without agglomeration of CNT at 8 wt% in the matrix.

Use of pressure to the dies containing a matrix and reinforcement precursor during sintering results in dense compact. This operation was done in inert atmosphere as well as vacuum conditions for metal matrix-CNT composites. Al-CNTs composites were fabricated through hot pressing found to be agglomeration of CNT. Also, the process leads to formation of carbide compounds. Further, precursors are also processed through ultrasonic dispersion of CNT in alcoholic media and isostatic pressing leads no chemical reaction between the SWCNT and aluminum. Cu-CNT was hot pressed after ball milling the powder at 1100°C in graphite die successfully. Mg-CNT [16] and Ti-CNT [17] combinations are also prepared through hot pressing in vacuum conditions which results in CNT agglomeration [18].

Spark plasma sintering (SPS) or electric field assisted sintering (EFAS) was found to be different from hot pressing and the heat was generated by pulsed DC current which is passed to powder kept in die. Great improvement in the compressive strength of Cu-10 vol% CNTs composite was observed for SPS processed compacts [19]. Improvement in hardness and sliding wear resistance were observed for the various metal matrix-CNT composites. SPS processed Al-1 wt% CNTs compacts are exhibited slight improvement in the hardness, flexural and improvement in the wear resistance. Compared to other conventional process SPS process became a promising method to obtain high density metal matrix-CNT composites. Other advantage was small sintering time which ensures the minimal reaction of the CNT with matrix component during consolidation [20].

Density of the metal matrix-CNTs compacts can be increased by deformation process and the method was suitable for aluminum- and copper-based composites. Hot extrusion is the commonly used deformation technique for metal matrix-CNTs composite. Equal channel angular extrusion (ECAE) and cold rolling are the other deformation techniques to process the composites. Aluminum and CNTs powders are processed through ultra-sonication in ethanol followed by drying, compaction and extrusion at 500°C with an extrusion ratio 25:1 [21]. In the other case, aluminum-CNT mixtures were ultra-sonicated and ball milled followed by sintering (580°C) and extrusion at 560°C successfully [30]. During deformation, CNT clusters are broken and are aligned in the direction of shear stress. Efforts have been made to process Mg-CNT and Mg-SiC-CNT composites through hot extrusion and 36% improvement in the yield strength was observed [22, 23]. Au-Sn-Cu solders with 1 wt% SWCNTs produced through hot extrusion shown 18% increase in the tensile strength [24].

Disintegrated melt deposition (DMD) was used to improve the CNT dispersion. This was carried out to fabricate Mg-CNT composite [25] where, the molten Mg-2 wt% CNT at 750°C is made to pass through an orifice and was disintegrated by two argon jets. Thus disintegrated molten melt is deposited in the metallic mold and thus obtained ingot is extruded at 350°C to get the Mg-CNT rods. Improvement in strength and ductility was observed for such fabricated materials. Also, increase in the content of CNTs affected the fatigue performance by reducing the number of cycle due to presence of voids and the matrix-CNT interface [26].

Melt filtration method was the commonly used technique to develop the Metal matrix composite. This method enables the high chances of homogeneous distribution of CNTs in the metal matrix. The key factor in this method includes proper filling up of pores and that constitute the final dense of the product. Mg-CNT was prepared in this manner and found to be enhanced in the shear modulus [27]. Aluminum-CNT mixtures were ball milled (7 h at 300 rpm) and compacted to make preform. Thus prepared preform was infiltrated spontaneously by LY12 Aluminum alloy at 800°C in nitrogen atmosphere and core shell type microstructure developed in the preform. Such a type of an infiltrated composite with 20 vol% of CNT showed a decrease in wear rate and the coefficient of friction. The decrease in the coefficient of friction was seen up to 15 vol% of CNT [27]. Melt infiltration is quite economical method to fabricate composite with CNT combination and properties are completely rely on degree of homogeneity of the CNT in the matrix. Further, due to partial melting of the matrix in connection with the CNTs lead to inevitable reactions and that can be prevented through surface coatings methods.

Thermal spray was used in many mass production industries. In this process the material to be subjected to spraying is fed into the heating source in the form of wire or powder and it get melted. Thus melted molten metal was accelerated by carrier inert gas and impinged on the substrate. Splats are formed on the substrate in the form of layer by layer and accumulation of these slats became a coating. Such a method was used to synthesis of ceramic-CNT [28, 29] and metal-CNT [30, 31] composite. Once the CNTs were uniformly distributed within the single splats, then the complete composite structure which was built layer over layer will also have CNTs homogeneous distribution. Thus, the near net shaped metal-CNT composite structures can be produced for the real time applications such as aerospace and heavy machinery surfaces with reasonable corrosion and wear resistance.

Plasma spraying forming (PSF) was carried out for Al-Si alloys reinforced with CNTs [30]. Blending was carried out through ball milling process and the mixed powders are plasma sprayed. The spraying process was done through cryogenically cooling environment on AA 6061 aluminum mandrel. Further, the current proved the retaining the CNT structure at higher temperature and there no carbide formation. Also, it was inferred that the sintering did not produced any perceptible damage to the CNT structure. Thus produced composite exhibited 78% increase in the elastic modulus for the 10 wt% of CNTs [32].

High Velocity Oxy-Fuel Spraying (HVOF) was found to be other novel thermal spray method which uses the heat source from the combustion of fuels in oxygen. Al-10 wt% composite produced through this method exhibited 49% improvement in the elastic modulus and 17% improvement in the microhardness which was more compared to same composite produced through PSF [30]. HVOF process has the capability to produce metal matrix-CNTs composite with high homogeneous dispersion, which enhances the mechanical properties.

Cold spraying method accelerates the powder particle to high velocity and made to impact on the substrate which leads to formation of splats. Al-CNT composite coating was prepared from the blended pure aluminum powders from this method and composite observed to be a dance microstructure [31]. But, CNTs were shortened due to high impact shearing between the particles. Also, necking formation followed by cup and cone type of fracture observed for mild carbon steel and CNT composites [33].

Electrochemical route can be used to synthesis MWCNT composites as well thin films by material deposition. Most of the composites are processed through co-deposition of CNTs and metals-ions [34]. Uniform distribution and homogeneous distribution of CNTs can be achieved in this technique [35]. This method also has flexibility to fabricate CNTs-based one-dimensional (1D) composites [36]. Thus developed composite has an application for nanosensors and precursor for larger MWCNT composite structures. The processing parameters govern the nature of the structures and also different in both electroless deposition and electrochemical deposition technique. Current density and type of power source (AC or DC) plays an important role in case of electrodeposition which was directly proportional to deposition of CNTs. On the other hand pH value and bath temperature are the important key factors in case of thermochemical process which determines the coating composition and morphology of the developed composite. Thus, electroless deposition and electrodeposition have become an effective method to produce thin metal matrix composite and coating techniques. Ni, Cu, Zn and Cr along with CNT combination composite coatings and thin films system were studied so far.

Sputtering method was used to deposit the metal over CNTs. This method was suitable for fabricating the one dimensional (1D) nanostructured composite. Further, sputtering technique enables the alignment of CNTs in the developed composite. Deposition of aluminum on CNTs was carried out by the magnetron sputtering and subjected to various annealing treatment [37]. Sputtering method carried out for Au on SWCNT shows the self-organization and evenly spaced cluster [37]. Sandwich method involves the dispersing of CNTs between many thin metallic or alloy layers followed by cold weld with the application of pressure. This method was successfully used to fabricate Cu-SWCNT composites and good dispersion along with proper bonding was observed [38]. Aluminum-CNT composite also processed by spray deposition which was carried out by spraying CNT on aluminum foil and rolling. Nearly, 59% improvement in the elastic modulus for the Al-2 vol% was observed for such a developed composite.

In the friction stirring process, frictional force was used to weld the metal and the MWCNT composite. This method was used to process the Mg-CNT and Al-CNT composite successfully. The decrease in the grain size was observed due to incorporation of carbon nanotube through this process. Processing of Al-5 wt% SWCNT through this method resulted in the reduction of grain size up to be 80% [39].

4.5. Graphene-metal matrix composite

The explanation of graphene covers all forms of graphitic material from 100 nm < thick platelets down to single layer graphene [40]. However, the obtainability of single-or few-layer graphene that has caused the interest. In fact, it is possible to distinguish between flakes of graphene with different numbers of atomic layers in a transmission optical microscope due to its nature of significant optically energetic [41]. The work to determine the number of layers to be used for the reinforcement was formed and found that monolayer has the higher stress transfer than the bilayer graphene [42] and the flakes are sufficiently large(>30 micro meter) and aspect ratio should be high for the effective reinforcement of both bilayer [43] and monolayer graphene in the composite [44]. There has already been considerable effort put into the development routes of preparing high-quality graphene in large quantities for the research purposes along with the view to possible applications where it is suitable [45]. There are number of motives to develop graphene-metal composites. The strengthening mechanism of graphene reinforcement was thought to be related to the excellent mechanical and the unique structured characteristics of graphene, and good bonding interfaces between graphene and matrix. There are many challenges involved to get graphene dispersed metal matrix composite with the existing conventional metallurgical process or methods due to huge density difference between graphene nanoflakes (GNFs) and metal matrix, more interfacial contact area than carbon nanotubes and also reaction at matrix reinforcement interface [46] because the metals are much reactive. The work relating to this field is still remaining in their infancy. But the increase of publications in this category signifies that growing an interest toward graphene-based metal composites. Research on development of metal-graphene composites is still in its infancy stage as compared to polymer-graphene and ceramic-graphene composites. The metal matrix composites incorporated with the secondary phase graphene includes aluminum, magnesium, nickel, platinum [47], gold [48], cobalt [49], palladium [50], and silicon [51]. Further, these composites found to be application in supercapacitors [52], energy devices (batteries) [52], electrocatalysts and biosensors [53].

4.6. Processing methods of graphene-metal matrix composite

Powder metallurgy route was the commonly used technique for processing of graphene-based Cu, Al, Mg, etc., and alloys composites. It consists of processing of graphene with the metal or alloy powder followed by compaction and sintering. Usually dispersion and compaction is done through various methods. This step will have a great influence on final densification and properties of the developed composite. The common problem associated with the graphene includes agglomeration and it requires high energy to overtake the surface energy of the graphene to make it single flake. Further, high energy was utilized to break the graphene interlayer van der Waals force to obtain an individual sheet of graphene. In many cases graphene has been processed through ball milling and ultrasonication in order to disperse it into the matrix material. During the preparation of graphene-metal matrix composite, dimethylformamide (DMF), isopropanol, N-methyl pyrrolidone (NMP), deionized water and acetone was utilized as liquid media for ball milling.

Wet chemistry method utilizes the ultrasonication for mixing of matrix and graphene flakes in a liquid media. Sound waves generated during Ultrasonication are used to induce cavitation followed by agitating the particles in liquid media. Tip and bath sonicator are the commonly used ultrasonication devices for processing the graphene-metal powder mixtures. Ultrasonication processes will not use an impact or shear force on graphene sheets unlike ball milling and there is no particle size reduction during processing. Further, wet chemistry method completely eliminates the contamination issues during processing, except from the liquid media. Also, wet chemistry and the ball milling can be combined to process the metal and graphene precursors [54].

Mechanical alloying method was the most commonly used technique for fabrication of the metal-/alloy-based composite. The commonly used metals to fabricate the composite incorporating with the graphene includes: copper (Cu), aluminum (Al) and magnesium (Mg), etc. During alloying, the milling process was carried out to refine the metal or alloy powder in the milling media. Further, the milling process produces the repeated cold welding, re-welding and fracture of the metallic powders. Thus, it leads to simultaneous strengthening during milling by grain refining and work hardening. Microstructure of the composite can be controlled by modification of milling process parameters such as time, milling ratio and media. ZrO_2 [55] are the commonly used balls for mechanical alloying of Al-graphene powder in a milling jar. The quantity of graphene added for the metal powder is typically <12 wt% so far. Further, milling process was carried out usually in argon (Ar) atmosphere to control the oxidation. Methanol, cryomilling and petroleum ether are the commonly involved process control agents during milling. Also, increasing in the milling time will degrade the properties of graphene leading to formation of defects in the developed composites. Additionally, hardness and strength of the graphene-MMCs fabricated via ball-milling followed by compaction and sintering are improved due to improved interfacial reaction, bonding and grain refinement.

Hot extrusion follows a hot working process; it requires a large quantity of powder and preparatory process (ball milling, compaction and sintering) to make a billet to extrude. For aluminum-graphene composites, the prepared billets are heated to >500°C which may lead to carbide formation at the metal graphene interfaces which reduces the strength of the composite. Most of the research has been carried out using spherical shaped aluminum powder

(1–22 μm). But, it is observed that nanoflake size matrix possesses a great compatibility with the graphene and significant improvement in the properties was observed. graphene synthesized through chemically, thermally exfoliated and hummer's method are used to fabricate the composite through hot extrusion. Some of the studies used slurry blending technique in which the ethanol or acetone is used as the medium. Thus processed metal matrix and graphene mixtures are consolidated through hydraulic pressing or hot isostatic pressing (HIP) and sintered at <600°C in argon (Ar) atmosphere followed by extrusion [56].

The metal (Al, Mg)/graphene composite produced through hot extrusion possess densities close to theoretical densities. Further, nanofiller graphene and the metallic grains are aligned along the direction of extrusion. Most of the graphene-MMCs, synthesized through hot extrusion, exhibit an improvement in strength, fracture toughness and hardness. Al-graphene composites extruded at a temperature less than 500°C possess a drastic improvement in the properties and it was found that they are defect free. Also, optimized graphene content for the aluminum matrix induce the extreme strength and larger grain refinement in the developed composite. Further, optimized graphene content in the matrix prevents the agglomeration which helps in preventing the carbide formation sites [57].

Hot rolling involves a combination of ball milling (high energy) and rolling which was used to fabricate the graphene-metal matrix composite effectively. The metal particle size range of 20–200 μm with 97–99.7% purity was considered in the studies. Thus processed powder mixtures were compacted in a thin copper (Cu) tube and subjected to rolling. Usually high speed differential rolling (HSDR) or equal speed rolling (ESR) is used and HSDR exhibited a larger amount of deformation]. Solid state friction stirring procedure same as friction stir welding. The process uses a non-consumable rotating tool which was hold mechanically by the rotating head and stirs the material. The main challenge in case of graphene/metal matrix system was the huge aspect ratio and small thickness will lead to agglomeration during the surface processing. In addition, a novel combination of liquid state solid stirring followed by friction stir processing to fabricate graphene/metal composite. Lot of agglomeration was found in the current method [58].

Graphene oxide reduction to graphene during chemical mixing was used to form a composite. This method was applied to develop many composite including palladium, platinum, cobalt, gold, etc. In the chemical mixing method solution media was used to disperse GO and metal particles during the synthesis [59]. During the process metal nanoparticles absorbed on the GO flakes and subjected to catalytic reduction reaction of GO with the solution and form a metal-graphene composite. This method enables the metal particle to sit over the reduced graphene nanoflakes and prevents the agglomeration and restacking. Chemical mixing of graphene with metal uses a metallic salts and graphene as a starting material. During the process, metallic salts are reduced in to the solvent and deposited on the graphene sheets to form a composite. The process prevents the agglomeration of the graphene flakes by developing a nonosized metallic particle between each graphene layers.

5. Conclusion

Most of the researchers have discussed the positive aspects of graphene reinforced composites, the extensive property of graphene and its huge potential for industrial applications. Due

to the 2D structure and high specific surface area (SSA) of the graphene, it has several typical and intrinsic merits over the other reinforcements to incorporate in matrix for developing the composite structure. Graphene with very low content addition to the matrix showed a break through improvement and evolved as effective reinforcement for the material over high content particulate and CNT-based reinforcement composite system.

Author details

Prashantha Kumar HG* and Anthony Xavior M

*Address all correspondence to: prashanthakumar.hg@gmail.com

School of Mechanical Engineering, VIT University, Vellore, TN, India

References

[1] Shenogin S, Xue L, Ozisik R, Keblinski P, Cahill DG. Role of thermal boundary resistance on the heat flow in carbon-nanotube composites. Journal of Applied Physics. 2004;**95**(12):8136-8144. DOI: 10.1063/1.1736328

[2] Bhat DG, Johnson DG, Malshe AP, Naseem H, Brown WD, Schaper LW, Shen CH. A preliminary investigation of the effect of post-deposition polishing of diamond films on the machining behavior of diamond-coated cutting tools. Diamond and Related Materials. 1995;**4**(7):921-929. DOI: 10.1016/0925-9635(94)00251-7

[3] Ma PC, Siddiqui NA, Marom G, Kim JK. Dispersion and functionalization of carbon nanotubes for polymer-based nanocomposites: A review. Composites Part A: Applied Science and Manufacturing. 2010;**41**(10):1345-1367. DOI: 10.1016/j.compositesa.2010.07.003

[4] Bamini NS, Vidyalakshmy Y, Choedak T, Kejalakshmy N, Muthukrishnan P, Ancy CJ. Synthesis, linear optical, non-linear optical, thermal and mechanical characterizations of dye-doped semi-organic NLO crystals. Materials Research Express. 2015;**2**(6):065010. DOI: 10.1088/2053-1591/2/6/065010

[5] Iijima S. Carbon nanotubes: past, present, and future. Physica B: Condensed Matter. 2002;**323**(1-4):1-5. DOI: 10.1016/S0921-4526(02)00869-4

[6] Szuecs F, Kim CP, Johnson WL. Mechanical properties of Zr56. 2Ti13. 8Nb5. 0Cu6. 9Ni5. 6Be12. 5 ductile phase reinforced bulk metallic glass composite. Acta Materialia. 2001;**49**(9):1507-1513. DOI: 10.1016/S1359-6454(01)00068-4

[7] Danafar F, Fakhru'l-Razi A, Salleh MAM, Biak DRA. Fluidized bed catalytic chemical vapor deposition synthesis of carbon nanotubes—A review. Chemical Engineering Journal. 2009;**155**(1-2):37-48. DOI: 10.1016/j.cej.2009.07.052

[8] Vaisman L, Wagner HD, Marom G. The role of surfactants in dispersion of carbon nanotubes. Advances in Colloid and Interface Science. 2006;**128**:37-46. DOI: 10.1016/j.cis.2006.11.007

[9] Yuen SM, Ma CCM, Chuang CY, Yu KC, Wu SY, Yang CC, Wei MH. Effect of processing method on the shielding effectiveness of electromagnetic interference of MWCNT/PMMA composites. Composites Science and Technology. 2008;**68**(3-4):963-968. DOI: 10.1016/j.compscitech.2007.08.004

[10] Narten AH, Danford MD, Levy H. X-ray diffraction study of liquid water in the temperature range 4-200°C. Discussions of the Faraday Society. 1967;**43**:97-107. DOI: 10.1039/DF9674300097

[11] Maria AJ, Kurtycz A, Olszyna RA. Recent advances in graphene family materials toxicity investigations. Journal of Nanoparticle Research. 2012;**4**(12):1320. DOI:10.1007/s11051-012-1320-8

[12] Pop E, Varshney V, Roy AK. Thermal properties of graphene: Fundamentals and applications. MRS Bulletin. 2012;**37**(12):1273-1281. DOI: 10.1557/mrs.2012.203

[13] Sudagar J, Lian J, Sha W. Electroless nickel, alloy, composite and nano coatings–A critical review. Journal of Alloys and Compounds. 2013;**571**:183-204. DOI: 10.1016/j.jallcom.2013.03.107

[14] Thostenson ET, Li C, Chou TW. Nanocomposites in context. Composites Science and Technology. 2005;**65**(3-4):491-516. DOI: 10.1016/j.compscitech.2004.11.003

[15] Srinivasa RB, Lahiri D, Agarwal A. Carbon nanotube reinforced metal matrix composites-a review. International materials reviews. 2010;**55**(1):41-64. DOI.org/10.1179/095066009X12572530170543

[16] Esawi AMK, Morsi K, Sayed A, Taher M, Lanka S. Effect of carbon nanotube (CNT) content on the mechanical properties of CNT-reinforced aluminium composites. Composites Science and Technology. 2010;**70**(16):2237-2241. DOI: 10.1016/j.compscitech.2010.05.004

[17] Liu XM, Dong Huang Z, Woon Oh S, Zhang B, Ma PC, Yuen MM, Kim JK. Carbon nanotube (CNT)-based composites as electrode material for rechargeable Li-ion batteries: A review. Composites Science and Technology. 2012;**72**(2):121-144. DOI: 10.1016/j.compscitech.2011.11.019

[18] Llorca-Isern N, Artieda-Guzmán C. Metal-based composite powders. In Advances in Powder Metallurgy, Woodhead Publishing Series in Metals and Surface Engineering. 2013. pp. 241-272. DOI.org/10.1533/9780857098900.2.241

[19] Shukla AK, Nayan N, Murty SVSN, Sharma SC, Chandran P, Bakshi SR, George KM. Processing of copper-carbon nanotube composites by vacuum hot pressing technique. Materials Science and Engineering: A. 2013;**560**:365-371. DOI: 10.1016/j.msea.2012.09.080

[20] Salama E. Tensile and Fracture Behavior of Single and Dual Matrix Aluminum-Carbon Nanotube Composites. 2013. Available from: http://dar.aucegypt.edu/handle/10526/3597

[21] Ramesh KT. Nanomaterials. In: Nanomaterials. Boston, MA: Springer; 2009. pp. 1-20. DOI: 10.1007/978-0-387-09783-1

[22] Goh CS, Wei J, Lee LC, Gupta M. Development of novel carbon nanotube reinforced magnesium nanocomposites using the powder metallurgy technique. Nanotechnology. 2005;**17**(1):7. DOI: 10.1088/0957-4484/17/1/002

[23] Thakur SK, Kwee GT, Gupta M. Development and characterization of magnesium composites containing nano-sized silicon carbide and carbon nanotubes as hybrid reinforcements. Journal of Materials Science. 2007;**42**(24):10040-10046. DOI: 10.1007/s10853-007-2004-0

[24] Kumar KM, Kripesh V, Tay AA. Single-wall carbon nanotube (SWCNT) functionalized Sn-Ag-Cu lead-free composite solders. Journal of Alloys and Compounds. 2008;**450**(1-2):229-237. DOI: 10.1016/j.jallcom.2006.10.123

[25] Goh CS, Wei J, Lee LC, Gupta M. Simultaneous enhancement in strength and ductility by reinforcing magnesium with carbon nanotubes. Materials Science and Engineering: A. 2006;**423**(1-2):153-156. DOI: 10.1016/j.msea.2005.10.071

[26] Goh CS, Wei J, Lee LC, Gupta M. Ductility improvement and fatigue studies in Mg-CNT nanocomposites. Composites Science and Technology. 2008;**68**(6):1432-1439. DOI: 10.1016/j.compscitech.2007.10.057

[27] Zhou SM, Zhang XB, Ding ZP, Min CY, Xu GL, Zhu WM. Fabrication and tribological properties of carbon nanotubes reinforced Al composites prepared by pressureless infiltration technique. Composites Part A: Applied Science and Manufacturing. 2007;**38**(2):301-306. DOI: 10.1016/j.compositesa.2006.04.004

[28] Balani K, Anderson R, Laha T, Andara M, Tercero J, Crumpler E, Agarwal A. Plasma-sprayed carbon nanotube reinforced hydroxyapatite coatings and their interaction with human osteoblasts in vitro. Biomaterials. 2007;**28**(4):618-624. DOI: 10.1016/j.biomaterials.2006.09.013

[29] Keshri AK, Huang J, Singh V, Choi W, Seal S, Agarwal A. Synthesis of aluminum oxide coating with carbon nanotube reinforcement produced by chemical vapor deposition for improved fracture and wear resistance. Carbon. 2010;**48**(2):431-442. DOI: 10.1016/j.carbon.2009.08.046

[30] Laha T, Agarwal A, McKechnie T, Seal S. Synthesis and characterization of plasma spray formed carbon nanotube reinforced aluminum composite. Materials Science and Engineering: A. 2004;**381**(1-2):249-258. DOI: 10.1016/j.msea.2004.04.014

[31] Bakshi SR, Singh V, Seal S, Agarwal A. Aluminum composite reinforced with multiwalled carbon nanotubes from plasma spraying of spray dried powders. Surface and Coatings Technology. 2009;**203**(10-11):1544-1554. DOI: 10.1016/j.surfcoat.2008.12.004

[32] Laha T, Chen Y, Lahiri D, Agarwal A. Tensile properties of carbon nanotube reinforced aluminum nanocomposite fabricated by plasma spray forming. Composites Part A: Applied Science and Manufacturing. 2009;**40**(5):589-594. DOI: 10.1016/j.compositesa.2009.02.007

[33] Bakshi SR, Singh V, McCartney DG, Seal S, Agarwal A. Deformation and damage mechanisms of multiwalled carbon nanotubes under high-velocity impact. Scripta Materialia. 2008;**59**(5):499-502. DOI: 10.1016/j.scriptamat.2008.04.035

[34] Tan J, Yu T, Xu B, Yao Q. Microstructure and wear resistance of nickel–carbon nanotube composite coating from brush plating technique. Tribology Letters. 2006;**21**(2):107-111. DOI: 10.1007/s11249-006-9025-8

[35] Chai Y, Zhang K, Zhang M, Chan PC, Yuen MM. Carbon nanotube/copper composites for via filling and thermal management. In: Electronic Components and Technology Conference, 2007. ECTC'07. Proceedings. 57th. IEEE; 2007, May. pp. 1224-1229. DOI: 10.1109/ECTC.2007.373950

[36] Dingsheng YUAN, Yingliang L. Electroless deposition of Cu on multiwalled carbon nanotubes. Rare Metals. 2006;**25**(3):237-240. DOI: 10.1016/S1001-0521(06)60046-6

[37] Huang W, Chen H, Zuo JM. One-dimensional self-assembly of metallic nanostructures on single-walled carbon-nanotube bundles. Small. 2006;**2**(12):1418-1421. DOI: 10.1002/smll.200600241/full

[38] Li YH, Housten W, Zhao Y, Zhu YQ. Cu/single-walled carbon nanotube laminate composites fabricated by cold rolling and annealing. Nanotechnology. 2007;**18**(20):205607. DOI: 10.1088/0957-4484/18/20/205607

[39] Lim DK, Shibayanagi T, Gerlich AP. Synthesis of multi-walled CNT reinforced aluminium alloy composite via friction stir processing. Materials Science and Engineering: A. 2009;**507**(1-2):194-199. DOI: 10.1016/j.msea.2008.11.067

[40] Jang BZ, Zhamu A. Processing of nanographene platelets (NGPs) and NGP nanocomposites: A review. Journal of Materials Science. 2008;**43**(15):5092-5101. DOI: 10.1007/s10853-008-2755-2

[41] Blake P, Hill EW, Castro Neto AH, Novoselov KS, Jiang D, Yang R. Booth TJ, Geim AK. Making graphene visible. Applied Physics Letters. 2007;**91**(6):063124. DOI: doi/abs/10.1063/1.2768624

[42] Gong L, Young RJ, Kinloch IA, Riaz I, Jalil R, Novoselov KS. Optimizing the reinforcement of polymer-based nanocomposites by graphene. ACS Nano. 2012;**6**(3):2086-2095. DOI: 10.1021/nn203917d

[43] Frank O, Bouša M, Riaz I, Jalil R, Novoselov KS, Tsoukleri G, et al. Phonon and structural changes in deformed Bernal stacked bilayer graphene. Nano Letters. 2011;**12**(2):687-693. DOI: doi/abs/10.1021/nl203565p

[44] Hernandez Y, Nicolosi V, Lotya M, Blighe FM, Sun Z, De S, et al. High-yield production of graphene by liquid-phase exfoliation of graphite. Nature Nanotechnology. 2008;**3**(9):563. DOI: 10.1038/nnano.2008.215

[45] Rao CEE, Sood AE, Subrahmanyam KE, Govindaraj A. Graphene: The new two-dimensional nanomaterial. Angewandte Chemie International Edition. 2009;**48**(42):7752-7777. DOI: 10.1002/anie.200901678/full

[46] Kumar HP, Xavior MA. Graphene reinforced metal matrix composite (GRMMC): A review. Procedia Engineering. 2014;**97**:1033-1040. DOI: 10.1016/j.proeng.2014.12.381

[47] Hu Y, Jin J, Wu P, Zhang H, Cai C. Graphene-gold nanostructure composites fabricated by electrodeposition and their electrocatalytic activity toward the oxygen reduction and glucose oxidation. Electrochimica Acta. 2010;**56**(1):491-500. DOI: 10.1016/j.electacta.2010.09.021

[48] Yang S, Cui G, Pang S, Cao Q, Kolb U, Feng X, Müllen K. Fabrication of cobalt and cobalt oxide/graphene composites: Towards high-performance anode materials for lithium ion batteries. ChemSusChem. 2010;**3**(2):236-239. DOI: 10.1002/cssc.200900106/full

[49] Xu C, Wang X, Zhu J. Graphene-metal particle nanocomposites. The Journal of Physical Chemistry C. 2008;**112**(50):19841-19845. DOI: 10.1021/jp807989b

[50] Chou SL, Wang JZ, Choucair M, Liu HK, Stride JA, Dou SX. Enhanced reversible lithium storage in a nanosize silicon/graphene composite. Electrochemistry Communications. 2010;**12**(2):303-306. DOI: 10.1016/j.elecom.2009.12.024

[51] Si Y, Samulski ET. Exfoliated graphene separated by platinum nanoparticles. Chemistry of Materials. 2008;**20**(21):6792-6797. DOI: 10.1021/cm801356a

[52] Li Y, Tang L, Li J. Preparation and electrochemical performance for methanol oxidation of Pt/graphene nanocomposites. Electrochemistry Communications. 2009;**11**(4):846-849. DOI: 10.1016/j.elecom.2009.02.009

[53] Song B, Li D, Qi W, Elstner M, Fan C, Fang H. Graphene on Au(111): A highly conductive material with excellent adsorption properties for high-resolution bio/nanodetection and identification. Chemphyschem. 2010;**11**(3):585-589. DOI: 10.1002/cphc.200900743

[54] Li S, Wang Y, Lai C, Qiu J, Ling M, Martens W, et al. Directional synthesis of tin oxide@ graphene nanocomposites via a one-step up-scalable wet-mechanochemical route for lithium ion batteries. Journal of Materials Chemistry A. 2014;**2**(26):10211-10217. DOI: 10.1039/C4TA01131G

[55] Suryanarayana C. Mechanical alloying and milling. Progress in Materials Science. 2001;**46**(1-2):1-184. DOI: 10.1016/S0079-6425(99)00010-9

[56] Liu J, Khan U, Coleman J, Fernandez B, Rodriguez P, Naher S, Brabazon D. Graphene oxide and graphene nanosheet reinforced aluminium matrix composites: Powder synthesis and prepared composite characteristics. Materials & Design. 2016;**94**:87-94. DOI: 10.1016/j.matdes.2016.01.031

[57] Rashad M, Pan F, Tang A, Asif M. Effect of graphene nanoplatelets addition on mechanical properties of pure aluminum using a semi-powder method. Progress in Natural Science: Materials International. 2014;**24**(2):101-108. DOI: 10.1016/j.pnsc.2014.03.012

[58] Maurya R, Kumar B, Ariharan S, Ramkumar J, Balani K. Effect of carbonaceous reinforcements on the mechanical and tribological properties of friction stir processed Al6061 alloy. Materials & Design. 2016;**98**:155-166. DOI: 10.1016/j.matdes.2016.03.021

[59] Lambert TN, Chavez CA, Hernandez-Sanchez B, Lu P, Bell NS, Ambrosini A, Huber DL. Synthesis and characterization of titania-graphene nanocomposites. The Journal of Physical Chemistry C. 2009;**113**(46):19812-19823. DOI: 10.1021/jp905456f

Chapter 4

Analytical Description of the Pore Structure of Porous Powder Materials

Victor Maziuk

Additional information is available at the end of the chapter

http://dx.doi.org/10.5772/intechopen.76712

Abstract

In this chapter, we propose a method for the analytical description of the porous powder materials' (PPMs) pore distribution based on the pore structure data obtained by mercury porosimetry. The mercury porosimetry method is mostly informative and reliable when speaking about the recurrence of results as compared with other methods of pore distribution investigation. In this chapter, we present a calculation method of correcting experimental data of mercury porosimetry, based on the presentation of a porous body by a statistical model of a serial type.

Keywords: porous powder material, pore volume distribution on size, average hydraulic pore size, mercury porosimetry, statistical model of porous body

1. Introduction

Consistent with the multiple functions performed by porous powder materials (PPMs) in various technical devices, a variety of computational methods were developed to assess the effectiveness of the PPMs' varying pore structure. The relevant calculations use characteristics of the pore structure of the PPMs determined experimentally. The pore volume distribution on size and the average hydraulic pore size are considered as main, most common, characteristics of the pore structure. In this chapter, we propose a method for the analytical description of the PPMs' pore distribution based on the pore structure data obtained by mercury porosimetry. The mercury porosimetry method is mostly informative and reliable when speaking about recurrence of results as compared with other methods of pore distribution investigation. However, a pore distribution function provided by this method has a distorted character. It increases the volume of small pores that is provided by the narrowing and widening of pore

channels on the way of mercury travel. In this chapter, we present a calculation method of correcting experimental data of mercury porosimetry, based on the presentation of a porous body by a statistical model of a serial type.

2. Analytical description of the pore structure

Mercury porosimetry is the most accurate and informative method of studying the pore volume distribution on size. The essence of this method consists of measuring the quantity of mercury pressed in the pre-evacuated porous material, depending on the applied external pressure [1].

Mercury porosimeter operates as follows. The test sample is placed in a sealed cell which is evacuated; simultaneously the sample is degassed. Then, mercury is introduced into the cell so that mercury completely closes the sample. The mercury is automatically subjected to a predetermined pressure, which is left for a certain time so that the mercury fills all the pores that have the size larger than the critical value. At each table pressure value, the volume of mercury, which went down in the pores of the sample, is measured with a permittance method. According to the experimental data, the integral

$$F(d) = \frac{V(d)}{V_0} \tag{1}$$

and the differential

$$f(d) = -\frac{1}{V_0}\frac{dV(d)}{dd} \tag{2}$$

functions of pore volume distribution on size are calculated. Here $V(d)$—the volume of mercury—went down into the sample at the pressure corresponding to the critical pore size d; V_0—the total amount of mercury—went down into the sample at the maximal pressure.

For processing the experimental data, the following technique was developed. Because usually the minimum and maximum pore sizes of the PPMs differ by 1–2 orders of magnitude; the logarithmically uniform pressure table is pre-assigned that corresponds to the logarithmically uniform sequence of pore size values ${d_0}^T, {d_1}^T, \ldots, {d_N}^T$:

$$\frac{{d_i}^T}{{d_{i-1}}^T} = const, \quad i = 1, \ldots, N. \tag{3}$$

However, because the automatically applied pressure is not exactly equal to the table value, and may differ from it by 1.5%, the real critical pore sizes d_i coincide with the table values with the same deviation:

$$d_i = {d_i}^T \pm 0.015{d_i}^T, \quad i = 0, \ldots, N. \tag{4}$$

According to the obtained values of the volume of mercury which went down into the sample V_0, V_1, …, V_N, integral function of pore distribution is approximated by a finite Fourier series [2]. As a first approximation, the volume V_i is deemed as related to the values of pore size distributed logarithmically evenly between d_0 and d_N and equal to $d_0(d_N/d_0)^{i/N}$, $i = 0, \ldots, N$. Assuming

$$V_{2N-i} = V_i, \quad i = 1, \ \ldots, \ N, \tag{5}$$

the volume values are calculated in the points d_i by the approximating function:

$$V_i^{(j)} = \frac{a_0^{(j)}}{2} + \sum_{k=1}^{N-1} a_k^{(j)} \cos \frac{\pi k \ln \frac{d_i}{d_0}}{\ln \frac{d_N}{d_0}} + (-1)^N \frac{a_N^{(j)}}{2}, \quad i = 0, \ \ldots, \ N, \tag{6}$$

where

$$a_k^{(j)} = \frac{1}{N} \sum_{m=0}^{2N-1} y_m^{(j)} \cos \frac{\pi m k}{N}, \quad k = 0, \ \ldots, \ N; j = 1, \ \ldots, \ J. \tag{7}$$

In the last expression in the first approximation, as it was said,

$$y_m^{(1)} = V_m, \quad m = 0, \ \ldots, \ 2N - 1, \tag{8}$$

and successive approximation of the volume values in the points d_i is given by the approximating function to the experimental values provided by the next iteration:

$$y_m^{(j)} = y_m^{(j-1)} + V_m - V_m^{(j-1)}, \quad m = 0, \ \ldots, \ 2N - 1; j = 2, \ \ldots, \ J. \tag{9}$$

A satisfactory accuracy of the approximation of the experimental results (deviation less than 1%) is usually achieved when the number of iterations is $J = 5$. Obtained values of the expansion coefficients $a_k^{(J)}$ allow one to calculate the approximating function of pore volume distribution on size for any values of the pore size $d_0 \le d \le d_N$ by the expression:

$$F(d) = \frac{1}{V_0} \left(\frac{a_0^{(j)}}{2} \right) + \sum_{k=1}^{N-1} a_k^{(j)} \cos \frac{\pi k \ln \frac{d}{d_0}}{\ln \frac{d_N}{d_0}} + (-1)^N \frac{a_N^{(j)}}{2}. \tag{10}$$

It is easy to obtain the expression for the approximating differential function by differentiating the last expression:

$$f(d) = \frac{1}{V_0} \frac{\pi}{d \ln \frac{d_N}{d_0}} \sum_{k=1}^{N-1} k a_k^{(j)} \sin \frac{\pi k \ln \frac{d}{d_0}}{\ln \frac{d_N}{d_0}}. \tag{11}$$

Figures 1 and **2** show the processed, accordingly described, technique data on the experimental study of pore volume distribution on size of the PPMs obtained by sintering a freely poured copper powder PMS-N with a particle size from −315 to 200 μm.

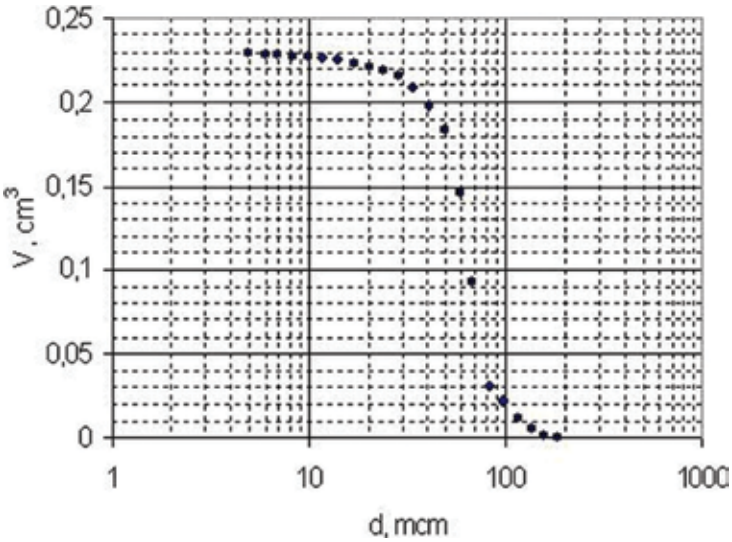

Figure 1. The results of the experimental investigation of volume pore distribution on size of sintered copper PMS-N. Particle size (−315 to +200) mm, sample weight 1.7 g.

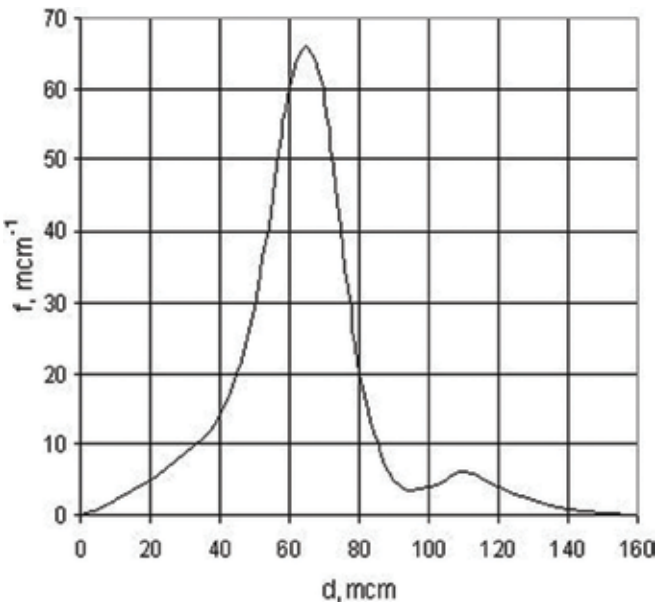

Figure 2. The approximating differential function of pore volume distribution on size of sintered copper.

The average hydraulic pore size characterizes the transport and evaporative capacity of the PPMs at full saturation of its pore space with working fluid. Experimental determination of the average hydraulic pore size is based on the use of Laplace's law. The test sample in the form of a tablet is placed in the sleeve so that the rubber gasket is tightly compressed on the side

surface of the sample (**Figure 3**). At the bottom of the sleeve is a socket, connected to a hose of sufficient length, filled with a liquid which completely wets the sample. The lower end of the hose is placed in a vessel containing the same liquid. A slow rise of the sample is produced. At the moment of separation of the liquid in the hose from the sample, the height of the sample over the liquid level in the vessel h is recorded. The average hydraulic pore size d is calculated by the expression:

$$d = \frac{4\sigma}{\rho g h}, \tag{12}$$

where σ is the surface tension, ρ is the density of the liquid, and g is the acceleration of free fall.

In case of partial draining of the pore space (e.g., with intense evaporation of the liquid inside the PPMs, the action of the mass forces, etc.), the pore size distribution becomes significant. The question arises about the relationship between the function of pore distribution and average pore size of PPMs. Special experiments and subsequent calculations showed that for the PPMs, fabricated with the same technology from different fractions of one powder, such a relationship exists. If the integral function of pore distribution of PPMs with the average

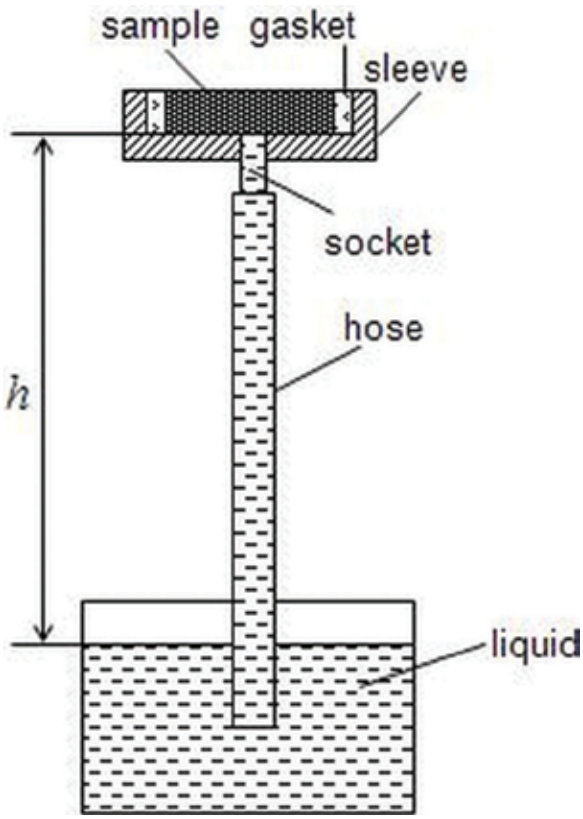

Figure 3. Experimental determination of the average hydraulic pore size.

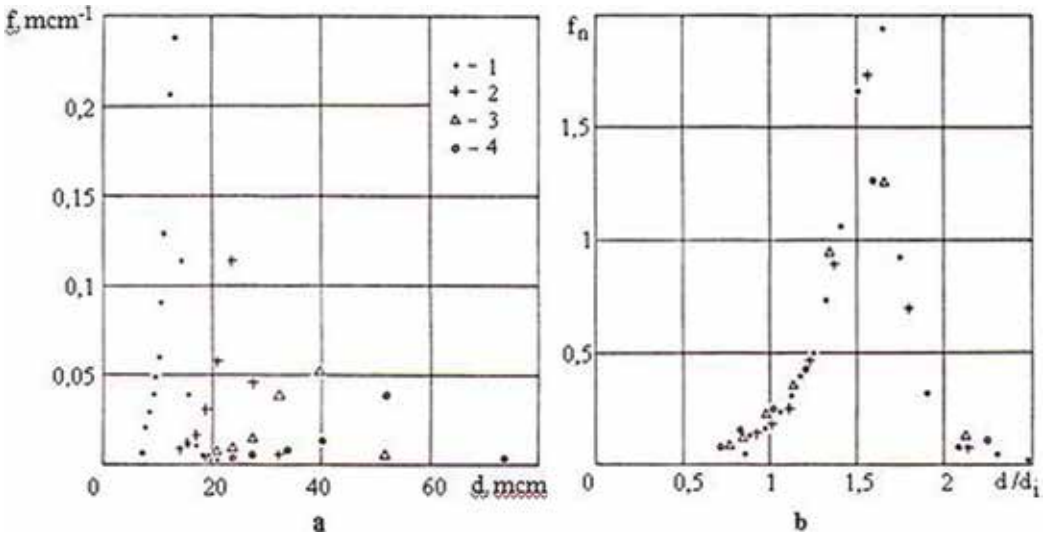

Figure 4. Experimental data on pore distribution of the porous bronze in conventional coordinates (a) and the normalized coordinates (b): 1, particle size <63 μm, d_1 = 8.1 μm; 2, 63–100 μm, d_2 = 15.2 μm; 3, 160–100 μm, d_3 = 24.2 μm; 4, 200–160 μm, d_4 = 33 μm.

hydraulic pore size of d_1 is $F_1(d)$, then the integral function of pore distribution of PPMs with the average hydraulic pore size of d_2 can be calculated from the function $F_1(d)$ by the coordinate transformation $d \rightarrow d' = d\ d_1/d_2$:

$$F_2(d) = F_1\left(d\frac{d_1}{d_2}\right); \tag{13}$$

respectively, for the differential pore distribution function:

$$f_2(d) = -\frac{dF_2(d)}{dd} = -\frac{dF_1(d')}{dd'}\frac{dd'}{dd} = f_1\left(d\frac{d_1}{d_2}\right)\frac{d_1}{d_2}. \tag{14}$$

Express provision is illustrated in **Figure 4**, where the experimental data for a porous bronze material BrOF10-1 depicts in the conventional coordinates (f, d) (a) and in the coordinates normalized by the average hydraulic pore size (f_n, $\frac{d}{d_i}$) (b). As shown, in the normalized coordinates the experimental points lie almost on the same curve.

3. Method to correct the data of mercury porosimetry

It is known [1] that pore distribution function, derived from the method of mercury porosimetry, is of a distorted character. It raises the volume of small pores that is caused by narrowing and widening porous channels on the way of mercury travel. Therefore, to use the data of mercury porosimetry in calculations of operational properties of porous materials, a correction of this data is necessary.

The developed method of correction of mercury porosimetry data is based on using a statistical model of a porous body of a serial type [3, 4]. In this model, a porous body is presented as a block of parallel capillaries, each of which consists of a number of successively disposed cylindrical elements. The diameter ζ and the length ξ of each element are random values, which do not depend on adjacent elements and are distributed with the probability density $\Psi(\zeta,\xi)$. Such a model is very similar to a real PPM structure and discloses the corrugateness of channels, as well as the accidental character of narrowing and widening.

Let us consider a process of mercury pressing into a model porous body. Let the mercury be on the left from the plane $x = 0$; on the right there is a porous body as a layer with the thickness l_0. If mercury pressure is p, it penetrates in the elements with the diameter, exceeding the critical one $\zeta_p = 4\gamma \cos\Theta/p$, where γ is a coefficient of the mercury surface tension and Θ is an angle of moistening with the mercury of the porous body material. Thereby, mercury will enter the ν first

$$z_\nu = \sum_{i=1}^{\nu} \xi_i. \tag{15}$$

elements, if $\zeta_1, \ldots, \zeta_\nu > \zeta_p$, and $\zeta_{\nu+1} < \zeta_p$. Then the length of the mercury part of the given capillary is

Let the function of the mercury capillary part length be $P(z)$. If suppressing in k-element, a corresponding distribution function is $P_k(z)$, and a probability density is $\Psi_k(z)$:

$$P_k(z) = \int_0^z \Psi_k(x)dx, \tag{16}$$

then

$$P(z) = \sum_{k=1}^{\infty} \omega_k P_k(z), \tag{17}$$

where ω_k is the probability of mercury suppression in the k-element, distributed as per a geometrical law:

$$\omega_k = \mu^{k-1}(1-\mu), \tag{18}$$

μ is the relative number of elements with the diameter exceeding a critical one.

$$\mu = \int_{\zeta_p}^{\infty} d\varsigma \int_0^{\infty} \Psi(\varsigma,\xi)d\xi. \tag{19}$$

Under pressure p all the ξ_i are distributed in the same may with the probability density:

$$\Phi_p(\xi) = \int_{d_p}^{\infty} \Psi(\varsigma,\xi)d\varsigma \Big/ \int_0^{\infty} d\xi \int_{d_p}^{\infty} \Psi(\varsigma,\xi)d\varsigma. \tag{20}$$

$\Psi_k(x)$ is calculated via $\Psi_{k-1}(x)$ as follows:

$$\Psi_k(x) = \int_0^x \Psi_{k-1}(x')\Phi_p(x-x')dx'. \tag{21}$$

Substituting Eq. (21) in Eq. (16), we shall get:

$$P_k(z) = \int_0^z \Phi_p(x)P_{k-1}(z-x)dx. \tag{22}$$

Next, substituting Eq. (22) in Eq. (17):

$$P(z) = (1-\mu)P_1(z) + \sum_{k=2}^{\infty} \mu^{k-1}(1-\mu)\int_0^z \Phi_p(x)P_{k-1}(z-x)dx = \int_0^z \Phi_p(x)\big(1-\mu+\mu P(z-x)\big)dx. \tag{23}$$

Thereby, we derived an equation to find a function of the length z distribution of the mercury capillary part under the pressure in the mercury p, which is an integral Volterra equation of the second gender:

$$P(z) = \int_0^z \Phi_p(x)\big(1-\mu+\mu P(z-x)\big)dx. \tag{24}$$

Thereafter we shall consider a model, in which all the elements have the same length ξ_0, that is, the density of the distribution probability ξ_i is equal to the δ-function under any pressure p:

$$\Phi_p(\xi) = \delta(\xi - \xi_0). \tag{25}$$

Justifying such a simplification is based on a smooth-changing a pore diameter. When the value of ξ_0 is rather small, a transversal size of the pore part, the length of which is ξ_0, may be considered as constant. Substituting Eq. (25) in (24), we derive an equation for $P(z)$:

$$p(z) = 1 - \mu + \mu p(z - \xi_0), \tag{26}$$

giving a step-by-step solution:

$$\begin{array}{lll} \text{when} & z<0 & P(z)=0; \\ \text{when} & 0\le z<\xi_0 & P(z)=1-\mu; \\ \cdots\cdots & \cdots\cdots & \cdots\cdots \\ \text{when} & (n\text{-}1)\xi_0\le z<n\xi_0 & P(z)=1-\mu^n. \end{array} \tag{27}$$

where $n = l_0/\xi_0$ is the number of elements in one capillary.

The derived solution for $P(z)$ must be connected with an experimental value of the entered mercury volume. If in the given capillary the length of the mercury part is z, the mercury volume in it is

$$v_{1p}(z) = v_1 z \int_{d_p}^{\infty} f(\varsigma) d\varsigma, \tag{28}$$

where $f(\zeta)$ is the true density of pore volume distribution on sizes and v_1 is a medium volume of capillary length unit. A total volume of mercury, entered under the pressure p, is

$$v(p) = \int_0^{l_0} N_0 \frac{dP}{dz} v_{1p}(z) dz + v_1 l_0 \int_{l_0} N_0 \frac{dP}{dz} dz \int_{\varsigma_p}^{\infty} f(\varsigma) d\varsigma, \tag{29}$$

where N_0 represents a total quantity of the capillaries. In the expression (29), the first component considers the volume of partially filled capillaries, and the second component considers the volume of fully filled ones. Convert the expression (29), considering $V_0 = v_1 N_0 l_0$ (V_0 is the total volume of the porous area):

$$v(p) = V_0 \left(1 - \frac{1}{l_0} \int_0^{l_0} P(z) dz\right) \int_{d_p}^{\infty} f(\varsigma) d\varsigma. \tag{30}$$

Using the solution (27), we may make a calculation:

$$\frac{1}{l_0} \int_0^{l_0} P(z) dz = 1 - \frac{\mu}{n} \frac{1 - \mu^n}{1 - \mu}. \tag{31}$$

Substituting Eq. (31) into Eq. (30):

$$v(p) = V_0 \frac{\mu}{n} \frac{1 - \mu^n}{1 - \mu} \int_{d_p}^{\infty} f(\varsigma) d\varsigma. \tag{32}$$

A dependence exists between the functions $\mu(\zeta)$ and $f(\zeta)$:

$$\frac{d\mu}{d\varsigma} = \frac{f(\varsigma)}{s\varsigma^2}, \tag{33}$$

where we use the designation, $s = \int_0^{\infty} \frac{f(\varsigma)}{\varsigma^2} d\varsigma$.

Using Eq. (33), let us convert an integral in Eq. (32) (later on for convenience of writing let us consider $v = v(d)$):

$$\int_{\varsigma}^{\infty} f(\varsigma)d\varsigma = -s\int_{\varsigma}^{\infty}\frac{d\mu}{d\varsigma}\varsigma^2 d\varsigma = s\left(\mu\varsigma^2 + 2\int_{\varsigma}^{\infty}\mu\varsigma d\varsigma\right), \tag{34}$$

Substituting Eq. (34) in Eq. (32), we get:

$$\frac{bv}{\mu}\frac{1-\mu}{1-\mu^n} - \mu\varsigma^2 = 2\int_{\varsigma}^{\infty}\mu\varsigma d\varsigma, \tag{35}$$

where there is marked $b=n/(sV_0)$. Differentiating the expression (35) on d, we get the following equation after converting:

$$\frac{d\mu}{d\varsigma} = \frac{b\frac{dv}{d\varsigma}\mu(1-\mu)(1-\mu^n)}{\mu^2\varsigma^2(1-\mu^n)^2 - bv\left((1-\mu)n\mu^n - 1 + \mu^n\right)}, \tag{36}$$

which forms the Cauchy problem together with a boundary condition

$$\mu(\varsigma_{\min}) = 1 \tag{37}$$

to determine a true function of pore quantity distribution on sizes $\mu(\zeta)$. In Eq. (21), the values b and n are indefinite and are connected with the desired function $\mu(\zeta)$. Therefore, to solve the Cauchy problem there is an iterative method as follows.

Zero approximation $\mu_0(\zeta)$ is obtained, considering:

$$f_0(\varsigma) = -\frac{1}{V_0}\frac{dv}{d\varsigma}; \quad s_0 = \int_0^{\infty}\frac{f_0(\varsigma)}{\varsigma^2}d\varsigma; \quad \xi_{00} = \int_0^{\infty}\varsigma f_0(\varsigma)d\varsigma; \quad n_0 = \frac{l_0}{\xi_{00}}; \quad b_0 = \frac{n_0}{s_0V_0}, \tag{38}$$

where l_0 is the size of the porous material sample being investigated in the direction of mercury travel. The following approximations $\mu_i(\zeta)$ are obtained using the following calculations:

$$f_i(\varsigma) = \frac{\frac{d\mu_{i-1}}{d\varsigma}}{2\int_0^{\infty}\mu_{i-1}\varsigma d\varsigma}; \quad s_i = \sqrt{s_{i-1}\frac{1}{2\int_0^{\infty}\mu_{i-1}\varsigma d\varsigma}}; \quad \xi_{0i} = \frac{3\int_0^{\infty}\mu_i\varsigma^2 d\varsigma}{2\int_0^{\infty}\mu_{i-1}\varsigma d\varsigma}; \quad n_i = \frac{l_0}{\xi_{0i}}; \quad b_i = \frac{n_i}{s_iV_0}. \tag{39}$$

Calculation of $\mu_i(\zeta)$ on each step of the iteration is made by the Runge-Kutta method [5]; therewith, the initial value of the calculated function is $\mu(\zeta_{min}) = 1$, and the derivative is calculated using the equality

$$\lim_{\mu\to 1}\frac{1-\mu}{1-\mu^n} = \frac{1}{n}, \tag{40}$$

with which it is possible to obtain:

$$\lim_{\mu \to 1} \frac{d\mu}{d\varsigma} = \frac{b\frac{dv}{d\varsigma}}{n\varsigma^2 - \frac{n-1}{2}bv}. \tag{41}$$

In **Figure 5** the results of calculating the functions of pore volume on size distribution from Eq. (36) and—for comparison—directly from the experimental data are given. It is seen that as a result of data correction of mercury porosimetry, the curves of pore distribution displace considerably in the direction of large pores.

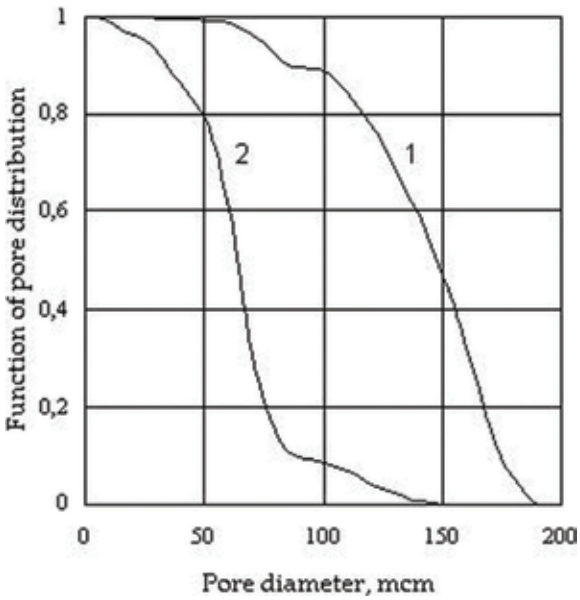

Figure 5. Function of pore volume distribution on sizes, calculated by the developed methodic (1) and directly from experimental data (2).

4. Conclusions

The relationship between the function of pore distribution and average hydraulic pore size, eliminating the need for a time-consuming set of experiments to determine the function of pore distribution of porous powder material, allowing to calculate the pore distribution function of porous powder material with any hydraulic average pore size from the known pore distribution function of the reference porous powder material with the fixed average hydraulic pore size, is explained.

The true function of pore distribution, obtained as a result of correcting mercury porosimetry data, enables to improve considerably the accuracy of calculations of processes and facilities parameters, where porous powder materials are used.

Author details

Victor Maziuk

Address all correspondence to: maziuk@tut.by

Powder Metallurgy Institute, Minsk, Belarus

References

[1] Greg S, Singh K. Adsorption, Surface Area, & Porosity. 2nd ed. London, New York: Academic Press; 1982. 306 p

[2] Hemming RW. Numerical Methods for Scientists and Engineers. 2nd ed. New York: McGraw-Hill; 1973. 400 p

[3] Chernenko AA, Chizmadzhev JuA. Subject to a theory of capillary balance in a porous body (in Russian). USSR Academy of Sciences Papers. 1963;**151**(2):392-395

[4] Markin VS. Subject to properties of interphase boundary in one model of a porous body (in Russian). USSR Academy of Sciences Transactions, OchN. 1963;**12**(9):1680-1692

[5] Butcher JC. Numerical Methods for Ordinary Differential Equations. New York: John Wiley & Sons; 2008. ISBN 978-0-470-72335-7

Section 2

Non-Metallic Powders

Chapter 5

Sol-Gel Synthesis of Calcium-Deficient Hydroxyapatite: Influence of the pH Behavior during Synthesis on the Structural, Chemical Composition and Physical Properties

José Bruno Rojas Trigos, Yolanda Jiménez-Flores, Víctor Suárez, Moseratt Suárez-Quezada and Uriel Nogal

Additional information is available at the end of the chapter

http://dx.doi.org/10.5772/intechopen.76531

Abstract

This work analyzes the influence of the pH on the physical-chemical properties of calcium-deficient hydroxyapatite synthesized by the sol-gel method. The pH evolution in the course of the synthesis was followed during the drop-by-drop adding of the calcium source to the phosphorus source, for different drip rates. The structural, morphological, and textural characterizations demonstrate that increasing the drip rate up to values of 10 $\mu l \cdot s^{-1}$ increases the crystallite size and the specific surface area, while the chemical and optical characterizations show that higher drip rates also increase the calcium and oxygen vacancies, related to an increase in the energy of the optical band gap. However, for the sample synthesized at a drip rate of 17 $\mu l \cdot s^{-1}$, the conjunction of higher calcium and oxygen vacancies has an opposite effect in the optical properties, in comparison to the observations in the synthesized samples at lower drip rates. Finally, the thermal characterization shows that, for all cases, the thermal diffusivity values agree with the reported values elsewhere.

Keywords: chemical composition, hydroxyapatite, optical properties, sol-gel method, thermal properties

1. Introduction

There are many chemical routes for the synthesis of hydroxyapatite and hydroxyapatite compounds, such as biomimetic methods, co-precipitation, and sol-gel methods, among others

[1–3]. It is well known that the characteristics of the synthesis methodology have great influence on the structure, morphology, and chemical composition, as well on the mechanical, thermal, and optical properties of the resultant product. Particularly in the sol-gel synthesis of hydroxyapatite (at normal temperature and pressure conditions), the evolution of the values of the pH during the synthesis strongly affects the final structure and stoichiometry, frequently by promoting the presence of calcium vacancies, crystalline defects, and impurities in the hydroxyapatite structure, modifying the physical-chemical properties of it. While for some applications (e.g., bone replacement and development of bioactive coatings), the presence of high levels of calcium and oxygen deficiencies are undesirable, for other applications such as development luminescent probes and photocatalysts, it are well received and even propitiated [4, 5]. In the year 2006, Degirmenbasi et al. [6] reported a simple sol–gel methodology to obtain stoichiometric hydroxyapatite, by adding drop-by-drop calcium nitrite aqueous solution to sodium phosphate aqueous solution, under mechanical stirring and adjusting the pH at 10, adding sodium hydroxide to the mixture, as needed. Modifying the Degirmenbasi methodology by using a specific amount of sodium hydroxide for the synthesis, Jiménez-Flores et al. [7] reported significant differences in the crystallite size and crystalline fraction, morphology, and thermal properties between samples of calcium-deficient hydroxyapatite, synthesized by using different drip rates and stirring methods (in this case, mechanical and ultrasonic-assisted). In the aforementioned work [7], the observed differences between the synthesized samples were related to an increase in the internal energy during the synthesis—due to the different drip rates and the stirring methods. However, it is also possible that the different drip rates have caused fluctuations in the pH values, affecting the kinetics and the efficiency of the chemical reaction. To clarify the effect of the drip rate in the synthesis of hydroxyapatite, we propose to monitor the evolution of pH during the sol–gel synthesis, comparing the structural, physical, and chemical characteristics of the samples synthesized under different drip rates.

2. Synthesis of calcium-deficient hydroxyapatite

For the sol-gel synthesis of calcium-deficient hydroxyapatite (CDHA), 80 ml of tetra hydrated calcium nitrate ($Ca(NO_3)_2{\cdot}4H_2O$), 48 ml of sodium phosphate (Na_3PO_4), and 16 ml of sodium hydroxide (NaOH) aqueous solutions, at 0.1 M, were prepared at room temperature (25°C). All the chemical compounds were purchased from Sigma-Aldrich.

2.1. Synthesis procedure

The NaOH aqueous solution was incorporated to the $Ca(NO_3)_2{\cdot}4H_2O$ solution and stirred during 30 min to obtain a heterogeneous mixture, as the calcium source. This mixture was then added, drop-by-drop, to the aqueous solution of Na_3PO_4 under continuous stirring at 25°C. During this first stage of the synthesis (**Figure 1**, framed inset), the condensation and gelation of the sol particles take place. To eliminate the solvent (DI water, in this case), the obtained gel is filtered and dried, resulting into a xerogel with the appearance of small brittle glasses. Finally, such glasses were mechanically pulverized obtaining powdered samples of the synthesized compounds. In **Figure 1**, a schematic draw of the CDHA synthesis is shown.

For the purposes of the present work, four different drip rates were used for the CDHA synthesis (see **Table 1**), considering that 20 drops are equivalent to 1 ml.

For each sample, the evolution of the pH during the first stage of the synthesis was followed, making a comparison between the samples during the incorporation of the first 63 ml of the calcium source into the Na_3PO_4 solution. The results are presented in **Figure 2**.

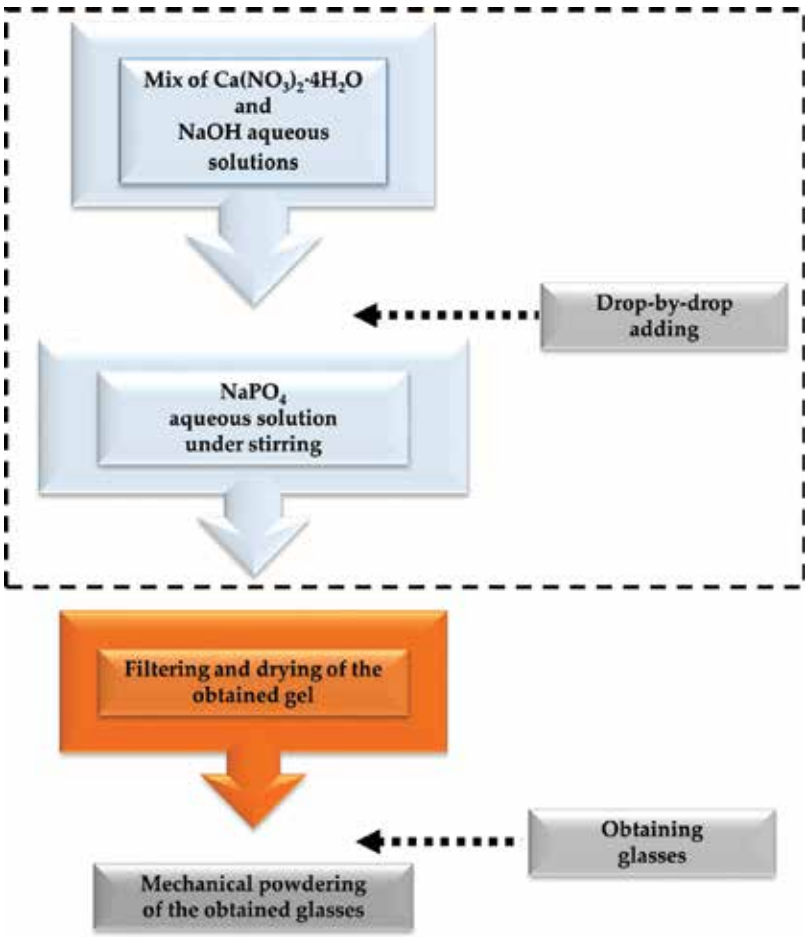

Figure 1. Schematic draw of the sol–gel CDHA synthesis.

Sample	Stirring velocity (rpm)	Drip rate ($\mu l \cdot s^{-1}$)	Drying conditions
CDHA_A	600	≈5	24 h at 80°C
CDHA_B		≈8	
CDHA_C		≈10	
CDHA_D		≈17	

Table 1. Parameters employed for the CDHA synthesis.

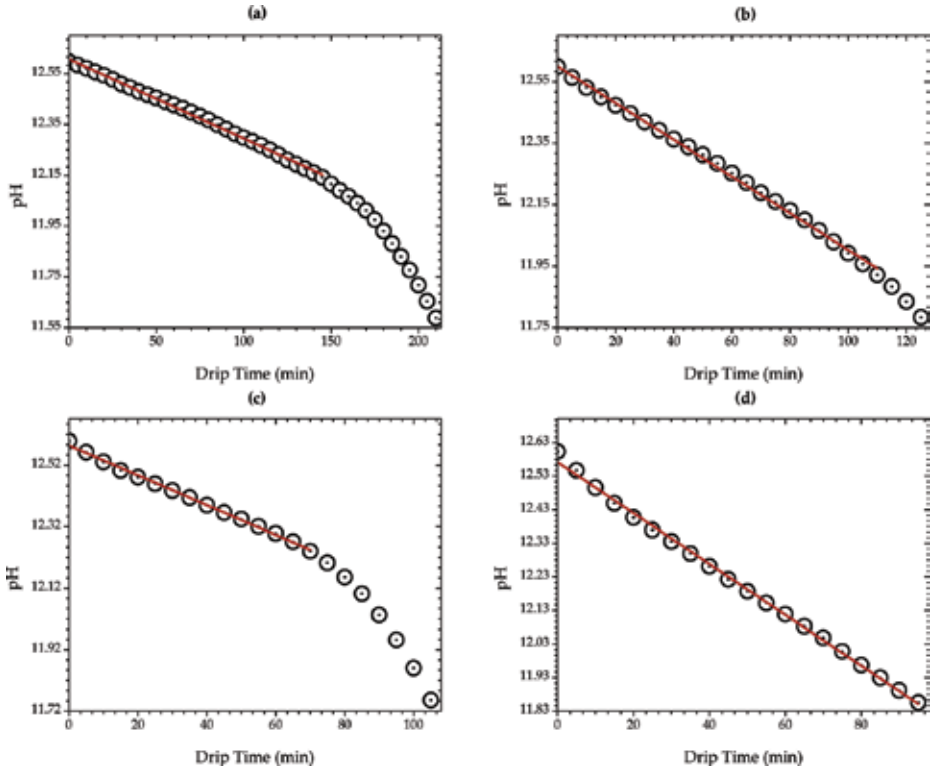

Figure 2. Evolution of the pH during the synthesis of the (a) CDHA_A, (b) CDHA_B, (c) CDHA_C, and CDHA_D samples. The red line represents the best linear fit.

In all cases, the pH values decrease monotonically in time as it was expected; however, the samples exhibit different distinctive features. The shape of drip time vs. pH plots of CDHA_A and CDHA_C samples is quite similar, showing a linear region at the drip beginning (**Figure 2 (a)** and **(c)**), where the pH decreases at rates of 52.2×10^{-6} and 80.8×10^{-6} s^{-1}, respectively. After the linear region, the pH values fall down rapidly changing its concavity, approximately at 2/3 of the drip time for both samples.

On the other hand, the pH values during the synthesis of the CDHA_B sample show a larger linear region than the CDHA_A and CDHA_C samples (**Figure 2(b)**), with a slope of 116.2×10^{-6} s^{-1}; nevertheless, a small concavity change occurs just at the end of the drip time. Contrary to the previous samples, the drip time vs. pH plot of CDHA_D sample (**Figure 2(d)**) shows that the pH values decrease at a constant rate of 126.3×10^{-6} s^{-1}. Finally, it is not worthless to mention that the final pH values (i.e., at the very end of the synthesis of each sample) were 10.04, 11.6, 11.7, and 11.86 for CDHA_A, CDHA_B, CDHA_C, and CDHA_D samples, respectively. This is an important issue to remark, since other authors report that the best conditions for the sol-gel synthesis of stoichiometric hydroxyapatite consider a pH = 10 [6, 8].

http://dx.doi.org/10.5772/intechopen.76531

3. Structure analysis

3.1. Crystalline structure and surface morphology

By using an X-ray diffractometer (Bruker, D-8 Advance), which employs the Cu-K line (λ = 1.5418 Å) and for diffraction angle ranging $10° \leq \Theta \leq 80°$, the X-ray diffraction pattern was obtained for all samples. The standard corundum powder pattern was used to determine the instrumental width, $\beta_{inst} = 0.047°$. In **Figure 3**, the diffraction patterns are displayed identifying the peaks corresponding to the diffraction planes (100), (200), (002), (210), (320), and (004).

The X-ray diffraction patterns agree well (with figure of merit up to 0.9, in all cases) with the ICDD crystallographic chart no. 00–009-0432 (from the International Centre for Diffraction Data database), corresponding to the synthetic hydroxyapatite—with chemical formula, $Ca_5(PO_4)_3(OH)$. For the analysis of the diffraction patterns, the principal observed diffraction peaks were considered to calculate the average crystallite size D, by means of the Scherrer equation (Eq. (1)), while the Bragg Law (Eq. (2)) was used for the determination of the unitary cell parameters $\{c, a\}$. In such calculations, the corrected peak width $\beta_c = (\beta^2 - \beta_{inst}^2)^{1/2}$ has been used:

$$D = \frac{0.9\lambda}{\beta_c Cos\Theta} \tag{1}$$

$$\frac{4\,Sin^2\Theta}{\lambda^2} = \frac{4}{3}\left[\frac{h^2 + hk + k^2}{a^2}\right] + \left[\frac{l}{c}\right]^2 \tag{2}$$

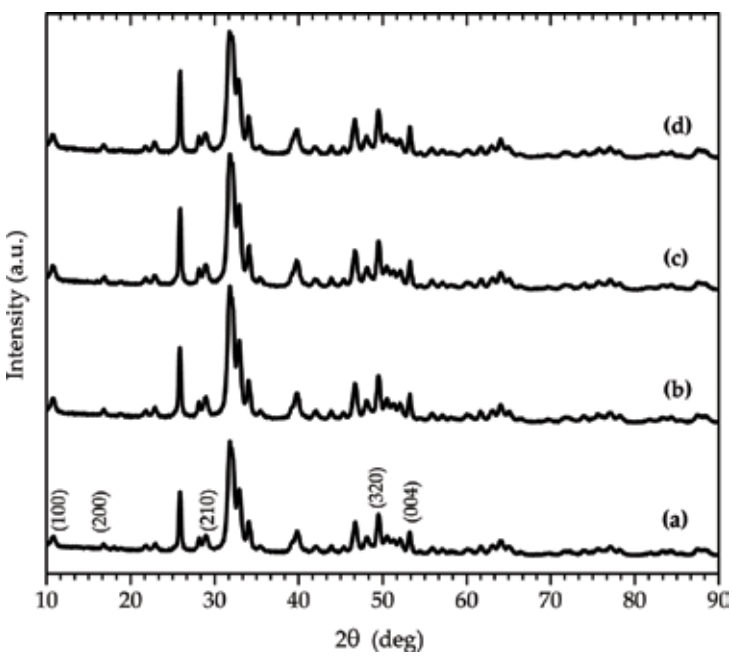

Figure 3. X-ray diffraction patterns of (a) CDHA_A, (b) CDHA_B, (c) CDHA_C, and (d) CDHA_D samples.

In Eq. (2), a hexagonal 6/m-dipyramidal crystal symmetry was considered: being *h*, *k*, and *l* the Miller indexes of the diffraction plane (*h*, *k*, *l*). The results of the analysis has been summarized in **Table 2**, including a comparison with the reported values of unitary cell parameters for stoichiometric hydroxyapatite (c = 6.8745 Å, a = 9.4166 Å) [9].

Although no significant differences were found in the values of the parameters of the unitary cell, a monotonic increase in the crystallite size is observed, as function of the drip rate. The surface morphology of the samples was studied through their corresponding micrographs, taken by a scanning electron microscope, SEM (JEOL, JSM-6390LV), employing an accelerating voltage of 20 kV and a magnification of 20,000× (see **Figure 4**).

Sample	D (Å)	a (Å)	Δa (%)	c (Å)	Δc (%)
CDHA_A	268.3	9.412	0.04	6.877	−0.04
CDHA_B	271.7	9.418	−0.01	6.877	−0.04
CDHA_C	275.3	9.416	0.01	6.875	−0.01
CDHA_D	303.3	9.419	−0.03	6.873	0.02

Table 2. Average crystallite size and unitary cell parameters.

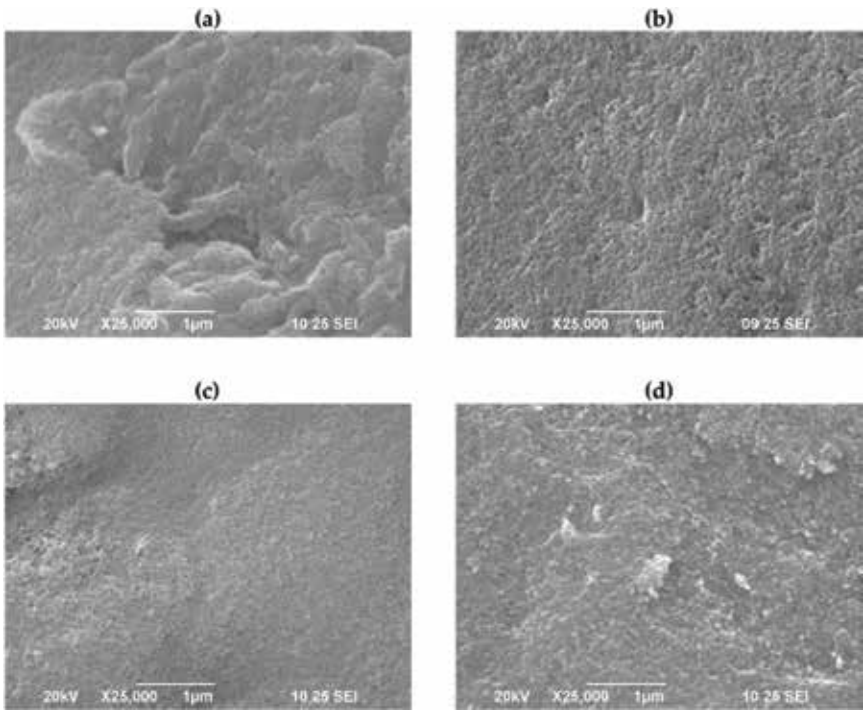

Figure 4. SEM micrographs of samples: (a) CDHA_A, (b) CDHA_B, (c) CDHA_C, and (d) CDHA_D.

http://dx.doi.org/10.5772/intechopen.76531

The SEM images show that increasing the drip rate has a discernible effect on the surface morphology of the glasses, previously to the mechanical powdering of them. The sample CDHA_A shows the most irregular surface of all (**Figure 4(a)**), small pores being discernible on it, while the sample CDHA_B presents a much more planar surface (**Figure 4(b)**) with (in appearance) larger pores on it. On the other hand, sample CDHA_C shows a less planar but smoother surface (**Figure 4(c)**) and, at least in appearance, a homogenous distribution of small pores on the surface. The case of CDHA_D presents a compact and granulated surface (**Figure 4(d)**), but still small pores are perceived.

3.2. Textural properties

In order to determine the textural properties of the synthesized samples, the adsorption isotherms for 100 mg of powdered samples were obtained (see **Figure 5**) employing a Quantachrome NOVA4200e equipment, using N_2 as adsorbate. The measurement temperature was kept at −196°C, using liquid nitrogen as coolant.

From the adsorption isotherms, the specific surface area was determined by the Brunauer-Emmet-Teller (BET) method, while the Barrett-Joyner-Halenda (BJH) method was for the determination of the pore size diameter [10, 11]. The textural properties of the samples have

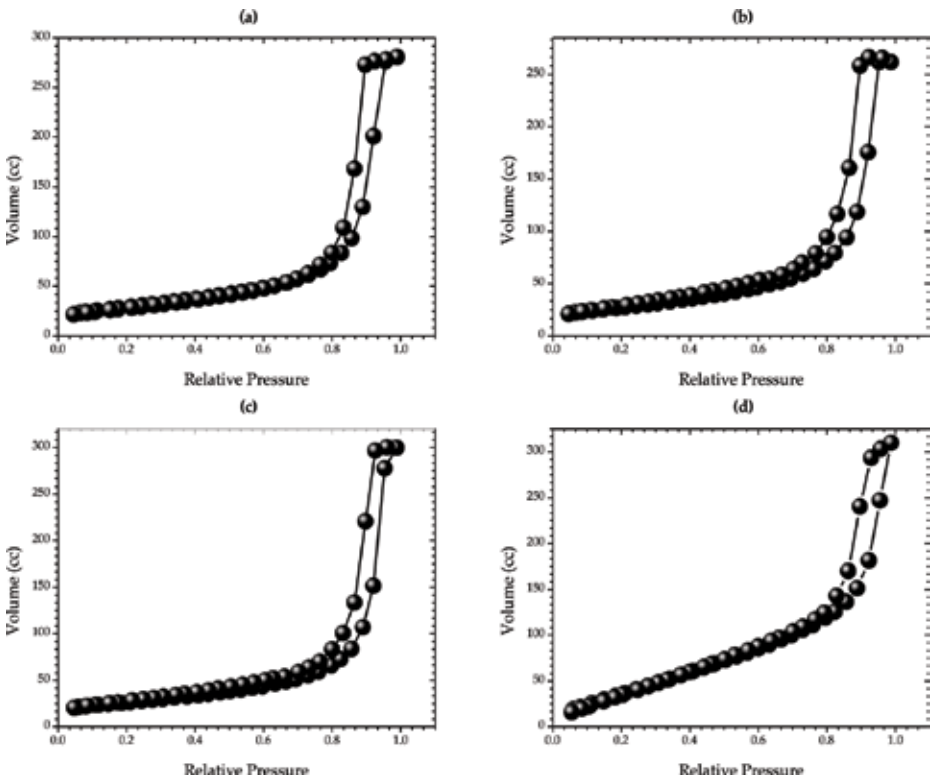

Figure 5. Adsorption isotherms of (a) CDHA_A, (b) CDHA_B, (c) CDHA_C, and (d) CDHA_D samples.

Sample	Specific surface area ($m^2 \cdot g^{-1}$)	Pore size diameter (Å)	Total pore volume ($cm^3 \cdot g^{-1}$)
CDHA_A	101.860	203.2	0.434
CDHA_B	91.856	212.9	0.464
CDHA_C	96.178	181.9	0.405
CDHA_D	92.403	117.2	0.391

Table 3. Textural properties of the studied samples.

been summarized in **Table 3**. From their shape, the isotherms shown in **Figure 5** can be classified as type V isotherm, which indicates unrestricted multilayer adsorption, characteristic of mesoporous materials. The shape of the hysteresis loops is indicative of ink-bottle-shaped pores, associated to poor network connectivity effects [12].

The textural properties agrees well with the SEM observations, correcting the initial visual impression on the pore size on the surface of the samples. With the exception of the CDHA_A sample, the pore radius size, as well as the total pore volume, decreases with increasing drip rate.

4. Chemical characterization

4.1. Elemental chemical composition

The elemental chemical composition was determined using an energy-dispersive X-ray spectroscopy (EDS) system, integrated to the SEM equipment, which employs a Si-Li detector (Oxford Pentafet, mod. 7582). From the EDS spectra recorded for energies ranging 0.12–12 keV, the elemental quantification, as well as the Ca/P and the (Ca + O)/P ratios, has been determined and summarized in **Table 4**.

The results of the elemental quantification by EDS, together with the pH behavior during the synthesis, are indicative that the mass flow (controlled through the drip rate) significantly affects the reaction kinetics during the formation of hydroxyapatite, influencing the efficiency of ion exchange, promoting calcium and oxygen vacancies. The values of carbon content in the samples are consistent with the observed surface morphology and textural properties at different drip rates, suggesting the hypothesis that the presence of carbon in the samples could be due to the absorption of atmospheric CO_2.

Sample	Na (at.%)	C (at.%)	O (at.%)	P (at.%)	Ca (at.%)	Ca/P	(Ca + O)/P
CDHA_A	—	9.78	54.58	13.87	21.77	1.57	5.50
CDHA_B	—	7.40	56.91	14.56	21.13	1.45	5.36
CDHA_C	—	6.53	57.69	14.79	20.99	1.42	5.32
CDHA_D	0.21	8.59	57.32	14.42	19.46	1.35	5.32

Table 4. Quantification of the elemental chemical composition of the samples.

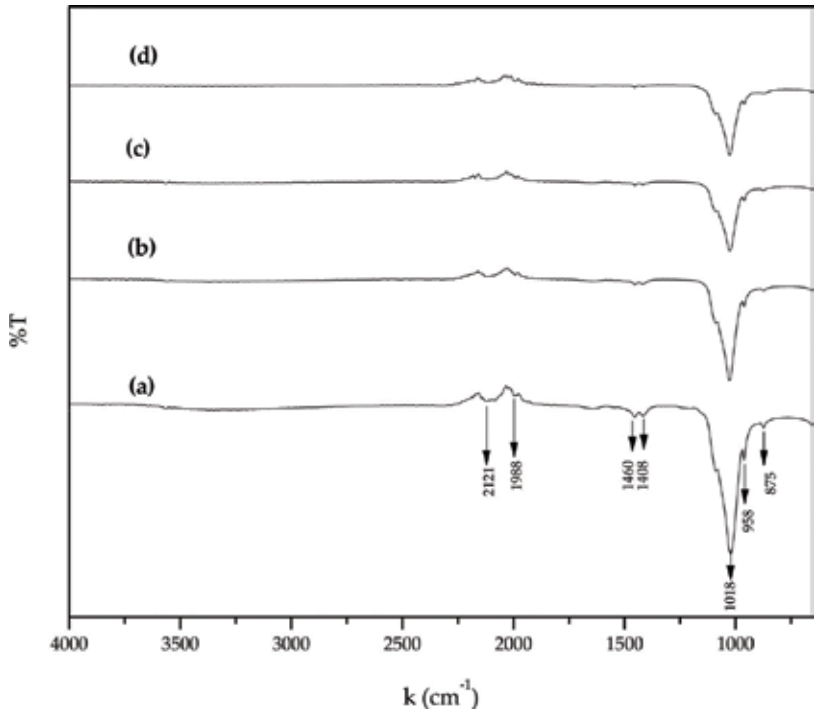

Figure 6. FTIR spectra of samples: (a) CDHA_A, (b) CDHA_B, (c) CDHA_C, and (d) CDHA_D.

4.2. Functional groups detected

For the identification of the functional groups present in samples, the diffuse reflectance spectra were obtained using a FTIR spectrophotometer (Shimadzu, IR Affinity-1S), operating in the attenuated total reflection mode, and the spectroscopic wave number ranging 4000 $cm^{-1} \leq k \leq 650\ cm^{-1}$. At next (**Figure 6**), the FTIR spectra are displayed identifying the detected signals.

The signals centered at 958 and 1018 cm^{-1} are typical of asymmetric stretching of P—O bond of the PO_4^{-3} functional group, while the signal at 875 cm^{-1} corresponds also to the P—O asymmetric stretch but for the HPO_4^{-2} functional group. The signals in the neighborhood of 1408 and 1460 cm^{-1} correspond to stretching of the C—O bond, proper of the inorganic carbonate group. Finally, the signals at 2121 and 1988 cm^{-1} are related to the symmetrical stretching of the H—P bond in the HPO_4^{-2} functional group. These results agree with the EDS elemental quantification and the X-ray diffraction patterns, confirming the formation of calcium-deficient hydroxyapatite. In addition, the presence of carbonate signals supports the hypothesis that the carbon content is due to the atmospheric CO_2 absorbed during the synthesis.

5. Optical properties

To investigate on the optical properties of the CDHA samples (particularly the optical band gap), two experimental techniques were employed here: the UV–Vis spectroscopy and the

photoacoustic spectroscopy (PAS) techniques. The UV–Vis technique provides the diffuse reflectance, characterized by the Kubelka-Munk function F(R), as function of the wavelength (equivalent to the photon energy) of the excitation beam. Since the F(R) function depends linearly on the ratio between the optical absorption and the scattering coefficients, an empirical estimation of the band gap, E_g, is possible by extrapolation of the linear region of the Tauc plots [13]. However, the UV–Vis technique is quite sensitive to light scattering effects, so, an over estimation of E_g value is frequent. On the other hand, the PAS technique directly provides the optical absorption spectra, being less disturbed by light scattering effects than other optical spectroscopic techniques, because the PAS signal is generated only by the internal heat diffusion in the sample, as result by the optical absorption and the non-radiative thermal relaxation mechanisms [14, 15].

5.1. UV–Vis diffuse reflectance spectra

A UV–Vis spectrophotometer (Agilent, mod. Cary-100) was employed to measure the F(R) spectrum of the synthesized samples, ranging the wavelength from 200 nm ≤ λ ≤ 250 nm, correcting the obtained spectrums by measuring the background signal. In **Figure 7**, the Tauc plots, from the F(R) values, are exhibited considering the samples as indirect band gap materials.

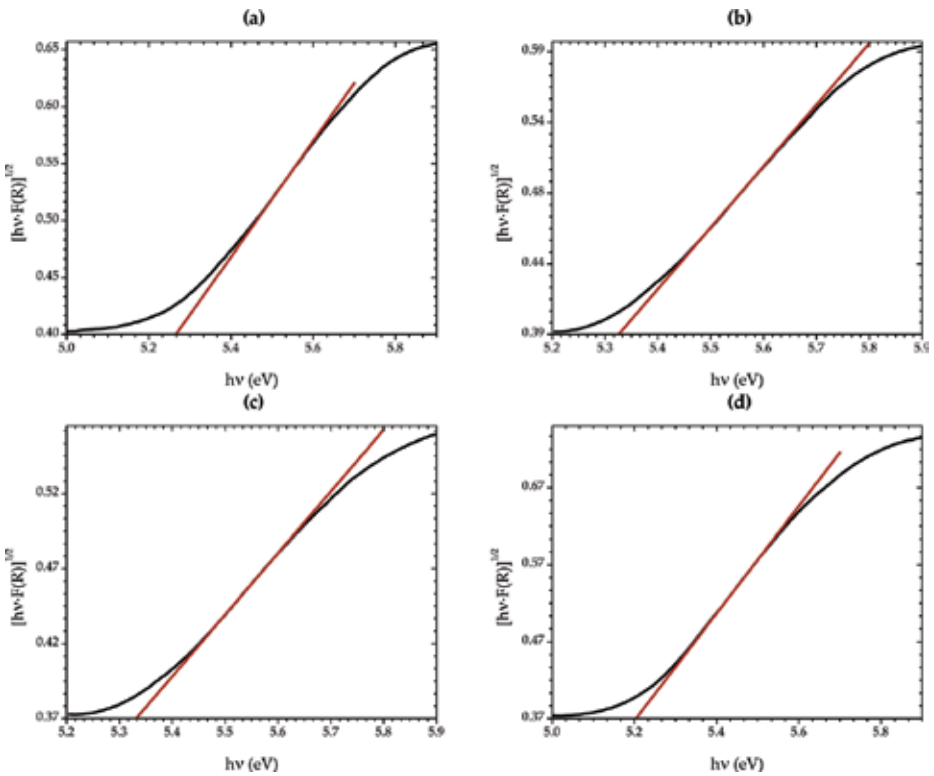

Figure 7. Tauc plots of (a) CDHA_A, (b) CDHA_B, (c) CDHA_C, and (d) CDHA_D samples. The red line shows the extrapolation of the linear region.

5.2. PAS absorption spectra

To record the absorption spectra of the samples, a homemade PAS measurement system was used for such goal, for a wavelength ranging 206 nm ≤ λ ≤ 288 nm and for a modulation frequency f = 17 Hz. A schematic drawing of the experimental setup is presented as follows (**Figure 8**).

The continuous beam, emitted by the 200 W Hg Arc lamp (Newport, Mod. 66,483) optimized for UV, passes through a monochromator (Newport, mod. Cornerstone 130 1/8 m) to obtain a quasi-monochromatic excitation beam. The continuous excitation beam was then modulated by a mechanical chopper (Stanford Research Systems, mod. SR-540), impinging into the optical window of the PAS measurement cell (MTEC, mod. 300). The PAS signal (**S**, $\Delta\phi$) was then filtered and amplified by a lock-in amplifier (Stanford Research Systems, mod. SR 830), using the modulation frequency as reference, to be storage for its further analysis. From the absorption spectra, the Tauc plots of the samples were constructed for the empirical determination of the optical band gap energies (**Figure 9**).

The optical band gap calculations, from UV–Vis and PAS measurements, are reported in **Table 5**, for purposes of comparison between techniques.

As can be seen from the above results, as the drip rate gets higher, the energy band gap also increases, with the one exception of the CDHA_D, and as it was expected, there is an overestimation on the optical band gap calculations from UV–Vis data. Nevertheless, in both cases (and for all samples) the empirical determination of E_g agrees with the reported values for hydroxyapatite from UV–Vis measurements and density functional theory (DFT) calculations [16, 17]. Using atomistic calculations, Santos and Rezende [18] conclude that the formation of the most probable defects in hydroxyapatite always involves calcium and oxygen vacancies, in agreement to the DFT calculations reported by de Leeuw et al. [19] and de Leeuw [20]. Based on the previous works in the EDS quantification, the increasing of the E_g is

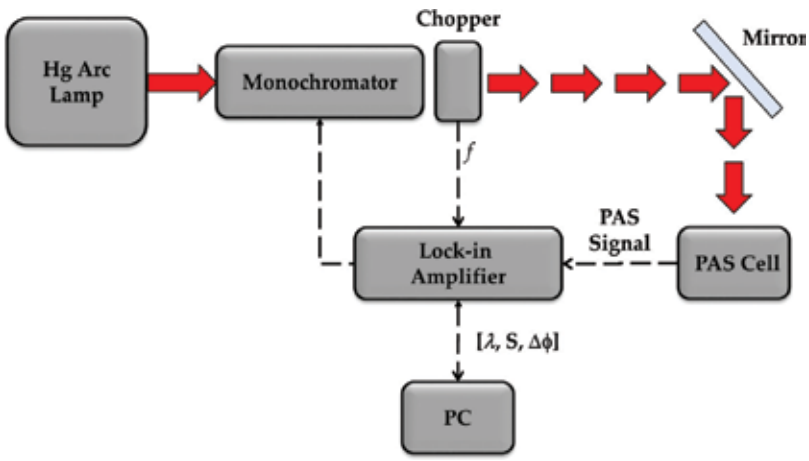

Figure 8. PAS measurement system. Here, **S** and $\Delta\phi$ are the amplitude and the phase shift of the PAS signal, respectively.

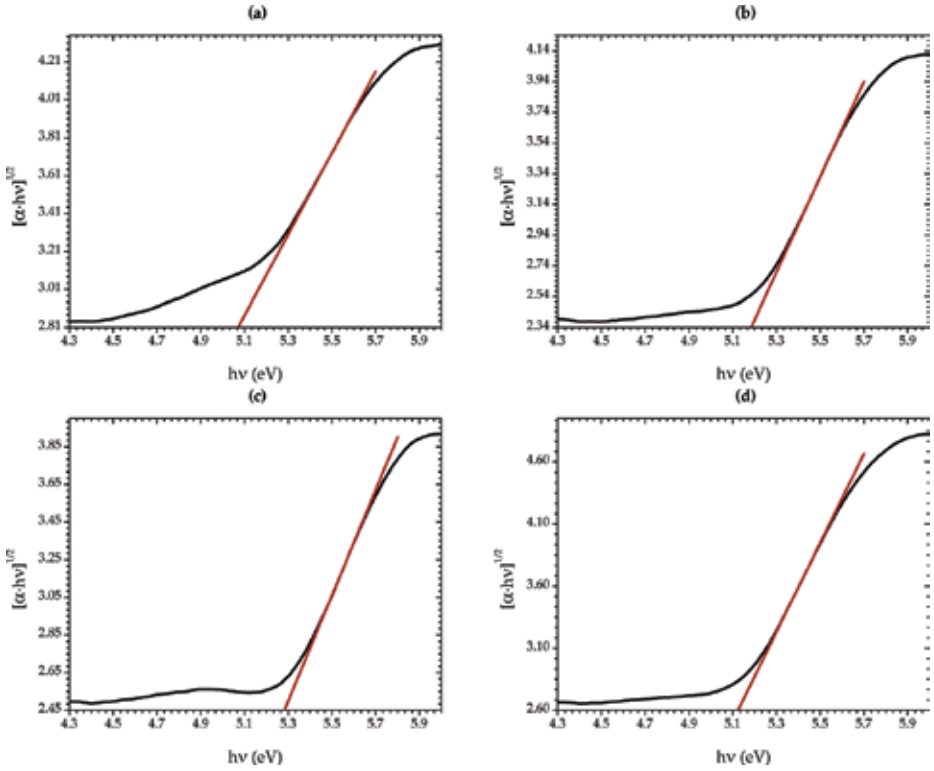

Figure 9. Tauc plots of (a) CDHA_A, (b) CDHA_B, (c) CDHA_C, and (d) CDHA_D samples. The red line shows the extrapolation of the linear region.

Sample	E_g[a] (eV)	E_g[b] (eV)	ΔE_g (%)
CDHA_A	5.26	5.1	3.14
CDHA_B	5.31	5.18	2.51
CDHA_C	5.33	5.29	0.76
CDHA_D	5.21	5.12	1.76

[a]From UV-Vis.
[b]From PAS.

Table 5. Optical band gap values determined from UV–Vis and PAS measurements.

explained as an effect mostly due to a higher levels of calcium and oxygen (in the OH sites) vacancies, as the drip rate increases from 5 to 10 $\mu l \cdot s^{-1}$. For a higher drip rate (i.e., 17 $\mu l \cdot s^{-1}$), it is possible that the oxygen vacancies occur at the phosphate sites as well at the OH sites. In such case, the DFT calculations predict the existence of energy levels inside the forbidden band, which explains why the band gap energy decreases for the CDHA_D sample.

http://dx.doi.org/10.5772/intechopen.76531

6. Thermal properties

For the determination of the thermal response of the samples, a homemade photoacoustic detection (PA) measurement system was employed, for a modulation frequency ranging 400 Hz ≤ f ≤ 4 kHz. The experimental setup is similar to the PAS measurement system but replacing the Hg arc lamp and the monochromator by a 405 nm laser diode (controlled by a TTL signal), as is shown in **Figure 10**.

The excitation beam wavelength was chosen to avoid the contribution of the photogenerated charge carriers to the PA signal. To perform the PA measurements in the transmission configuration [21, 22], pills of powdered samples were obtained by compacting 100 mg of powdered sample. Considering the samples as optically opaque and thermally thick, the PA signal will depend on the modulation frequency as indicated by Eq. (3):

$$S = A_0 \cdot \frac{\exp\left(-\sqrt{f/f_c}\right)}{f}; \qquad f_c \equiv \frac{\alpha_s}{\pi \cdot l_s^2} \tag{3}$$

In Eq. (3), A_0 is an instrumental constant, f_c is the so-called characteristic frequency of the sample, and α_s and l_s are the thermal diffusivity and thickness of the sample, respectively. For modulation frequencies where Eq. (3) is applicable, α_s can be calculated from the slope of the linear region in the semi-logarithmic $f^{1/2}$ vs. f·**S** plot (**Figure 11**). The results obtained have been summarized in **Table 6**.

Although the values of the thermal diffusivities agree with the reported values for hydroxyapatite [7, 23, 24], there is no clear correlation with the synthesis drip rate nor the stoichiometry of the samples. This is because the different levels of compaction of the sample's pills affect the effective thermal properties. The nonlinear behavior at low modulation frequencies is

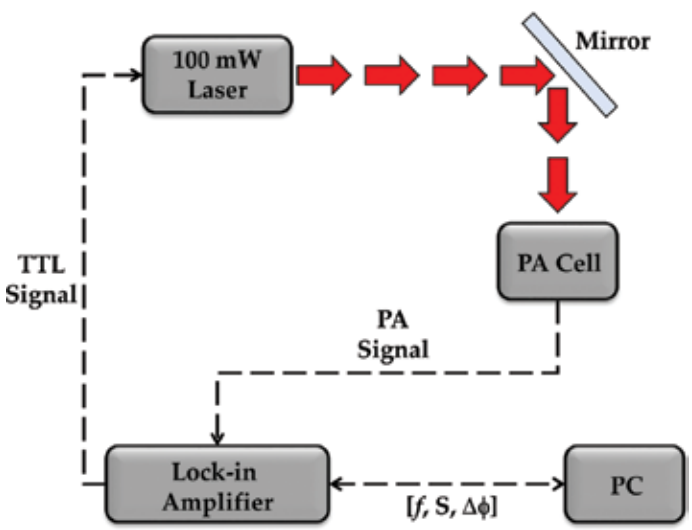

Figure 10. PA measurement system. Here, **S** and Δϕ are the amplitude and the phase shift of the PA signal, respectively.

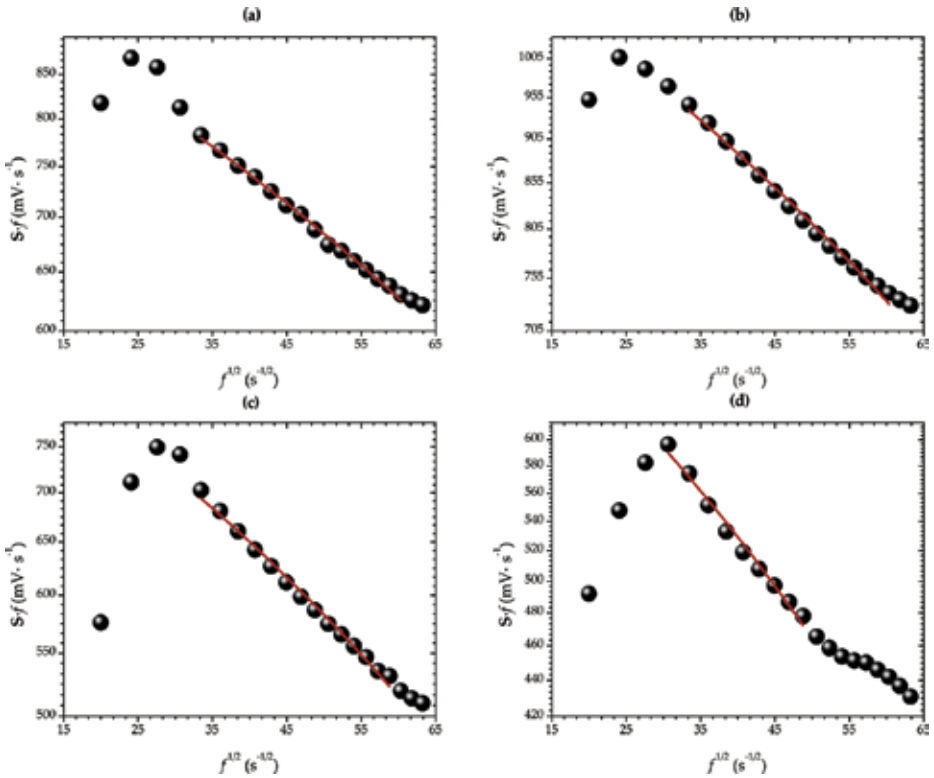

Figure 11. $f^{1/2}$ vs. fS plot of (a) CDHA_A, (b) CDHA_B, (c) CDHA_C, and (d) CDHA_D. The red line shows the best fit.

Sample	Slope (mV·s$^{-1/2}$)	f_c ($\times 10^{-3}$ Hz)	α_s ($\times 10^{-7}$ m^2·s^{-1})
CDHA_A	−5.75	30.29	1.90
CDHA_B	−7.78	16.53	1.02
CDHA_C	−6.75	21.93	2.42
CDHA_D	−6.49	23.73	2.58

Table 6. Thermal diffusivity of the samples.

indicative of a transition between thermal regimes. For larger modulations frequencies, the signal-to-noise ratio becomes too small (especially for CDHA_D sample) to obtain reliable data. The previous results must be corroborated by other photothermal techniques, such as IR photothermal radiometry or lock-in thermography [25, 26].

7. Conclusions

The sol–gel synthesis of calcium-deficient hydroxyapatite was successfully achieved, for four different drip rates during synthesis procedures, describing the distinctive features of the pH evolution, for each case. For the samples synthesized at drip rate values of 5, 8, 10, and

17 $\mu l \cdot s^{-1}$, the structural, morphological, and textural characterizations show that the pore radius size and the total pore volume tend to decrease for a drip rate up to 5 $\mu l \cdot s^{-1}$, contrary to the crystallite size, which decreases for all samples as the drip rate increases. The chemical characterizations demonstrate that increasing the drip rate promotes the presence of calcium and oxygen vacancies in the hydroxyapatite structure. From the diffuse reflectance and absorbance spectra, the energy band gap of the samples increases as the drip rate does, with the exception of the sample synthesized at 17 $\mu l \cdot s^{-1}$, possible due to a combination of a larger presence of oxygen vacancies on the phosphate sites and calcium vacancies. The results of the thermal characterization allowed determining the effective thermal diffusivity of the samples, obtaining values that agree well with those reported in the literature. However, it was not possible to establish a clear correlation between the effective thermal properties and the values of the drip rate used during the synthesis. Finally, the drip rate in the hydroxyapatite sol-gel synthesis clearly governs the pH during synthesis and, therefore, has a major impact in the physical-chemical properties of the hydroxyapatite.

Acknowledgements

Authors acknowledge the Instituto Politécnico Nacional from Mexico, for financial support through 1855 SIP multidisciplinary and 20170229 SIP projects. The authors wish to thank the National Energy Conversion and Storage Laboratory, CICATA U. Legaria of the Instituto Politécnico Nacional of Mexico, and the PhD student René Cabrera for helping with the acquisition and analysis of XRD data. The authors thank also the PhD student Guadalupe Romero Ortiz for helping in the acquisition of hydrogen adsorption data.

Conflict of interest

The authors of this work declare no conflicts of interest of any kind.

Author details

José Bruno Rojas Trigos[1]*, Yolanda Jiménez-Flores[1], Víctor Suárez[2], Moseratt Suárez-Quezada[1] and Uriel Nogal[3]

*Address all correspondence to: jrojast@ipn.mx

1 Instituto Politécnico Nacional, Centro de Investigación en Ciencia Aplicada y Tecnología Avanzada, Unidad Legaria, Ciudad de México, Mexico

2 Cátedras CONACYT, Departamento de Química, ECOCATAL, Universidad Autónoma Metropolitana-Iztapalapa, Ciudad de México, Mexico

3 Cátedras CONACYT, Instituto Politécnico Nacional, Centro de Investigación en Ciencia Aplicada y Tecnología Avanzada, Ciudad de México, Mexico

References

[1] Supová M. Substituted hydroxyapatites for biomedical applications: A review. Ceramics International. 2015;**41**:9203-9231. DOI: 10.1002/jbm.b.33651

[2] Ferraz MP, Monteiro FJ, Manuel CM. Hydroxyapatite nanoparticles: A review of preparation methodologies. Journal of Applied Biomaterials and Biomechanics. 2004;**2**:74–80. ISSN: 1722-6899

[3] Nasser Mostafa Y. Characterization, thermal stability and sintering of hydroxyapatite powders prepared by different routes. Materials Chemistry and Physics. 2005;**94**:333-341. DOI: 10.1016/j.matchemphys.2005.05.011

[4] Deshmukh K, Shaik MM, Ramanan SR, Kowshik M. Self-activated fluorescent hydroxyapatite nanoparticles: A promising agent for bioimaging and biolabeling. ACS Biomaterials Science & Engineering. 2016;**2**:1257-1264. DOI: 10.1021/acsbiomaterials.6b00169

[5] Rosenmana G, Aronova D, Oster L, Haddad J, Mezinskis G, Pavlovska I, Chaikina M, Karlov A. Photoluminescence and surface photovoltage spectroscopy studies of hydroxyapatite nano-bio-ceramics. Journal of Luminescence. 2007;**122-123**:936-938. DOI: 10.1016/j.jlumin.2006.01.331

[6] Degirmenbasi N, Kalyon DM, Birinci E. Biocomposites of nanohydroxyapatite with collagen and poly(vinyl alcohol). Colloids and Surfaces B: Biointerfaces. 2008;**48**:42-49. DOI: 10.1016/j.colsurfb.2006.01.002

[7] Jiménez-Flores Y, Camacho N, Rojas-Trigos JB, Suárez M. Synthesis and thermal characterization of hydroxyapatite powders obtained by sol-gel technique. In: Campos RP, Cuevas AC, Esparza Muñoz RA, editors. Characterization of Metals and Alloys. Switzerland: Springer International Publishing; 2017. pp. 167-180. DOI: 10.10071978-3-319-31694-9_14

[8] Mollazadeh S, Javadpour J, Khavandi A. In situ synthesis and characterization of nanosize hydroxyapatite in poly(vinyl alcohol) matrix. Ceramics International. 2007;**33**:1579-1583. DOI: 10.1016/j.ceramint.2006.06.006

[9] Bideaux RA, Bladh KW, Nichols MC. In: Anthony JW, editor. Handbook of Mineralogy: Arsenates, Phosphates, Vanadates. Vol. 4. Chantilly, VA, USA: Mineralogical Society of America; 2000

[10] Brunauer S, Emmett PH, Teller E. Adsorption of gases in multimolecular layers. Journal of the American Chemical Society. 1938;**60**(2):309-319. DOI: 10.1021/ja01269a023

[11] Barret PB, Joyner LG, Halenda PP. The determination of pore volume and area distributions in porous substances. I. Computations from nitrogen isotherms. Journal of the American Chemical Society. 1951;**73**(1):373-380. DOI: 10.1021/ja01145a126

[12] Sing KSW, Everett DH, Haul RAW, Moscou L, Pierotti RA, Rouquérol RJ, Siemieniewska T. Reporting physisorption data for gas/solid systems with special reference to the

determination of surface area and porosity. Pure and Applied Chemistry. 1985;**57**(4):603-619. DOI: 10.1351/pac198557040603

[13] Tauc J. Optical properties and electronic structure of amorphous Ge and Si. Materials Research Bulletin. 1968;**3**:37-46. DOI: 10.1016/0025-5408(68)90023-8

[14] Rosencwaig A. Theoretical aspects of photoacoustic spectroscopy. Journal of Applied Physics. 1978;**49**:2905-2910. DOI: 10.1063/1.325175

[15] McDonald FA, Wetsel GC. Generalized theory of the photoacoustic effect. Journal of Applied Physics. 1978;**49**:2313-2322. DOI: 10.1063/1.325116

[16] Piccirillo C, Dunnill CW, Pullar RC, Tobaldi DM, Labrincha JA, Parkin IP, Pintado MM, Castro PML. Calcium phosphate-based materials of natural origin showing photocatalytic activity. Journal of Materials Chemistry A. 2013;**1**(21):6452-6461. DOI: 10.1039/C3TA10673J

[17] Bystrov VS, Piccirillo C, Tobaldi DM, Castro PML, Coutinho J, Kopyl S, Pullar RC. Oxygen vacancies, the optical band gap (Eg) and photocatalysis of hydroxyapatite: Comparing modelling with measured data. Applied Catalysis B: Environmental. 2016;**196**:100-107. DOI: 10.1016/j.apcatb.2016.05.014

[18] Santos RDS, Rezende MVS. Atomistic simulation of intrinsic defects and trivalent and tetravalent ion doping in hydroxyapatite. Advances in Condensed Matter Physics. 2014; **2014**:609024. DOI: 10.1155/2014/609024

[19] de Leeuw NH, Bowe JR, Rabone JAL. A computational investigation of stoichiometric and calcium-deficient oxy-deficient hydroxyl-apatites. Faraday Discussions. 2007;**134**:195-214. DOI: 10.1039/b602012g

[20] de Leeuw NH. Computer simulations of structures and properties of the biomaterial hydroxyapatite. Journal of Materials Chemistry. 2010;**20**:5376-5389. DOI: 10.1039/b921400c

[21] Rosencwaig A, Gersho A. Theory of the photoacoustic effect with solids. Journal of Applied Physics. 1976;**47**:64-69. DOI: 10.1063/1.322296

[22] Almond D, Patel P. Photothermal Sciences and Techniques. 1st ed. Devon: Chapman & Hall; 1996. p. 119. ISBN: 0 412 57880 8

[23] Coelho TM, Nogueira ES, Weinand WR, Lima WM, Steimacher A, Medina AN, Baesso ML, Bento AC. Thermal properties of natural nanostrunctured hydroxyapatite extracted from fish bone waste. Journal of Applied Physics. 2007;**101**:084701. DOI: 10.1063/1.2718866

[24] Calderón A, Peña Rodríguez G, Muñoz Hernández RA, Díaz Góngora JAI, Mejía Barradas CM. Thermal diffusivity in bone and hydroxyapatite. In: Vargas-Luna M, editor. Medical Physics: Eighth Mexican Symposium on Medical Physics; Guanajuato, Gto, Mexico. Melville, NY: AIP Publishing; 2004. pp. 278-281

[25] Martínez K, Marín E, Glorieux C, Lara-Bernal A, Calderón A, Peña Rodríguez G, Ivanov R. Thermal diffusivity measurements in solids by photothermal infrared radiometry:

Influence of convection-radiation heat losses. International Journal of Thermal Sciences. 2015;**98**:202-207. DOI: 10.1016/j.ijthermalsci.2015.07.019

[26] Bissieux C, Pron H, Henry JF. Photothermal and thermomechanical infrared thermography. In: Moares EM, editor. Thermal Wave Physics and Related Photothermal Techniques: Basic Principles and Recent Developments. Transworld Research Network; 2009. pp. 253-285. ISBN: 978-81-7895-401-1

Chapter 6

The Synthesis and Characterization of Nickel and Cobalt Ferrite Nanopowders Obtained by Different Methods

Ilmars Zalite, Gundega Heidemane, Janis Grabis and Mikhail Maiorov

Additional information is available at the end of the chapter

http://dx.doi.org/10.5772/intechopen.76809

Abstract

The single-phase $NiFe_2O_4$ and $CoFe_2O_4$ ferrites were synthesized by four methods: the high-frequency plasma chemical synthesis ("plasma"), sol-gel self-propagating combustion method ("combust"), and co-precipitation technology, combined with the hydrothermal synthesis ("hydrotherm") or spray-drying ("spray"). The specific surface area (SSA), crystallite size, and magnetic properties of the synthesized products have been determined. The synthesized ferrites are nanocrystalline single-phase materials with crystallite size of 5-40 nm. The SSA of nanoparticles synthesized in plasma is 28-30 m^2/g, the particle size distribution is in the range of 10-100 nm, with some individual particles up to 200 nm. The SSA of the ferrites obtained by the self-combustion and hydrothermal synthesis is 40 ± 3 and 60 ± 5 m^2/g, respectively. The SSA of the samples obtained by the spray-drying method is 80-90 m^2/g, and the calculated particle size is 13-15 nm. In this process, pellets up to 10 μm are obtained. After synthesis, $CoFe_2O_4$ are characterized by the saturation magnetization M_s of 75 emu/g ("plasma"), 53 emu/g ("combust") and 57 emu/g ("hydrotherm"). The M_s of NiFe2O4 is 44, 29, and 30 emu/g, respectively. The products obtained by the spray-drying method are partially X-ray amorphous and show magnetic properties only after heating above 450°C. These nanopowders were used in sintering studies.

Keywords: $NiFe_2O_4$, $CoFe_2O_4$, nanoparticles, synthesis, properties

1. Introduction

Ferrites are a wide range of minerals and synthetic materials, which have attracted a wide range of scientists' interest due to their various applications. Ferrites are technologically significant

materials due to their unique electrical, dielectric, electronic, mechanical, magnetic, optical and catalytic properties. These ferrites are characterized by good magnetic properties [1], low ($NiFe_2O_4$) [2] or high ($CoFe_2O_4$) [3] magnetic coercivity, high electrical resistivity and negligible eddy current loss for high-frequency electromagnetic wave propagation [2], chemical stability and fairly high mechanical hardness [4], low dielectric losses and high Curie temperature [5]. $CoFe_2O_4$ has a high permeability in the radio frequency range [6], high thermal stability [7], moderate saturation magnetization [3] and electrical conductivity [8].

The most significant and most popular use of ferrites is in optics, electronics, mechanics and other technical fields [9]. Ferrites also play a major role in medicine, biomedical applications, as chemical catalysis and special coatings (antistatic, electromagnetic shielding). Scientific articles contain extensive information on hyperthermia. This method introduces ferrite nanoparticles into living organisms and, under controlled conditions, nanoparticles are transported to the cancerous areas of the body, and cancer cells are destroyed in a magnetic field by heat treatment [10].

Ferrites have become suitable for many technological applications such as microwave devices [11] and telecommunication devices, electric motors and generators, as excellent core material for power transformers in electronics, antenna rods, loading coils and read/write heads for high speed digital tape [1], tape recorders and discs [3], high-density information storage and recording devices and as permanent magnets [11], sensors [12], and so on. Magnetic nanoparticles and in particular magnetic fluids (ferrofluids) are particularly important in biotechnology and biomedicine—the supply of biomedical drugs and as contrast media [12], in medical diagnostics [13]. Ferrite materials are widely used in catalysts [12]. In recent years, ferrite materials have been used to prevent and eliminate radio frequency interference in audio systems [4], as polarized ferroelectric ceramics in acoustic elements in underwater converters [14] and microwave absorbing materials [15], including ferrite-containing radar absorbing paints for masking military aircraft [16]. Lately, it has been discovered that cobalt ferrite nanoparticles can also act as photomagnetic material that shows interesting light-induced coercivity changes [17].

Ferrites in a nanocrystalline state (i.e., below single domain sizes [9]) are often found to have unique physical and mechanical properties compared to coarse-grained polycrystalline materials [18]. It is known that the properties of nanocrystalline ferrite materials, including dielectric constant, conductivity, permeability, and other magnetic properties are determined by their microstructure [19], which, in turn, is influenced by the method of their production [8], that is, the synthesis methods [1]. It is well known that the microstructure, in particular the crystallite size, essentially determines the parameters of the hysteresis loop of soft ferromagnetic materials [20]. Samples obtained with different synthesis methods show different electrical and magnetic properties [4]. Therefore, many new nanoparticle production techniques have been developed in recent years.

Ferrites, as the majority of ceramic materials, are obtained by reactions of solid phase from various oxides [21]. The development of nanotechnological processes has resulted in the development of several liquid phase and gas phase synthesis methods—chemical co-precipitation

http://dx.doi.org/10.5772/intechopen.76809

method [22], the sol-gel method [23], combustion reaction synthesis [24], hydrolysis [25], hydrothermal synthesis [26], salt melt technique [6], pyrolysis, various microwave synthesis methods [1] including microwave refluxing [27], microwave plasma [28] and microwave hydrothermal methods [29], high energy ball milling techniques [30], microemulsion methods [31], sono-chemical reactions [32], vapor deposition [33], precursor methods [34] and plasma synthesis [35].

In this work, we have tried to summarize our research results on ferrite nanoparticles produced by different methods and to compare their properties, including magnetic properties.

2. Experimental procedure

In research, nickel and cobalt ferrite nanopowders are obtained by the chemical sol-gel self-propagating combustion ("combust.") method [36], the co-precipitation technology in combination with hydrothermal synthesis ("hydrotherm.") [37] or spray-drying ("spray") [38] method and high-frequency plasma chemical synthesis ("plasma") [39]. The obtained nanopowders have been studied for mechanical and magnetic properties.

The synthesis of cobalt and nickel ferrites by the sol-gel self-propagating combustion method was carried out using reagent grade chemicals: $Co(NO_3)_2 \cdot 6H_2O$, $Ni(NO_3) \cdot 6H_2O$, $Fe(NO_3)_3 \cdot 9H_2O$, glycine, nitric acid [36]. A 100 ml 0.1 M cobalt (or nickel) nitrate solution was added to a 200 ml 0.1 M iron nitrate solution. The glycine was separately dissolved in 100 ml of distilled water, nitric acid added and both added to the nitrate mixture. Glycine (Gly) was used as a self-combustion agent with a molar ratio Me/Gly = 1: 0.8 and Gly/Nitr. = 1:4. The mixture was evenly stirred until the mixture has congealed. Then the mixture was heated until it ignited, and the heating was continued at 300°C for 4 h.

By the co-precipitation method, cobalt and nickel ferrites were synthesized using reagent grade chemicals: $FeCl_3 \cdot 6H_2O$, urea, $Co(NO_3)_2 \cdot 6H_2O$ or $Ni(NO_3)_2 \cdot 6H_2O$, NaOH [37]. The precursor was obtained as follows: urea was hydrolyzed for 3 h in a $FeCl_3 \cdot 6H_2O$ solution (molar ratio of 3: 1) at 70–75°C. Cobalt or nickel nitrate was added the cooled reaction mixture. The molar ratio $FeCl_3 \cdot 6H_2O$: $Co(NO_3)_2 \cdot 6H_2O$ or $Ni(NO_3)_2 \cdot 6H_2O$ corresponds to the metal ion stoichiometry in ferrite. Continually stirring the suspension with 40% NaOH solution, cobalt or nickel hydroxide was slowly precipitated until the pH of the suspension reached 9–10. Then the suspension was placed in an ultrasonic bath for 20 min and then treated for 24 h at 40°C. The sediment was then washed with distilled water by decantation until the presence of Cl ions was no longer detected. Next are two processing options:

A. by the hydrothermal method, the volume of the hydroxides mixture is reduced by decanting to 250 ml, poured into the reaction vessel and placed in an autoclave. The hydroxide mixture was then treated hydrothermally at different temperatures (200–250°C, 1–3 h, p = 17–17.5 MPa). After hydrothermal treatment, the formed precipitate was filtered with a water jet pump using a 5 μm membrane filter and washed with distilled water and dried at 40°C;

B. for spraying the hydroxide mixture with the spray-drying method, the pelleting machine was used developed by RTU Institute of Inorganic Chemistry. Main parameters of the suspension spray: hot air temperature and consumption of 370°C and 24 m^3/h, temperature in evaporating chamber 120–130°C.

Technological equipment developed by the Institute of Inorganic Chemistry of the Riga Technical University [35] was used for the production of ferrites by means of high-frequency (HF) plasma chemical synthesis. Commercial metals and metal oxides (Ni, Co, NiO, CoO and FeO) powders were evaporated in HF plasma to obtain ferrites. All raw materials in stoichiometric ratios (to obtain $NiFe_2O_4$ and $CoFe_2O_4$) were injected into nitrogen plasma at an average temperature of 5800–6200 K. After evaporation of the raw materials, the vapor was cooled very quickly with the cooling gas (air) and the product condensed on the filter in the form of nanosized ferrite particles.

Ferrite nanopowders for sintering were prepared as follows: the ferrite nanopowder samples were mechanically mixed for 1 h in a planetary mill with 3% by weight of stearic acid (400 rpm, ZrO_2 container, ZrO_2 ball material) using isopropanol as a dispersing medium. Stearic acid was used for better pressing. After mixing, the samples were dried in an oven at 80°C and sieved through a 200 μm sieve. For sintering without pressure samples were pressed (200 MPa) as tablets with a diameter of 12 mm and a height of 4–6 mm. Stearic acid was burned out at 600°C. Samples were sintered at 900–1300°C in an air atmosphere at a rate of 10°C/min in an oven LHT-08/18 (Nabertherm GmbH) for 2 h.

All samples were analyzed using the X-ray diffractometer Advance 8 (Bruker AXS). The size of the crystallites was calculated using the Scherer's equation. The magnetic properties of the synthesized ferrites were analyzed using vibrating sample magnetometry (VSM Lake Shore Cryotronics, Inc., Model 7404 VSM). The SSA was measured using the BET single point method. The size and morphology of the particles as well as the microstructure of the sintered material were studied using transmission electron microscope JEM-100S (JEOL) and a scanning electron microscope Mira/Tescan and Tescan Lyra-3 on the fracture surfaces. The density and open porosity of the sintered samples were determined by the Archimedes method.

3. Results

The characteristics of synthesized ferrites are given in **Table 1** and **Figures 1–5**. It has been found that all synthesized ferrites, with the exception of the spray-drying method, are nanocrystalline stoichiometric single-phase powders (**Figure 1**) with a SSA in the wide range of 30–55 m^2/g depending on the synthesis method and calculated (average) particle size of 20–40 nm (**Table 1**, **Figure 2**). The crystallite size of these ferrites is also in the range of 10–40 nm. During the spray-drying process high-dispersity nanoparticles, mainly consisting of cobalt or nickel ferrite, iron hydroxide FeO(OH), and X-ray amorphous part of the sample [38] were obtained. The SSA of these samples was in the range of 80–90 m^2/g (**Table 1**), but the calculated average particle size was 13–15 nm [38]. In this process, pellets of up to 10 μm were obtained (**Figure 3**).

The finer particles were obtained in the spray-drying process, hydrothermal and sol-gel self-propagating combustion synthesis, but the distribution of the particle size of ferrites obtained

Sample	SSA, m^2/g	d_{50}, nm*	Crystallite size, nm	Phase composition	M_s, emu/g	M_r, emu/g	H_c, Oe
$CoFe_2O_4$ (plasma)	29	39	40	$CoFe_2O_4$	75.4	32.0	780
$CoFe_2O_4$ (combust.)	37	31	20	$CoFe_2O_4$	53.4	20.3	1170
$CoFe_2O_4$ (hydrotherm.)	54	21	10–12	$CoFe_2O_4$	50.1	12.6	390
$CoFe_2O_4$ (spray)	84	14	—	p.a. $CoFe_2O_4$, FeO(OH)	—	—	—
$NiFe_2O_4$ (plasma)	29	38	40	$NiFe_2O_4$	44.2	10.0	74
$NiFe_2O_4$ (combust.)	43	26	10	$NiFe_2O_4$	21.4	2.3	81
$NiFe_2O_4$ (hydrotherm.)	42	26	22	$NiFe_2O_4$	39.0	2.6	23
$NiFe_2O_4$ (spray)	85	13	—	p.a. $NiFe_2O_4$, FeO(OH)	—	—	—

*Average particle size calculated from SSA.
p.a.—partially amorphous; M_s—saturation magnetization; M_r—remanent magnetization; H_c—coercivity

Table 1. Properties of synthesized ferrite nanopowders.

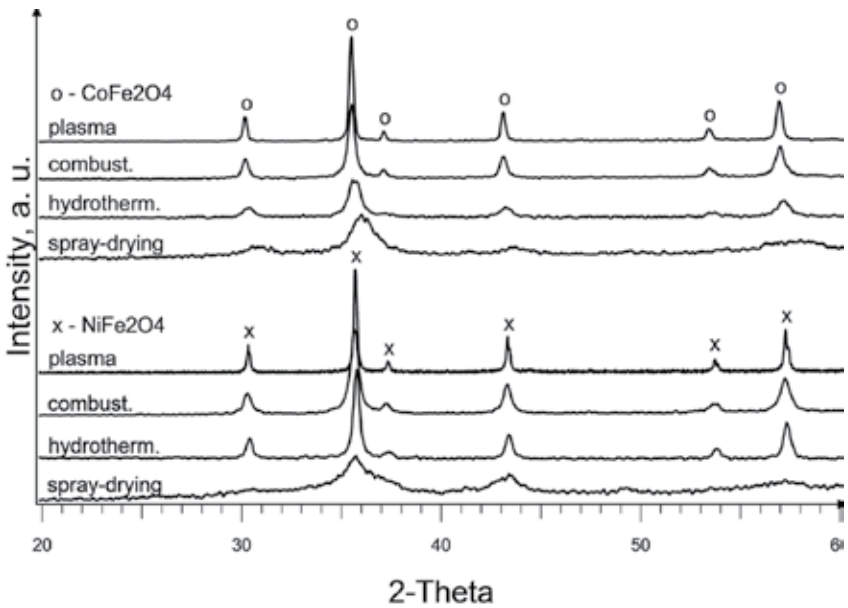

Figure 1. XRD pattern of ferrite nanopowders.

by the plasma synthesis is the most extensive (20–100 nm) with individual particles up to 200 nm. Plasma-derived particles are spherical.

The samples obtained at the optimal synthesis conditions were very clean because any other additional phase (usually magnetite, maghemite, hematite or other metal oxides) was not found by

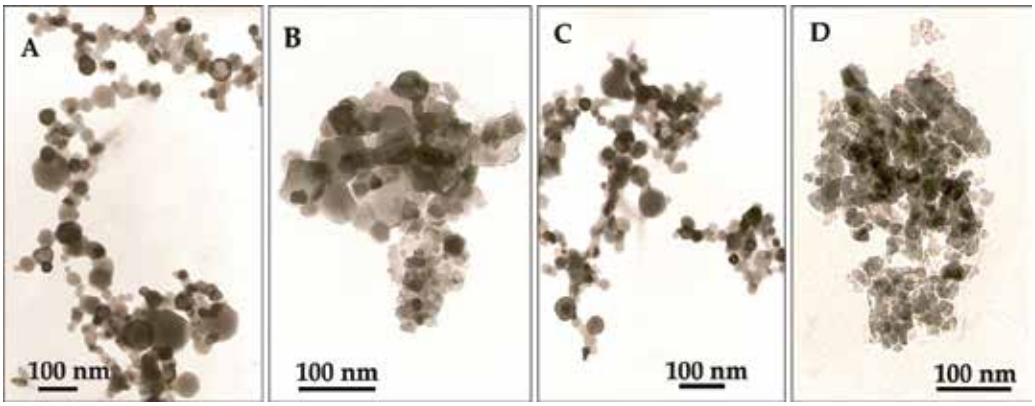

Figure 2. The electron microscope image of $CoFe_2O_4$ (A, C) and $NiFe_2O_4$ (B, D) obtained by the plasma synthesis (A), self-combustion (B), hydrothermal (C) and spray (D) methods.

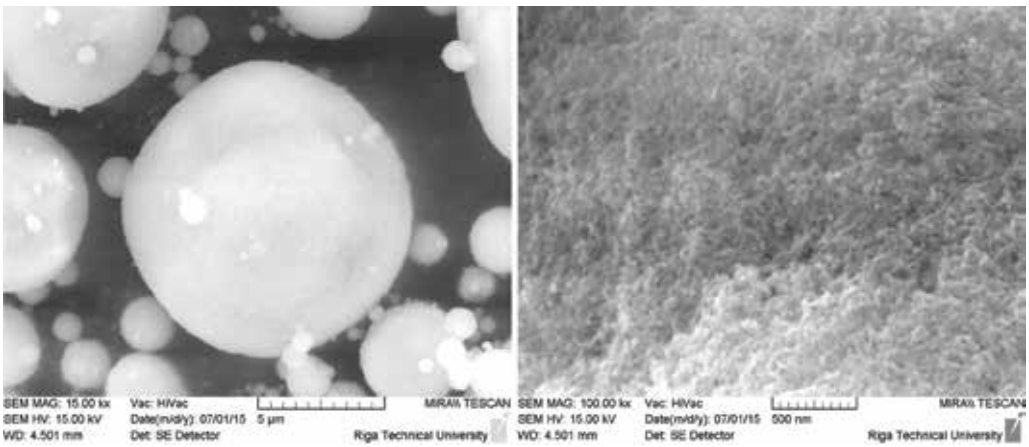

Figure 3. The electron microscope (SEM) images of spray-dried $NiFe_2O_4$ at different enlargements.

the X-ray analysis. By analyzing samples of ferrites produced by different methods, slight differences in relative intensity and width of reflexes, indicating differences in crystallite size (**Figure 1**), can be seen in the X-ray images. The self-combustion and hydrothermal synthesis methods give nanopowders with a lower crystallite size than those obtained by plasma synthesis (**Table 1**).

The magnetic properties of the nanoparticles obtained by the plasma synthesis process (**Table 1**, **Figure 4**) are very close to those of the standard dense material ($CoFe_2O_4$ magnetic saturation values are 80 emu/g and $NiFe_2O_4$ 50 emu/g [40]). In contrast, the samples prepared by self-combustion and hydrothermal method have different magnetic properties than those obtained by plasma synthesis. This is probably due to difference in the size of nanoparticles obtained by plasma, self-combustion and hydrothermal synthesis. The products obtained by the spray-drying method have magnetic properties only after heat treatment at 400–450°C at 550°C, the saturation magnetization of nickel ferrite is 16.9 emu/g, while for the cobalt ferrite is 51.3 emu/g.

http://dx.doi.org/10.5772/intechopen.76809

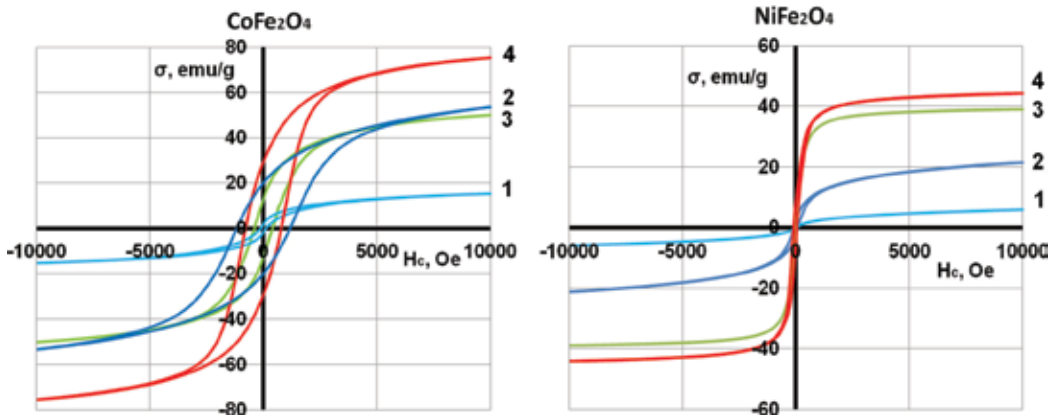

Figure 4. Magnetic properties of ferrites synthesized by the spray-drying (1) at 450°C, sol-gel self-combustion (2) and hydrothermal (3) method and in plasma (4).

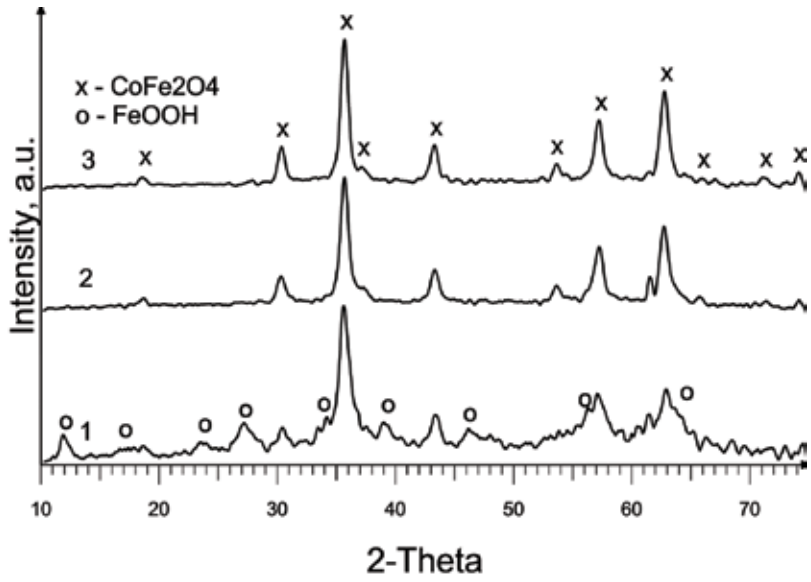

Figure 5. XRD pattern of the hydrothermally synthesized $CoFe_2O_4$ nanopowder prepared at: 1–200°C, 1 h; 2–230°C, 1 h; 3–250°C, 1 h.

Another interesting feature of nanoparticles synthesized in this study is their magnetic behavior, that is, although for all synthesized powders the particle size is below the critical size of a single domain (about 70 nm [41]), quasi-supermagnetic behavior is observed only for plasma-synthesized $NiFe_2O_4$ nanoparticles.

As an example of the impact of synthesis parameters, $CoFe_2O_4$ hydrothermal synthesis can be mentioned. Synthesizing at 200°C for 1 h, the product contains also FeO(OH) in addition to the basic phase (**Figure 5**). The product has weak magnetic properties (**Table 2**). Experiments

No	Mode, °C /h	SSA, m²/g	d_{50}, nm*	Crystallite size, nm	XRD phases	Magnetic properties		
						M_s, emu/g	M_r, emu/g	H_c, Oe
1	200/1	58	20	~10	$CoFe_2O_4$, FeO(OH)	13.2	2.6	105
2	200/3	59	19	13–14	$CoFe_2O_4$	—	—	—
3	230/1	63	18	10–13	$CoFe_2O_4$	50.0	10.2	494
4	230/3	55	21	15–16	$CoFe_2O_4$	58.9	17.8	643
5	250/1	61	19	12–13	$CoFe_2O_4$	57.3	17.3	566
6	250/3	62	18	10–12	$CoFe_2O_4$	59.8	16.8	574

*Calculated from SSA.

Table 2. Characteristics of $CoFe_2O_4$ nanopowders prepared hydrothermally.

have shown that the optimum synthesis temperature, when the pure one-phase product is formed, is from 230°C. Increasing the processing temperatures (up to 250°C) and time (up to 3 h) does not significantly affect the size of the specific surface area and crystallite. Increasing of the synthesis temperature and hydrothermal treatment time results in a small increase in magnetic characteristics (saturation magnetization M_s, remanent magnetization M_r and coercivity H_c) (**Table 2**).

After thermal treatment at higher temperatures, ferrite nanopowders synthesized by self-combustion, hydrothermal and spray-drying method, tend to decrease their SSA, but the particle size and crystallite size increase (**Figure 6**). This trend can be explained by the fact that the particles recrystallize and grow at higher temperatures, so the specific surface decreases. With the increase of crystallite size, the saturation magnetization and remanent magnetization of ferrites increase (**Tables 3** and **4**, **Figures 7** and **8**). For example, after thermal treatment of $CoFe_2O_4$ obtained by self-combustion and hydrothermal method at 800°C and more, the saturation magnetization increases to 80 and 72 emu/g, respectively.

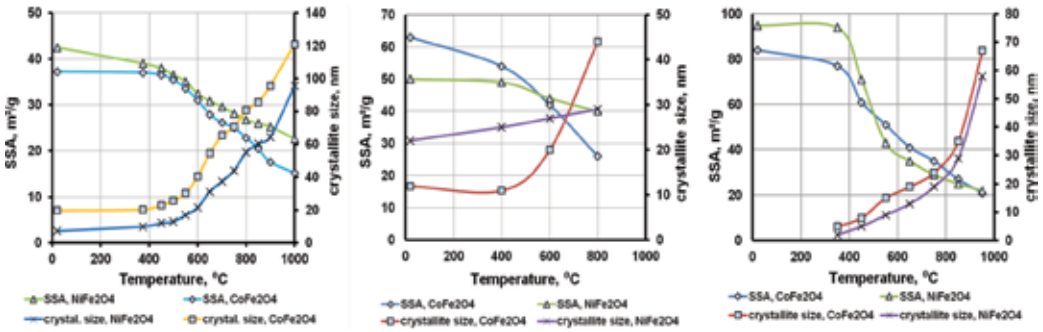

Figure 6. Specific surface area (SSA) and crystallite size comparison depending on temperature for $NiFe_2O_4$ and $CoFe_2O_4$ synthesized by the sol-gel self-combustion (A), the hydrothermal (B) and spray-drying (C) method.

Samples	Heating temperature, °C	M_s, emu/g	M_r, emu/g	H_c, Oe
$CoFe_2O_4$ combust.	Raw powder	53.4	20.3	1170
	450	55.0	21.7	1190
	650	76.1	39.3	1350
	850	79.9	35.7	930
	900	79.8	31.3	980
$CoFe_2O_4$ hydrotherm.	Raw powder	50.0	10.2	495
	400	50.1	12.6	390
	600	62.8	22.4	760
	800	71.6	28.9	875
$CoFe_2O_4$ spray	Raw powder	—	—	—
	350	—	—	—
	550	51.3	14.7	649
	750	61.1	22.3	878
	950	76.8	34.1	1067

Table 3. Magnetic properties of $CoFe_2O_4$ synthesized by the sol-gel self-combustion, hydrothermal and spray-drying methods after thermal treatment (2 h at different temperatures).

The spray-dried powder after the synthesis and granulation is partially amorphous and contains a small amount of FeO(OH). After heat treatment, starting from 400 to 450°C, a stoichiometric, single-phase nanocrystalline powder ($NiFe_2O_4$ or $CoFe_2O_4$) (**Figure 9**) was formed, with SSA from 100 (at 350°C) to 20 m^2/g (at 950°C) (**Figure 6**). The crystallite size at 350°C is 4 and 6 nm, respectively for $NiFe_2O_4$ and $CoFe_2O_4$, which increases with the increase of the processing temperature. The saturation magnetization (M_s) of the $NiFe_2O_4$ and $CoFe_2O_4$ ferrites increases, respectively, from 6 and 15 emu/g (at 450°C) to 40 and 77 emu/g (at 950°C) (**Tables 3** and **4**, **Figure 8**).

The relative density of samples before sintering was of 51–52% for plasma synthesized products and of 31–33% for products obtained by other methods. This shows that the ferrite nanopowders obtained by these methods are more difficult to compress because their particles are finer than ferrite powders synthesized in plasma.

Nanosized ferrite powders were sinteredat 900–1300°C. The density of ferrites after the heat treatment is shown in **Table 5**.

The sintering process of plasma synthesis products is the fastest compared with all investigated nanopowders: they have a high density at 900°C, but above 1000°C, the density is approaching already 100%. $CoFe_2O_4$ ferrites synthesized by other methods have a relatively high density at 1100°C, while $NiFe_2O_4$ ferrites require the temperature of 1200°C or higher to achieve high density. Although the sintering temperature of the ferrites obtained by the

Samples	Heating temperature, °C	M_s, emu/g	M_r, emu/g	H_c, Oe
$NiFe_2O_4$ combust.	Raw powder	29.0	6.0	120
	450	31.4	4.8	130
	650	37.4	9.1	200
	850	45.2	14.8	145
	900	47.4	15.0	135
$NiFe_2O_4$ hydrotherm.	Raw powder	37.4	2.6	23
	400	36.7	3.8	34
	600	40.2	5.2	55
	800	42.6	5.0	70
$NiFe_2O_4$ spray	Raw powder	—	—	—
	350	—	—	—
	550	16.9	1.1	57
	750	21.6	4.5	214
	950	40.0	8.6	151

Table 4. Magnetic properties of $NiFe_2O_4$ synthesized by the sol-gel self-combustion, hydrothermal and spray-drying methods after thermal treatment (2 h at different temperatures).

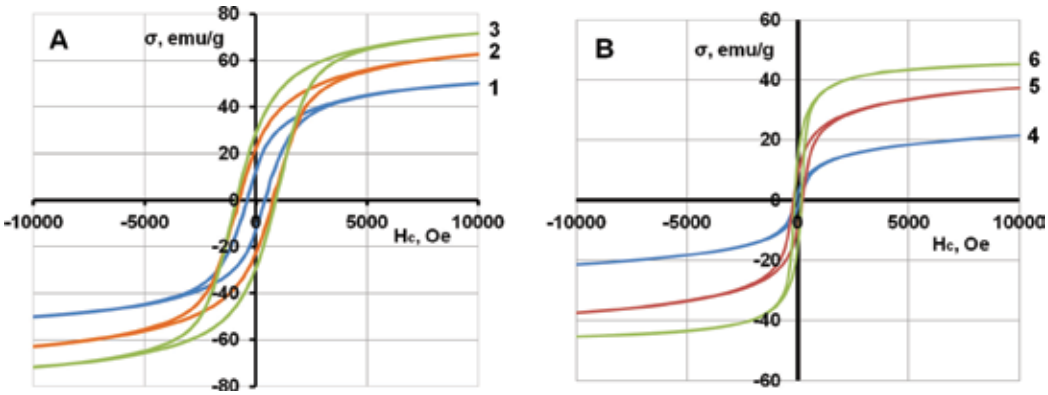

Figure 7. The magnetic properties of the sample $CoFe_2O_4$ prepared by the hydrothermal synthesis (A) after thermal treatment at 400°C (1), 600°C (2) and 800°C (3), $NiFe_2O_4$ prepared by the self-combustion synthesis (B) after thermal treatment at 450°C (4), 650°C (5) and 850°C (6).

spray method is slightly higher, they could be the most promising on the technological point of view among all these nanopowders because they are flowing and can be pressed without further treatment.

http://dx.doi.org/10.5772/intechopen.76809

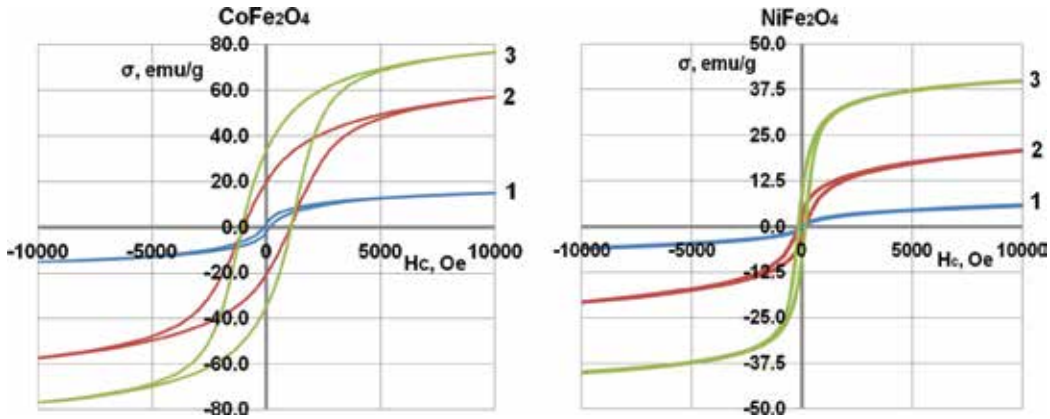

Figure 8. The magnetic properties of samples of $CoFe_2O_4$ and $NiFe_2O_4$ after thermal treatment at 450 (1), 650 (2) and 950 (3)°C prepared by the spray-drying method.

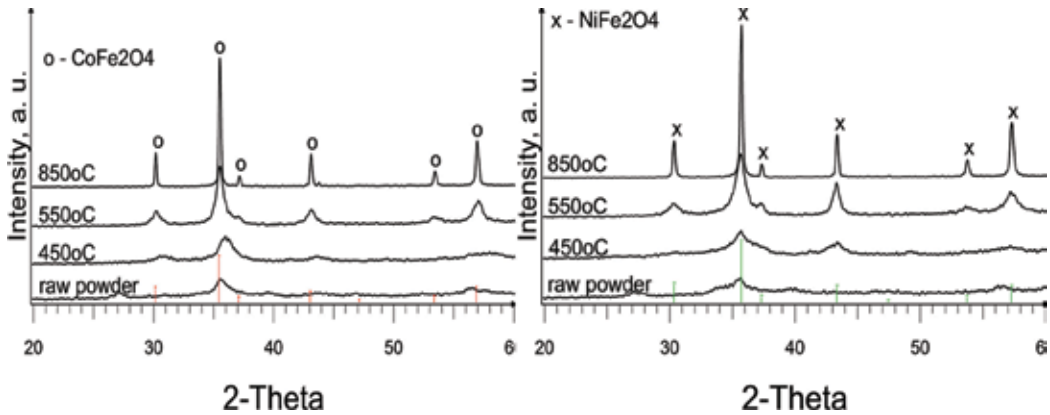

Figure 9. XRD pattern of spray-dried $CoFe_2O_4$ and $NiFe_2O_4$ ferrite nanopowders.

The crystallite size grows slightly during sintering: from 70 to 80 nm at 1100°C to 120–140 nm at 1300°C. For example, the crystallite size of hydrothermal $CoFe_2O_4$ varies from 10 to 13 nm in the raw powder to 75 nm (1000°C) and 150 nm (sintered at 1200°C). The grain size of samples sintered at 1200°C, obtained from self-combustion, hydrothermal and spray-dried powders, does not exceed 1 to 6 μm (**Figure 10**). As a result of high sintering activity, the grain size of plasma-synthesized ferrite outweighs: 10–15 μm for $NiFe_2O_4$ and 10–30 μm for $CoFe_2O_4$.

Compared with the ferrite nanopowders, ceramic materials have a higher saturation magnetization (**Figure 11**) and lower coercivity. This could be explained by the increase in grain size and crystallite size. An increase in the temperature of the sintering results in the increase of the grain size and magnetization for all ferrite materials, while coercivity decreases (**Table 6**).

Sample	Sintering temperature, °C									
	900		1000		1100		1200		1300	
	ϱ, %	$P_{op.}$, %	ϱ, %	$P_{op.}$, %	ϱ, %	$P_{op.}$, %	ϱ, %	$P_{op.}$, %	ϱ, %	$P_{op.}$, %
$CoFe_2O_4$ (plasma)	82.6	16.0	97.0	0.2	98.5	0.1	97.9	0	—	—
$CoFe_2O_4$ (combust.)	—	—	65.7	33.4	78.3	21.6	93.4	3.1	—	—
$CoFe_2O_4$ (hydrotherm.)	—	—	81.3	14.2	94.3	0.8	95.0	0.1	—	—
$CoFe_2O_4$ (spray)	—	—	62.3	35.5	90.0	8.8	90.8	4.7	95.1	0.7
$NiFe_2O_4$ (plasma)	87.9	12.1	99.4	0.2	99.9	0.1	100.0	0	—	—
$NiFe_2O_4$ (combust.)	—	—	72.4	25.5	87.7	9.4	96.1	1.6	—	—
$NiFe_2O_4$ (hydrotherm.)	—	—	—	—	79.1	19.8	85.8	12.0	—	—
$NiFe_2O_4$ (spray)	—	—	52.2	44.0	69.5	27.6	85.3	12.1	90.7	7.1

ϱ—density; P_{op}—open porosity.

Table 5. The relative density and open porosity of ferrites depending on sintering temperature (after 2 h sintering).

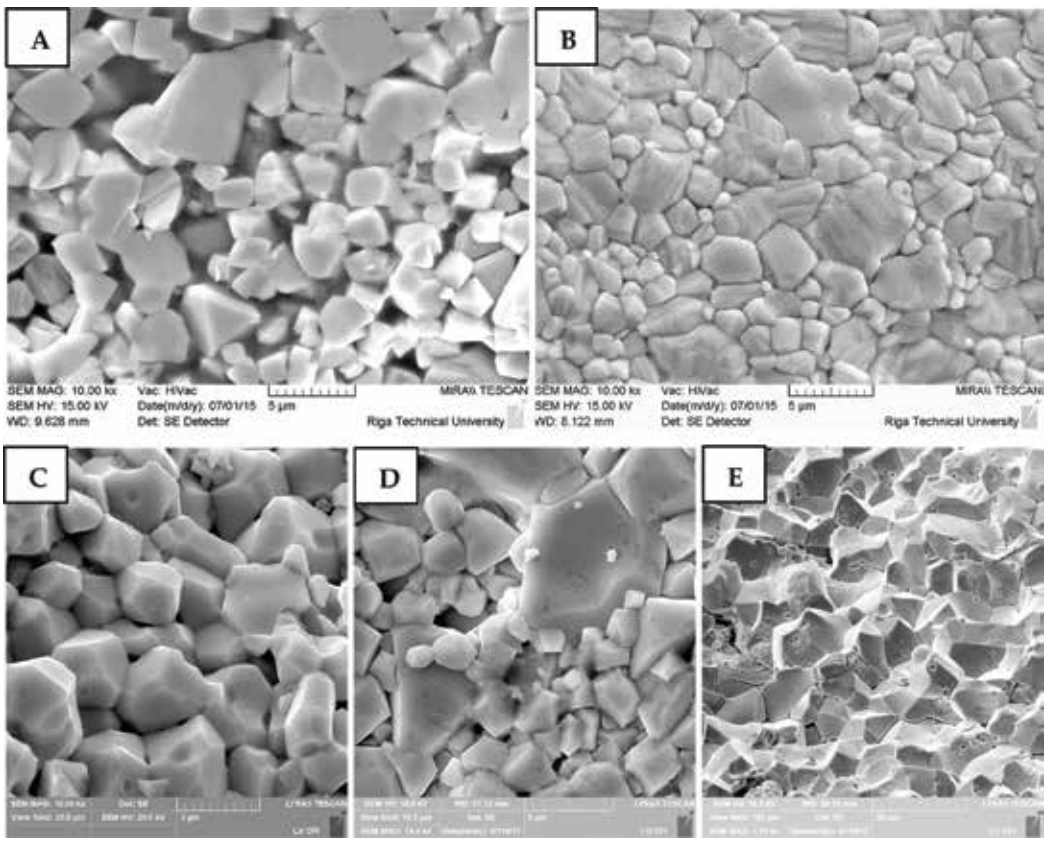

Figure 10. Typical SEM image of $NiFe_2O_4$ (a, D) and $CoFe_2O_4$ (B, C, E) ceramics sintered at 1200°C 2 h. The powders are prepared by hydrothermal (A, B), sol-gel self-propagating combustion (C), spray-drying (D) and plasma (E) methods.

http://dx.doi.org/10.5772/intechopen.76809

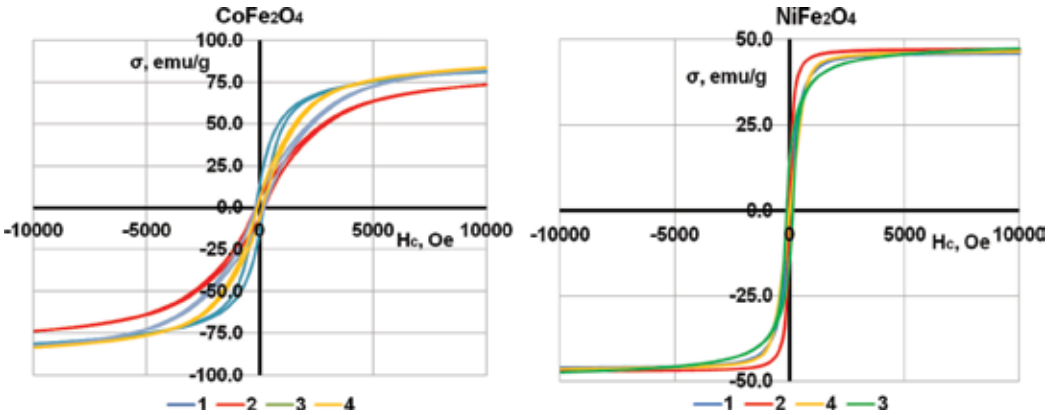

Figure 11. Magnetic properties of $CoFe_2O_4$ (a) and $NiFe_2O_4$ (B) ferrite, sintered at 1200°C from different powders: 1—hydrothermal, 2—spray-drying, 3—combustion, 4—plasma.

Heating temperature, °C	$CoFe_2O_4$			$NiFe_2O_4$		
	M_s, emu/g	M_r, emu/g	H_c, Oe	M_s, emu/g	M_r, emu/g	H_c, Oe
Self-combustion						
1200	82.6	6.9	190	—	—	—
Hydrothermal						
1100	77.0	20.7	493	40.4	6.5	102
1200	81.3	14.1	169	46.0	1.7	15
Spray						
1100	74.6	15.3	427	48.0	3.0	35
1300	73.8	5.9	187	47.0	2.4	11
Plasma						
1100	81.8	14.0	258	45.7	3.8	35
1200	83.6	8.0	110	46.3	0.7	11

Table 6. Magnetic properties of $CoFe_2O_4$ and $NiFe_2O_4$ ceramics after 2 h sintering.

The magnetic properties of the samples sintered at 1200°C are almost the same regardless of the method of extracting ferrite powders: saturation magnetization for $CoFe_2O_4$ is of 80–84 emu/g and 46–48 emu/g for $NiFe_2O_4$.

4. Conclusions

Single-phase nickel and cobalt ferrite nanopowders can be successfully synthesized by the chemical sol-gel self-propagating combustion and co-precipitation method combined with

hydrothermal synthesis or spray-drying method as well as high-frequency plasma synthesis. The magnetic properties of synthesized ferrite powders depend on their synthesis method.

Comparing the methods for obtaining ferrite nanopowders described earlier, we can say that plasma synthesis currently is the most productive method resulting in the highest magnetic properties (75 emu/g for $CoFe_2O_4$ and 44 emu/g for $NiFe_2O_4$). The disadvantage of this method is the presence of particles exceeding the size of 100 nm in a product that is not acceptable in all applications.

The chemical sol-gel self-propagating combustion and hydrothermal synthesis methods enables the production of smaller particles (SSA = 35–55 m^2/g; average particle size 20–30 nm) with less explicited magnetic properties (50–55 emu/g for $CoFe_2O_4$ and 20–40 emu/g for $NiFe_2O_4$) after synthesis, which can be increased after heat treatment at temperatures up to 800°C. The lack of these methods is a time-consuming process of filtering nanoparticles.

The filtration process can be bypassed by the spray-drying method. Here, the smallest particles of the powder (SSA = 80–90 m^2/g, average particle size 10–15 nm) are obtained, but due to the low processing temperatures, they have no explicited magnetic properties. Magnetic properties are observed after additional treatment starting at 400–450°C. However, the granular product is well suited for automated pressing processes for production of ceramic materials.

Sintered materials have higher magnetic properties than nanopowders. Magnetic properties of samples sintered at 1200°C are almost the same regardless of the method of obtaining ferrite powders: the saturation magnetization of $CoFe_2O_4$ is 80–84 emu/g and 46–48 emu/g for $NiFe_2O_4$.

Author details

Ilmars Zalite[1]*, Gundega Heidemane[1], Janis Grabis[1] and Mikhail Maiorov[2]

*Address all correspondence to: ilmars.zalite@rtu.lv

1 Institute of Inorganic Chemistry, Riga Technical University, Riga, Latvia

2 Institute of Physics, University of Latvia, Salaspils, Latvia

References

[1] Costa ACFM, Tortella E, Morelli MR, Kiminami RHGA. Synthesis, microstructure and magnetic properties of Ni–Zn ferrites. Journal of Magnetism and Magnetic Materials. 2003;**256**:174-182. DOI: 10.1016/S0304-8853(02)00449-3

[2] Priyadharsini P, Pradeep A, Chandrasekaran G. Novel combustion route of synthesis and characterization of nanocrystalline mixed ferrites of Ni–Zn. Journal of Magnetism and Magnetic Materials. 2009;**321**:1898-1903. DOI: 10.1016/j.jmmm.2008.12.005

[3] Hou C, Yu H, Zhang Q, Li Y. WangH. Preparation and magnetic property analysis of monodisperse Co–Zn ferrite nanospheres. Journal of Alloys and Compounds. 2010;**491**:431-435. DOI: 10.1016/j.jallcom.2009.10.217

[4] Gul IH, Ahmed W, Maqsood A. Electrical and magnetic characterization of nanocrystalline Ni–Zn ferrite synthesis by co-precipitation route. Journal of Magnetism and Magnetic Materials. 2008;**320**:270-275. DOI: 10.1016/j.jmmm.2007.05.032

[5] Yadoji P, Peelamedu R, Agrawal D, Roy R. Microwave sintering of Ni–Zn ferrites: Comparison with conventional sintering. Materials Science and Engineering: B. 2003;**98**:269-278. DOI: 10.1016/S0921-5107(03)00063-1

[6] Jadhav SS, Patange SM, Jadhav KM. Dielectric behaviour study of nanocrystalline Co-Zn ferrite. Journal of Biomedical and Bioengineering. 2010;**1**:21-29

[7] Ahmed MA, EL-Khawlani AA. Enhancement of the crystal size and magnetic properties of Mg-substituted Co ferrite. Journal of Magnetism and Magnetic Materials. 2009;**321**:1959-1963. DOI: 10.1016/j.jmmm.2008.12.021

[8] Gul IH, Abbasi AZ, Amin F, Anis-ur-Rehman M, Maqsood A. Structural, magnetic and electrical properties of $Co_{1-x}Zn_xFe_2O_4$ synthesized by co-precipitation method. Journal of Magnetism and Magnetic Materials. 2007;**311**:494-499. DOI: 10.1016/j.jmmm.2006.08.005

[9] Xue B, Liu R, Xu ZD, Zheng YF. Microwave Fabrication and Magnetic Property of Hierarchical Spherical α-Fe_2O_3 Nanostructures. Chemistry Letters. 2008;**37**:1058-1059. DOI: 10.1246/cl.2008.1058

[10] Fortin JP, Wilhelm C, Servais J, Menager C, Bacri JCF, Gazeau J. Size sorted anionic iron oxide nanomagnets as colloidal mediators for magnetic hyperthermia. Chemical Society. 2007;**129**:2628-2635. DOI: 10.1021/ja067457e

[11] Gul IH, Amin F, Abbasi AZ, Anis-ur-Rehman M, Maqsood A. Physical and magnetic characterization of co-precipitated nanosize Co–Ni ferrites. Scripta Materialia. 2007;**56**:497-500. DOI: 10.1016/j.scriptamat.2006.11.020

[12] Slatineanu T, Iordan AR, Oancea V, Palamaru MN, Dumitru I, Constantin CP, Caltun OF. Magnetic and dielectric properties of Co–Zn ferrite. Materials Science and Engineering: B. 2013;**178**:1040-1047. DOI: 10.1016/j.mseb.2013.06.014

[13] Arulmurugan R, Jeyadevan B, Vaidyanathan G, Sendhilnathan S. Effect of zinc substitution on Co–Zn and Mn–Zn ferrite nanoparticles prepared by co-precipitation. Journal of Magnetism and Magnetic Materials. 2005;**288**:470-477. DOI: 10.1016/j.jmmm.2004.09.138

[14] Tawfik A. Electromechanical properties of $Co_{0.6}Zn_{0.4}Fe_2O_4$ ferrite transducer. Journal of Magnetism and Magnetic Materials. 2001;**237**:283-287. DOI: 10.1016/S0304-8853(01)00466-8

[15] Kumar S, Singh V, Aggarwal S, Mandal UK, Kotnala RK. Monodisperse Co, Zn-Ferrite nanocrystals: Controlled synthesis, characterization and magnetic properties. Journal of Magnetism and Magnetic Materials. 2012;**324**:3683-3689. DOI: 10.1016/j.jmmm.2012.05.048

[16] Gul IH, Maqsood A. Structural, magnetic and electrical properties of cobalt ferrites prepared by the sol–gel route. Journal of Alloys and Compounds. 2008;**465**:227-231. DOI: 10.1016/j.jallcom.2007.11.006

[17] Giri AK, Kirkpatrick EM, Moongkhamklang P, Majetich SA. Photomagnetism and structure in cobalt ferrite nanoparticles. Applied Physics Letters. 2002;**80**:2341. DOI: 10.1063/1.1464661

[18] Suryanarayana C. Nanocrystalline materials. International Materials Reviews. 1995; **40**:41-64. DOI: 10.1179/imr.1995.40.2.41

[19] van der Zaag PJ, Ruigrok JJM, Noordermeer A, van Delden MHWM. The initial permeability of polycrystalline MnZn ferrites: The influence of domain and microstructure. Journal of Applied Physics. 1993;**74**:4085-4095. DOI: 10.1063/1.354454

[20] Chicinas I. Soft magnetic nanocrystalline powders produced by mechanical alloying routes. Journal of Optoelectronics and Advanced Materials. 2006;**8**:439-448

[21] Akther Hossain AKM, Tabata H, Kawai T. Magnetoresistive properties of $Zn_{1-x}Co_{x}Fe_2O_4$ ferrites. Journal of Magnetism and Magnetic Materials. 2008;**320**:1157-1162. DOI: 10.1016/j.jmmm.2007.11.009

[22] Ferreira TAS, Waerenborgh JC, Mendonça MHRM, Nunes MR, Costaa FM. Structural and morphological characterization of $FeCo_2O_4$ and $CoFe_2O_4$ spinels prepared by a coprecipitation method. Solid State Sciences. 2003;**5**:383-392. DOI: 10.1016/S1293-2558(03)00011-6

[23] Tang DQ, Zhang DJ, Ai H. Fabrication of magnetic core–shell $CoFe_2O_4/Al_2O_3$ nanoparticles as immobilized metal chelate affinity support for protein adsorption. Chemistry Letters. 2006;**35**:1238-1239. DOI: 10.1246/cl.2006.1238

[24] Zhou Z, Zhang Y, Wang Z, Wei W, Tang W, Shi J, Xiong R. Electronic structure studies of the spinel $CoFe_2O_4$ by X-ray photoelectron spectroscopy. Applied Surface Science. 2008;**254**:6972-6975. DOI: 10.1016/j.apsusc.2008.05.067

[25] Duong GV, Hanh N, Linh DV, Groessinger R, Weinberger P, Schafler E, Zehetbauer M. Monodispersed nanocrystalline $Co_{1-x}Zn_xFe_2O_4$ particles by forced hydrolysis: Synthesis and characterization. Journal of Magnetism and Magnetic Materials. 2007;**311**:46-50. DOI: 10.1016/j.jmmm.2006.11.167

[26] Millot N, Gallet SL, Aymes D, Bernard F, Grin Y. Spark plasma sintering of cobalt ferrite nanopowders prepared by coprecipitation and hydrothermal synthesis. Journal of the European Ceramic Society. 2007;**27**:921-926. DOI: 10.1016/j.jeurceramsoc.2006.04.141

[27] Giri J, Sriharsha T, Bahadur D. Optimization of parameters for the synthesis of nanosized $Co_{1-x}Zn_xFe_2O_4$, $(0 \le x \le 0.8)$ by microwave refluxing. Journal of Materials Chemistry. 2004;**14**:875-880. DOI: 10.1039/B310668C

[28] Chau JLH, Hsu MK, Kao CC. Microwave plasma synthesis of Co and SiC-coated Co nanopowders. Materials Letters. 2006;**60**:947-951. DOI: 10.1016/j.matlet.2005.10.054

[29] Kim CK, Lee JH, Katoh S, Murakami R, Yoshimura M. Synthesis of Co-, Co-Zn and Ni-Zn ferrite powders by the microwave-hydrothermal method. Materials Research Bulletin. 2001;**36**:2241-2250. DOI: 10.1016/S0025-5408(01)00703-6

[30] Jiang JZ, Wynn P, Mørup S, Okada T, Berry FJ. Magnetic structure evolution in mechanically milled nanostructured $ZnFe_2O_4$ particles. Nanostructured Materials. 1999;**12**:737-740. DOI: 10.1016/S0965-9773(99)00228-7

[31] Hochepied JF, Bonville P, Pileni MP. Nonstoichiometric zinc ferrite nanocrystals: Syntheses and unusual magnetic properties. The Journal of Physical Chemistry B. 2000;**104**:905-9122. DOI: 10.1021/jp991626i

[32] Shafi KVPM, Gedanken A, Prozorov R, Balogh J. Sonochemical preparation and size-dependent properties of nanostructured $CoFe_2O_4$ particles. Chemistry of Materials. 1998;**10**:3445-3450. DOI: 10.1021/cm980182k

[33] Jalaly M, Enayati MH, Karimzadeh F, Kameli P. Mechanosynthesis of nanostructured magnetic Ni–Zn ferrite. Powder Technology. 2009;**193**:150-153. DOI: 10.1016/j.powtec.2009.03.008

[34] Li F, Liu J, Evans DG, Duan X. Stoichiometric synthesis of pure MFe_2O_4(M = Mg, Co, and Ni) spinel ferrites from tailored layered double hydroxide (hydrotalcite-like) precursors. Chemistry of Materials. 2004;**16**:1597-1602. DOI: 10.1021/cm035248c

[35] Grabis J, Zalite I. Nanosize powders of refractory compounds for obtaining of fine-grained ceramic materials. Materials Science Forum. 2007;**555**:267-272. DOI: 10.4028/www.scientific.net/MSF.555.267

[36] Zalite I, Heidemane G, Kodols M, Grabis J, Maiorov M. The synthesis, characterization and sintering of nickel and cobalt ferrite nanopowders. Materials Science (Medžigotyra). 2012;**18**:3-7. DOI: 10.5755/j01.ms.18.1.1332

[37] Zalite I, Heidemane G, Kuznetsova L, Maiorov M. Hydrothermal synthesis of cobalt ferrite nanosized powders. IOP Conference Series: Materials Science and Engineering. 2015;**77**:5. DOI: 10.1088/1757-899X/77/1/012011

[38] Zalite I, Heidemane G, Palcevskis E, Maiorov M. Properties of nanosized ferrite powders and sintered materials prepared by the Co-precipitation technology, combined with the spray-drying method. Key Engineering Materials. 2016;**721**:295-299. DOI: 10.4028/www.scientific.net/KEM.721.295

[39] Zalite I, Heidemane G, Kuznetsova L, Kodols M, Grabis J, Maiorov M. The synthesis and characterization of nickel and cobalt ferrite nanopowders obtained by different methods. Chemical Technology. 2016;**67**:53-57. DOI: 10.5755/j01.ct.67.1.15824

[40] Smit J, Wijn HPJ. Ferrites: Physical properties of ferrimagnetic oxides in relation to their technical applications. Eindhoven, The Netherlands: Philips Technical Library; 1959. p. 384

[41] Song Q, Zhang ZJ. Correlation between spin-orbital coupling and the superparamagnetic properties in magnetite and cobalt ferrite spinel nanocrystals. Journal of Physical Chemistry B. 2006;**110**:11205-11209. DOI: 10.1021/jp060577o

Chapter 7

Titanium Carbide (TiC) Production by Mechanical Alloying

Héctor Enrique Jaramillo Suárez,
Nelly Alba de Sanchez and Julian Arnaldo Avila Diaz

Additional information is available at the end of the chapter

http://dx.doi.org/10.5772/intechopen.76690

Abstract

This chapter presents the process for obtaining titanium carbides (TiC) from elemental powders of titanium dioxide, aluminum, and graphite by means of the mechanical alloying technique, using a semi-industrial attritor mill. Three grindings were performing: a wet, a dry, and a vacuum grinding. The mass relations between grinding elements and powders used were 20:1 to wet grinding and 40:1 to dry and vacuum grinding. Each grinding took 36 h with a control stop at 18 h. The samples were analyzed using X-ray diffraction analysis and the characteristics peak were detected on $2\theta = 41$, 60, 72, and 76°. Targets of TiC were produced using compaction and sintering processes. The particle size (between 200 nm and 1 μm) was measure using a scanning electron microscopy (SEM). After the milling process, the particle size showed a huge distribution. However, after the sintered process, the particle size (lower than 5 μm) distribution had a low dispersion and their shape trends to be spherical. It is necessary to highlight that the precursors used were low cost compared to the high cost and purity powders used for this purpose; so this method is an excellent alternative to implement as a low-cost industrial process.

Keywords: titanium carbide, mechanical alloy, mechanosynthesis, milling, sintering process

1. Introduction

Such metastable phases as solid supersaturated solutions without crystalline equilibrium or intermediate quasicrystalline stages and amorphous alloys can be synthesized by mechanical alloying [1, 2]. In addition, nanostructures with grain sizes of a few nanometers, usually

<100 nm, can be produced. These metastable phases characteristically have an interesting combination of physical, chemical, mechanical, and magnetic properties that are now being explored due to their potential applications [3].

Mechanically alloyed materials are used in a variety of industries. They are used in the synthesis and processing of advanced materials (magnetic, superconducting, and ceramic materials) such as intermetallic materials, nanocomposites, catalysts, hydrogen-storage materials, gas heaters and dampers, and modifiers of the solubility of organic compounds for waste management and fertilizer production [4]. However, the main industrial applications of mechanically alloyed materials have been in heat treatments, glass processing, energy production, and the aerospace industry.

When in the search for materials which meet increasingly strict requirements, such as high rigidity, high mechanical strength, and low density, such processes as powder technologies and mechanical alloying emerge. These processes do not have any limitations unlike conventional processes, for example, the melting process [5], which is not viable when there are materials with very different melting temperatures, low solubility limits, manufacturing costs due to high energy consumption, and environmental impact problems. In this respect, the mechanical alloying is a non-traditional technique, industrially competitive in obtaining composite materials, easy to use, low cost, and environmentally friendly [6]. This process produces alloys in solid state from elemental powders of any type of material [1], using the impact energy produced by milling elements.

The materials produced by mechanical alloying have a good thermal stability of their mechanical properties. The stability of the mechanical strength is due to the uniform dispersion (with a spacing range of 100 nm) with very fine oxide particles (5–50 nm), which are stable at high temperatures, and inhibit the movement of dislocations in the metallic matrix and increase the strength of the creep deformation alloy. Other characteristic is a fairly homogeneous distribution of the elements of the alloy during the mechanical alloying that gives rise to a solid solution (strengthening) and precipitation-hardening alloys with more stability at high temperatures and a general improvement of the mechanical properties.

The materials obtained by mechanical alloying also have excellent resistance to oxidation and corrosion, which is mainly due to the homogeneous distribution of the alloying elements and adhesion between particles [7, 8]. Due to these characteristics, these materials are widely used in aerospace applications [9], where materials with high mechanical performance are generally needed, due to the unfavorable conditions of use.

In this sense, this chapter presents the process for obtaining titanium carbides (TiC) at a laboratory level. The TiC was obtained from elemental powders of titanium dioxide, aluminum, and graphite by means of the mechanical alloying technique, using a semi-industrial capacity attritor mill.

2. Experimental data

2.1. Initial hypothesis

To obtain titanium carbides, a chemical analysis was conducted:

$$TiO_2 + C + Al \rightarrow TiC + Al_2O_3 \quad (1)$$

On performing the balancing of Eq. (1), we have.

$$3TiO_2 + 3C + 4Al \rightarrow 3TiC + 2Al_2O_3 \tag{2}$$

From Eq. (2), the molar mass of the elements involved in the reaction was determined and the weight of the powders involved in the mechanical alloying process was calculated (**Table 1**). The percentage of participation for each initial powder was calculated as.

$$\%\,\mathrm{Re}activo = \frac{W}{W_t} x100\% \tag{3}$$

where W is the weight of the reactive powder and W_t is the total weight of the reagent.

So,

$$\%TiO_2 = \frac{239.7}{383.7} x100\% = 62.4\% \tag{4}$$

$$\%C = \frac{36.0}{383.7} x100\% = 9.4\% \tag{5}$$

$$\%Al = \frac{108.0}{383.7} x100\% = 28.1\% \tag{6}$$

2.2. Milling characteristics

During the experimental process, three initial millings were made: two wet millings and one vacuum dry milling, in order to fine-tune the process parameters. Once the process parameters have been fine-tuned (**Table 2**), milling was performed to obtain the TiC.

Chemical element	Mass (g/mol)	Left side of Eq. (2)		Right side of Eq. (2)	
		Moles	Mass (g)	Moles	Mass (g)
Ti	47.9	3	143.7	3	143.7
O_2	16.0	3	96.0	3	36.0
C	12.0	3	36.0	2	108.0
Al	27.0	4	108.8	2	96.0
Total		13	383.7	10	383.7

Table 1. Balancing chemical.

Process	Grinding	Initial powders (g)	Ratio $M_{balls}/M_{powders}$	Pressure (Torr)	Velocity (rpm)	Grinding time (h)
Wet grinding	Grinding 1	500	20:1	6.7×10^2	250	5
	Grinding 2	250	40:1	6.7×10^2	300	7
Dry grinding	Grinding 3	250	40:1	8.0×10^{-3}	500	12

Table 2. Experimental process details of powder grinding.

2.2.1. The mill

To make the millings, an attritor-type ball mill was used; it was developed and built by Universidad Autónoma de Occidente for this purpose (www.uao.edu.co) (**Figure 1**). The bowl of the mill has a maximum capacity of 2 l and the impeller has a rotation speed of 500 rpm. The bowl has a torispherical lid and the assembly is able to withstand temperatures over 300°C and pressures of 1.72 MPa (175 psi), which ensures a protective atmosphere.

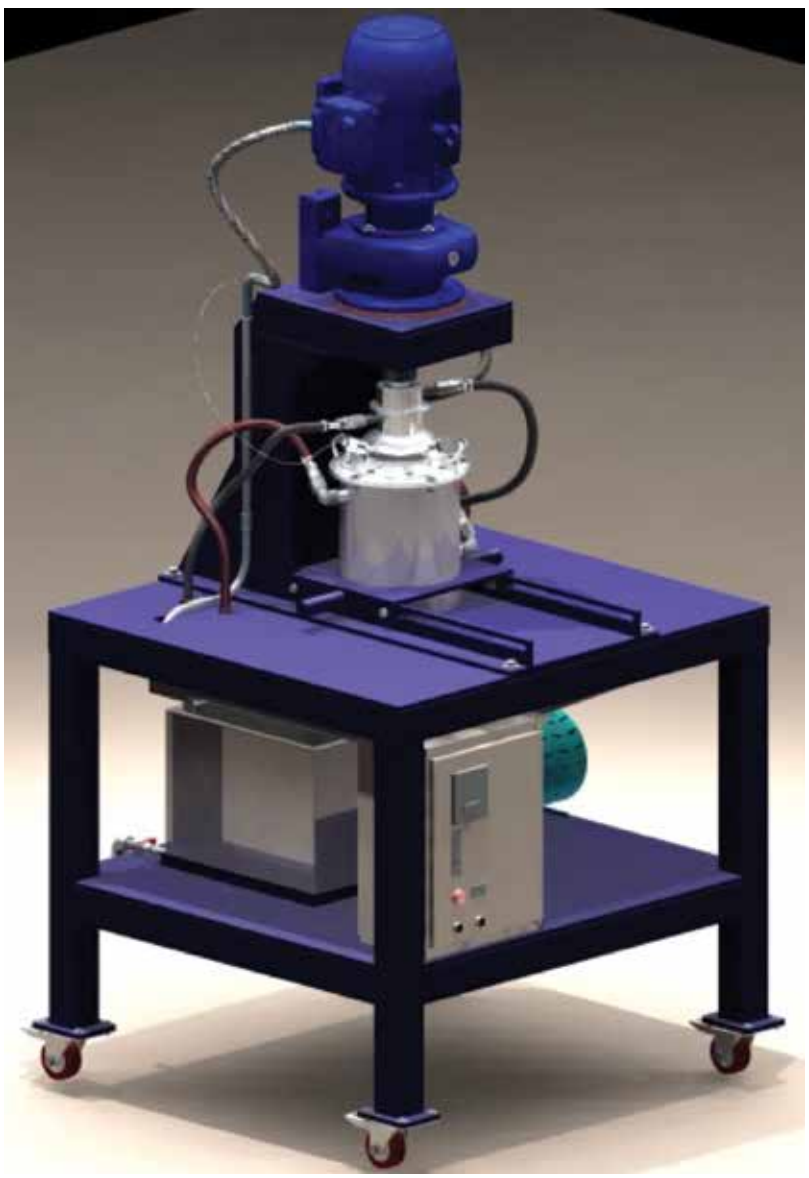

Figure 1. Attritor-type ball mill.

The mill also has a cooling system that allows the control of the internal temperature of the milling and a vacuum system with an Alcatel Adixen vacuum pump model 2005 SD for a vacuum pressure of 1 Pa and a 5.4 m^3/h flow. The alloy steel balls with a 10-mm-diameter were used. For more details of the design of the attritor mill, it is recommended to read Botero et al. [10].

For the milling 1-wet is called this way because 4% by weight of liquid ethanol was added as the process-controlling agent (PCA). The total amount of powders used in the milling was 500 and 20 g of ethanol (**Table 3**).

The M_{powder}/M_{balls} mass ratio determines the mass of balls that impact with regard to the mass of the powder material. At laboratory level, the recommended relationships [11] are between 10/1 and 20/1. For this milling, a ratio of 20/1 was selected, in order to have a greater amount of impact energy. Therefore, the mass of the balls (M_{balls}) is calculated as

$$\frac{M_{balls}}{M_{powder}} = \frac{20}{1} \Rightarrow M_{balls} = \frac{(2 \times 0.5\ \text{kg})}{1} = 10\ \text{kg} \tag{7}$$

For this milling, the agitator shaft speed was 250 rpm, the milling time was 5 h, and the process was conducted at an atmospheric pressure.

For the milling 2-wet, a total of 250 g of powder was used (**Table 4**); the most critical work parameters of the equipment were selected, in order to have the maximum available energy and ensure the formation of titanium carbide. Thus, 4% (10 g) by weight was added as the dispersing agent (PCA).

Material	Percentage (%)	Powders mass (g)
Titanium dioxide	62.47	312.35
Graphite	28.13	140.5
Aluminum	9.4	47.0
Total initial powder	100	500.0

Table 3. Amount and percentages of the initial powders of the wet grinding 1.

Material	Percentages (%)	Powders mass (g)
Titanium dioxide	62.47	156.2
Graphite	28.13	70.3
Aluminum	9.4	23.5
Total initial powder		250.0

Table 4. Amount and percentages of the initial powders of the wet grinding 2.

A mass ratio of 40/1 was used, for which a ball mass was obtained:

$$\frac{M_{balls}}{M_{powder}} = \frac{40}{1} \Rightarrow M_{balls} = \frac{(40 \times 0.5\ \text{kg})}{1} = 10\ \text{kg} \tag{8}$$

An agitator shaft speed of 300 rpm and a 7-h milling time at an atmospheric pressure was used.

For the milling 3-dry and vacuum, the amount of powder used in the milling was 250 g (**Table 5**). Aluminum powder was added in order to eliminate the formation of CO_2, to avoid the increase in pressure.

The mass ratio of 40/1 was used. For this case, the ball mass was

$$\frac{M_{balls}}{M_{powder}} = \frac{40}{1} \Rightarrow M_{balls} = \frac{(40 \times 0.25\ \text{kg})}{1} = 10\ \text{kg} \tag{9}$$

An agitator shaft speed of 500 rpm and a 12-h milling time were used, and the process was performed in vacuum. In this milling, ethanol was not added to the mixture as a dispersing agent.

From the initial millings, it was determined that the milling time had to be longer, in order to obtain higher concentrations of titanium carbide in the milling; this milling was named final milling. **Table 6** lists the parameters used in the milling.

2.3. Characterization of milling powders

The powders obtained from millings 1, 2, and 3 were characterized by X-ray diffraction with a Rigaku Rint 2200 diffractometer. The parameters used for X-ray diffraction analysis in millings 1 and 2 were 20 kW, 20 mAmp, and a sweep between 5 and 140° was performed with a scanning speed of 0.2 s/step. The parameters used for the analysis of milling 3 were 40 kW, 40 mAmp, a sweep between 10 and 100°, and a scanning speed of 2 s/step. For milling 3, three samples of material were taken in different parts of the milling container:

1. Sample 1: dust adhered to the milling spheres.
2. Sample 2: dust adhered to the walls of the bowl.
3. Sample 3: dust adhered to the bottom of the bowl.

Material	Percentage (%)	Powders mass (g)
Titanium dioxide	62.47	156.2
Graphite	28.13	70.3
Aluminum	9.4	23.5
Total initial powders	100	250

Table 5. Amount and percentages of the initial powders of the grinding 3, dry grinding, and vacuum grinding.

Process	Initial powders (g)	Temperature (°C)	Ratio $M_{balls}/M_{powders}$	Pressure (Torr)	Velocity (rpm)	Grinding time (h)
Grinding	169	38	40:1	1.7×10^{-2}	500	18
Grinding	169	38	40:1	1.7×10^{-2}	500	36

Table 6. Experimental process details of powders grinding.

The final milling was performed in a 36-h time; however, a stop of the process was made at 18 h to take a sample. For both cases, an X-ray analysis was performed, with a scanning speed between 1 and 5°/min, with a step of 0.020°, 40 kW, 40 mAmp, and a sweep between 10° and 100° (**Table 7**).

With the 36-h final milling powder, we proceeded to obtain three targets of 25.4-mm diameter, compacting and sintering them later (**Table 8**). In the compaction, a Carver hydraulic press with a maximum load capacity of 12 tons was used. A 10-ton load was applied for 3 min; in each process, the targets were between 4.5- and 6.5-mm thick.

The 5.0-mm thick target was divided into four parts in order to subject it to different sintering temperatures. The first part of the target and, according to the recommendations of Lü and Lai [12], the sample was put into the preheated oven at 700°C and kept at a sustained temperature for 1 h. After that, the oven was turned off and the material was let to cool down to room temperature inside the oven with the door closed. For the second part of the target, the process was repeated at a temperature of 1000°C. The two samples were then removed from the oven and a visual examination was performed.

Grinding	Composition	Abundance
18-h grinding	TiO_2	++
	TiC	+++
	SiO_3	+
	Al_2O_3	+
36-h grinding	TiO_2	++
	TiC	+++
	SiO_3	++
	Al_2O_3	+
	Fe	+

Convention: +++, abundant (>50%); ++, common (20–40%); ++, poor (10–20%); +, sparse (3–10%).

Table 7. Results of X-ray analysis.

Sample	Compacted mass material (g)	Targets thickness (mm)
1	10.015	6.5
2	7.751	5.0
3	5.952	4.5

Table 8. Compacted mass material and target thickness.

Scanning electron microscopy (SEM) (JSM-5910LV) tests were performed on the powder material with a 36-h milling time and the material sintered at 1000°C to determine size, distribution, particle shape, and local chemical composition.

3. Results

3.1. Millings 1 and 2: wet

The diffractograms of millings 1 and 2 (**Figure 2**) show the characteristic peaks of Rutile (TiO_2), in which 2θ is equal to 28, 36, 39, and 57° approximately, and it is presented as a tetragonal structure that indicates that the largest amount of powder corresponding to the initial material. The presence of characteristic graphite peaks with a hexagonal structure, in which 2θ is equal to approximately 24, 26, and 70°, is also observed. The most representative titanium carbide peaks have a cubic structure at approximate angles of 2θ that is equal to 36, 41, 61, 72, and 91°. Also, the characteristic peaks of aluminum (Al) of cubic structure in 2θ occurred, being equal to 9, 39, and 78° approximately. Alumina peaks (Al_2O_3) with a cubic structure at 2θ equal to 13, 21, and 50° also occurred.

The diffractograms for millings 1 and 2 (**Figure 2**) showed that small amounts of TiC were formed. Milling 2, with a more milling time (7 h) was the one that had the highest intensity TiC peaks, 146 a.u. approximately and at an angle of 2θ = 36°.

3.2. Milling 3: dry and vacuum

In the diffractograms (**Figure 3**), the characteristic peaks of the Rutile phase or titanium dioxide TiO_2, the titanium carbide (TiC), and the carbon for each of the samples are observed. The titanium carbide peaks, TiC, occur with their intensity maximums in 2θ equal to 36, 41, 60, 72, and 76°. With these peaks, it was evidenced that the highest intensity occurred at the angle of 2θ being equal to 36° in sample 1, with an approximate intensity of 247 a.u.

3.3. Final milling

The diffractogram for the powders with an 18-h milling time (**Figure 4**) shows characteristic peaks of rutile, titanium carbides, mica, and hydrated elements that facilitate the formation of hydrides and carbides. The characteristic peaks of titanium carbide (TiC) occurred with an intensity of 150 a.u. at 36°, but also at 2θ being equal to 41, 60, 72, and 76°.

For the 36-h milling time, the intensity of the characteristic peak of TiC at 36° increasing to 350 a.u. was observed (**Figure 5** and **Table 7**). Peaks at 2θ being equal to 41, 60, 72, and 76° were also diffracted, which were observed in the diffractogram for the 18-h milling.

As the milling time increased, the peaks of the X-ray diffractograms widened to twice their height, evidencing a process of internal stress accumulation.

In the sintering process, it was observed that the target subjected to a 700°C sintering temperature turned to a light gray color, and when trying to take it with the tweezers to remove it

http://dx.doi.org/10.5772/intechopen.76690

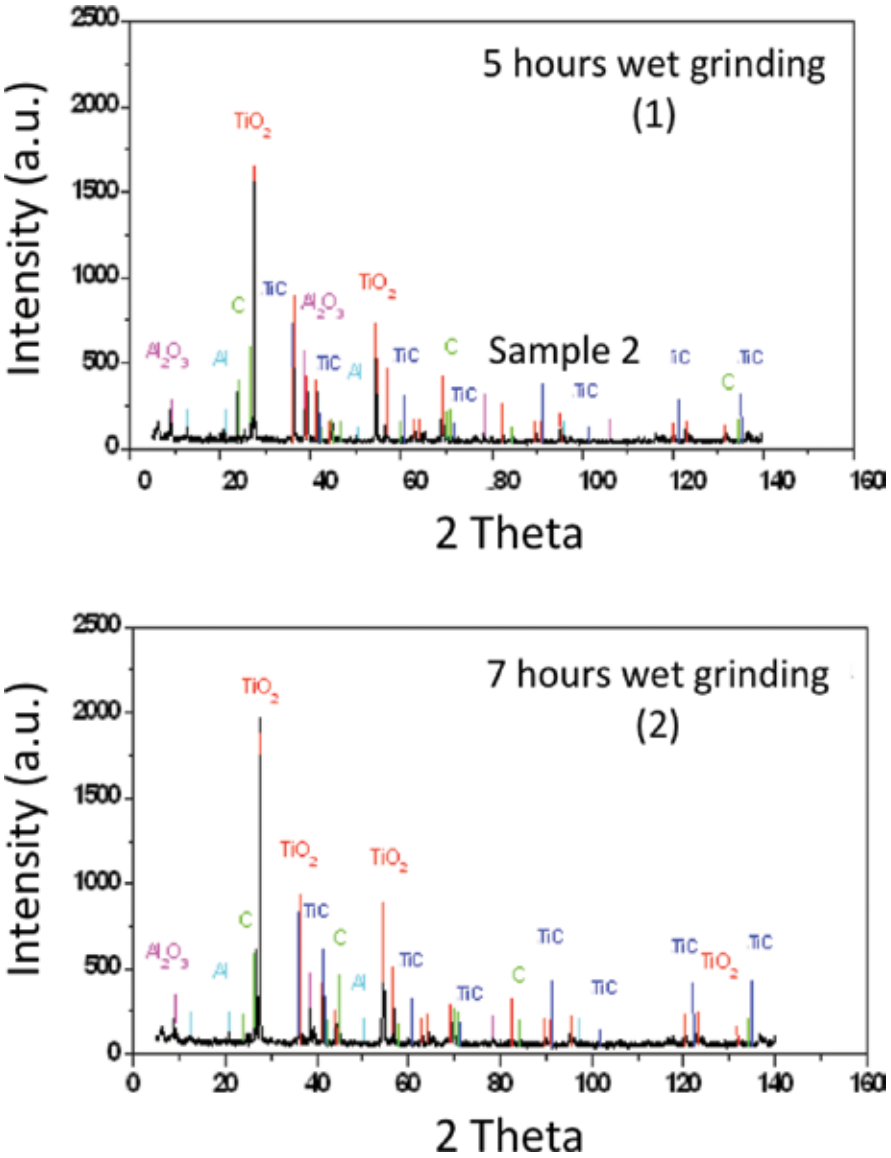

Figure 2. Diffractograms of millings 1 and 2.

from the oven, it fractured. This result shows that the material at this temperature did not sinter completely. The target subjected to a 1000°C temperature had a yellow color; this change in color is possibly due to the fact that, in the beginning, the pores are full of air, and as it was in oxidizing conditions, when opening the oven, it was discolored by the attack of oxygen on the surface [13]. This target showed a higher consistency than the sintering at 700°C.

In the micrographs (**Figure 6**) for the unsintered and 36-h milling time powders, the presence of two types of particles was observed; some of them had a spherical shape with an approximate

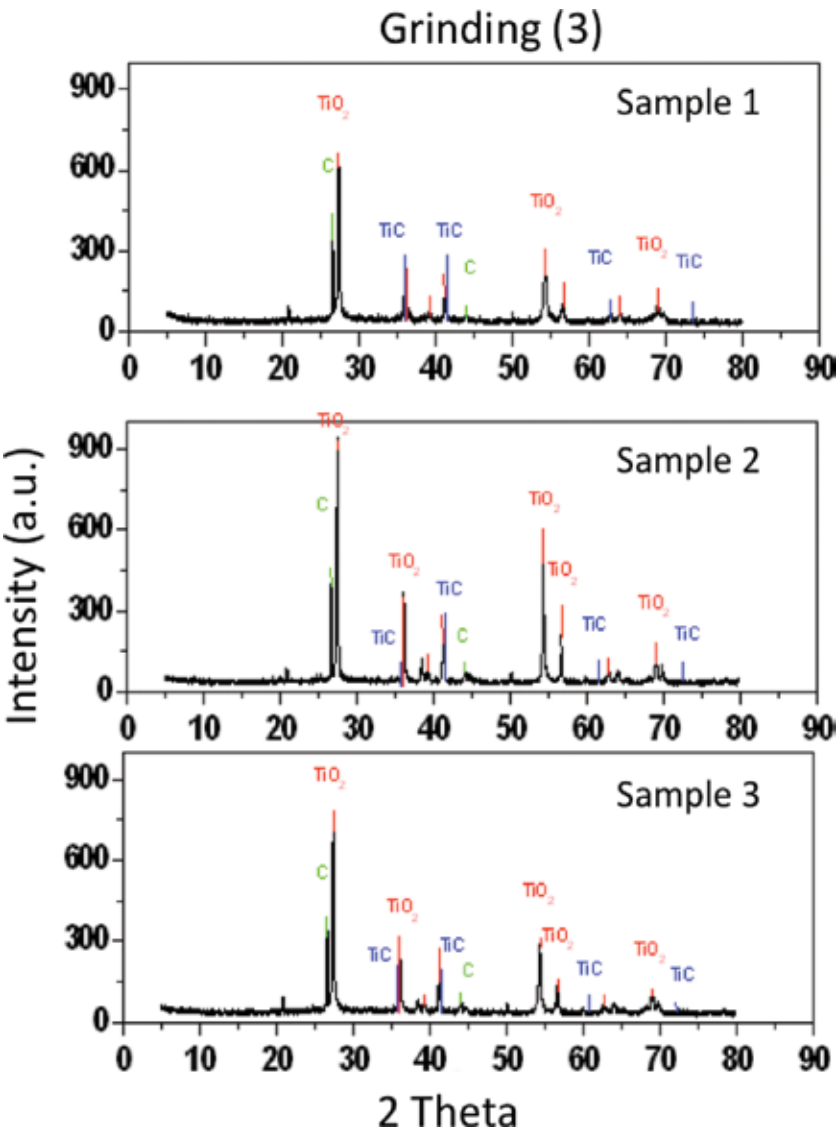

Figure 3. Diffractograms of dry and vacuum milling.

4-μm size (**Figure 6c**) and other particles of elongated shape of an approximate 1-μm size (**Figure 6e**). In general, it was found that the powders had an irregular particle size.

For the compacted and sintered material (36-h milling), a regular form of grain size was observed in the micrographs (**Figure 7**), with an average grain size of 5 μm (**Figure 7d**), and with a more regular particle size than the powder material. In the grain distribution, the growth of some grains can be seen at the expense of others, which means that a diffusion

http://dx.doi.org/10.5772/intechopen.76690

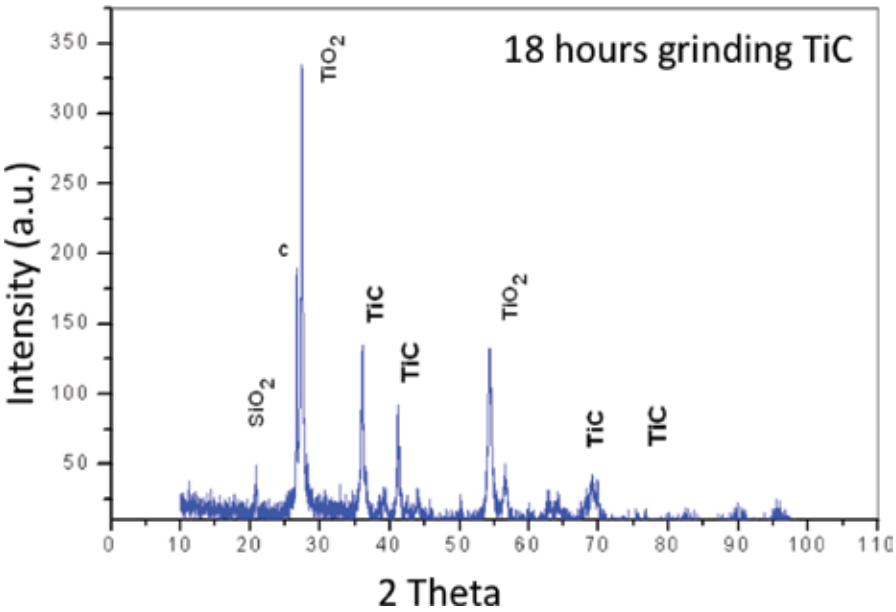

Figure 4. Diffractogram for the powders with an 18-h milling time.

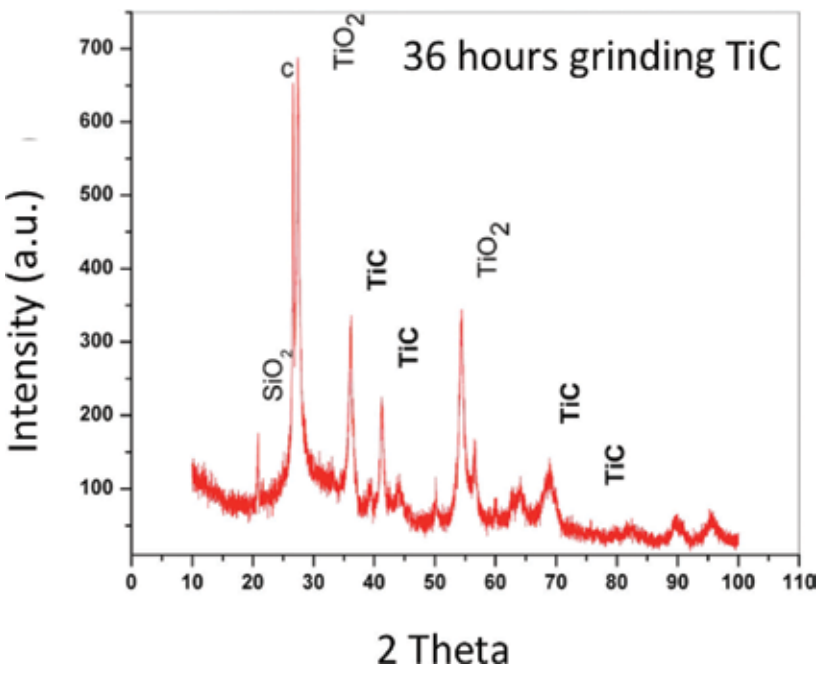

Figure 5. Diffractogram for the powders with a 36-h milling time.

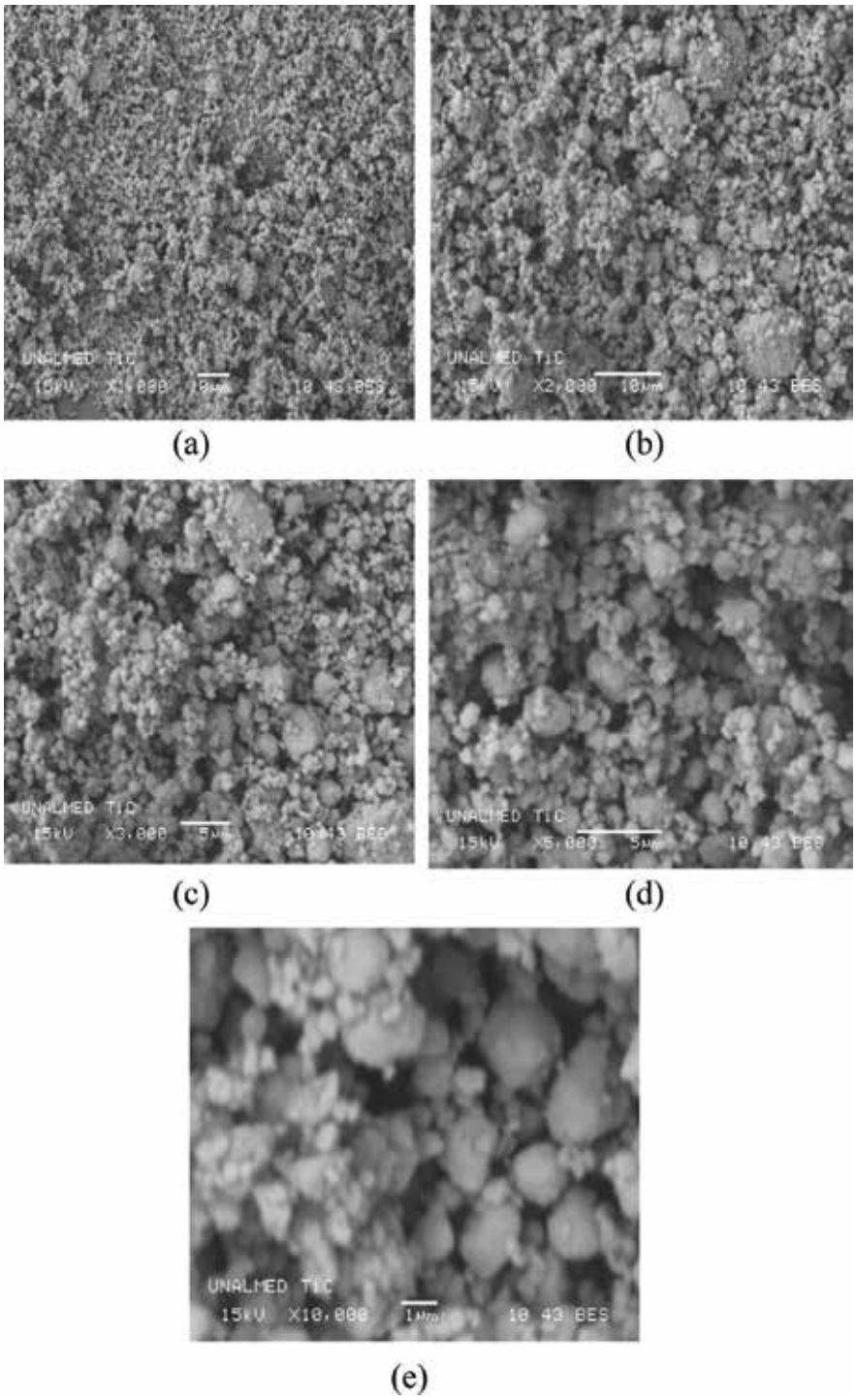

Figure 6. Micrographs for the unsintered and 36-h milling time powders: (a) 1000×, (b) 2000×, (c) 3000×, (d) 5000×, and (e) 10,000×.

http://dx.doi.org/10.5772/intechopen.76690

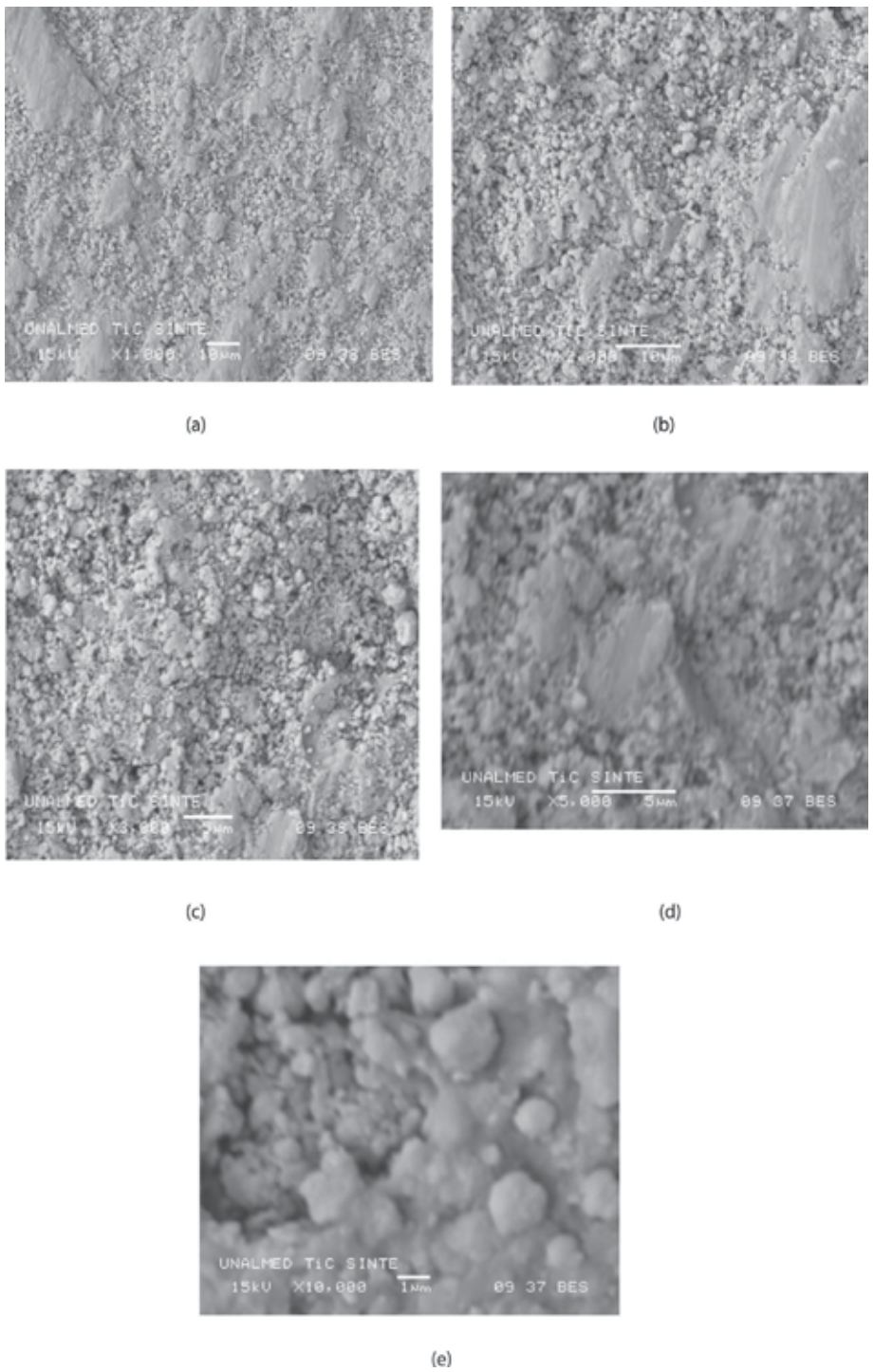

Figure 7. Micrographs for the compacted and sintered material (36-h milling): (a) 1000×, (b) 2000×, (c) 3000×, (d) 5000×, and (e) 10,000×.

process between particles occurred. The former issue showed that the 1000°C sintering favored the homogenization of grain size.

The chemical analysis performed on the powder material (36-h milling) showed the presence of elements such as silicon (Si), potassium (K), aluminum (Al), titanium (Ti), iron (Fe), and oxygen (O) (**Figure 8**). A high atomic percentage of oxygen and titanium was found (**Table 9**), which was followed by aluminum, silicon, and potassium.

For the sintered target (36-h milling), the chemical analysis (**Figure 9**) showed the presence of elements such as Al, Si, and Ti, which confirms the phases that were revealed in the X-ray diffractograms (**Figure 5**). Such present elements as calcium, potassium, and iron (**Table 10**)

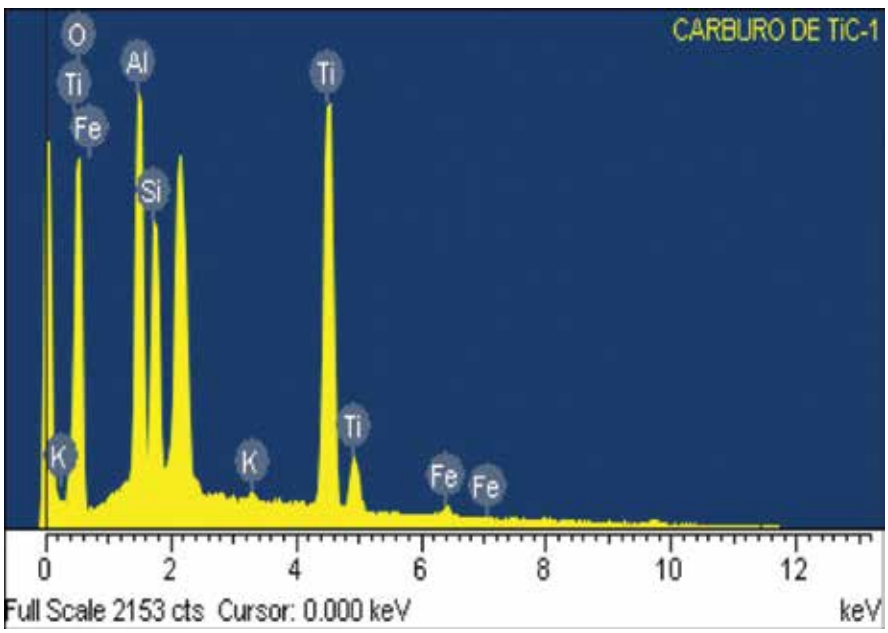

Figure 8. Scanning electron microscopy for the powder material (36-h milling).

Element	Weight (%)	Atomic (%)
O	45.89	67.14
Al	10.26	8.90
Si	7.62	6.35
K	0.33	0.20
Ti	34.00	16.62
Fe	1.90	0.80
Total	100.00	100.00

Table 9. Percentage of elements within the powders.

http://dx.doi.org/10.5772/intechopen.76690

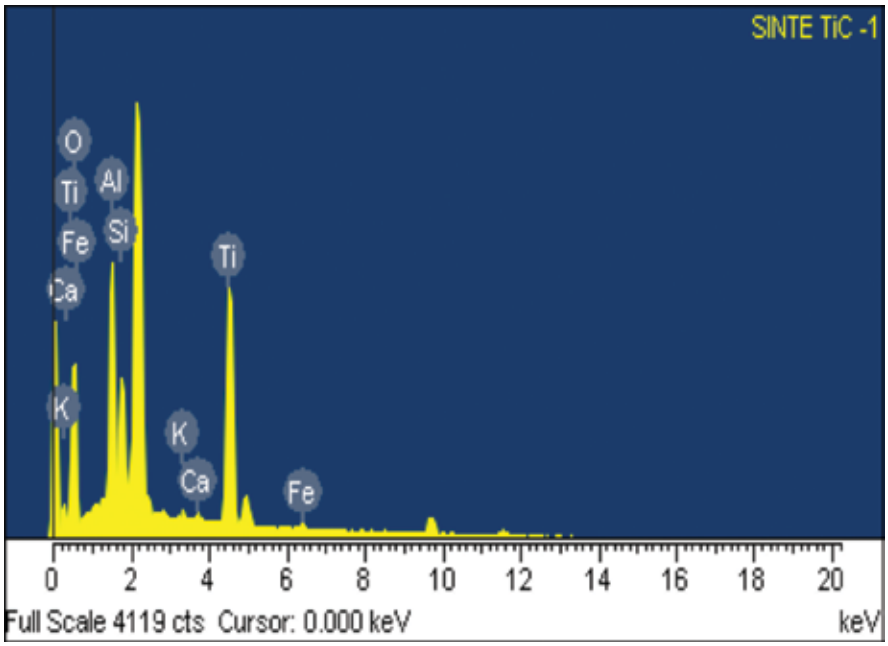

Figure 9. Scanning electron microscopy for the sintered target (36-h milling).

Element	Weight (%)	Atomic (%)
O	42.26	64.28
Al	11.61	10.39
Si	6.23	5.36
K	0.54	0.33
Ti	36.76	18.34
Fe	1.75	0.76
Ca	0.55	0.33
Total	100.00	100.00

Table 10. Percentage of elements within the sintered powders.

come from the material being found in the milling jars, as well as some impurities that the material absorbed during the sintering process.

4. Discussion

The presence of alumina in millings 1 and 2 means that the aluminum reacted with oxygen causing oxidation in the material and did not meet its main objective, which was to react with

titanium dioxide, to form titanium carbide, as was intended (Eq. (2)). The ethanol added to the mixture of millings 1 and 2, as dispersing liquid, added more oxygen to the material, making it difficult to extract the O_2 molecules from the titanium dioxide.

The highest concentration of TiC in milling 3 (sample 1), which corresponds to the powder adhered to the milling spheres, can be explained because, at this place, the highest impact energy occurs; consequently, the adhered material is in constant collision with all the parts that make up the milling bowl and this favors the creation of TiC.

The SEM micrographs of the 36-h milling powders showed a wide particle distribution, from about 200 nm through about 1 μm, while the sintered samples showed particles of spherical shape and regular distribution of grains with a size less than 5 μm. This grain distribution was produced by the growth of some grains at the expense of others, that is to say, a diffusion process occurred, and an effective sintering at a 1000°C temperature also took place.

5. Conclusions

The mechanosynthesis of titanium carbides was possible to be performed, and this is the main contribution of this research work, which uses the mechanical alloying technique from titanium dioxide, graphite, and commercial aluminum at a laboratory level.

In addition, it is necessary to highlight that the precursors being used in this process were very low cost, compared with the high-purity powders being normally used for this purpose.

Both issues open the possibility of implementing this method to obtain titanium carbides in a low-cost industrial process. Nevertheless, it is necessary to adjust the parameters of the milling process to produce TiC on an industrial scale.

Acknowledgements

This work was financed by Research and Technological Development Direction at Universidad Autónoma de Occidente, Cali, Colombia.

Author details

Héctor Enrique Jaramillo Suárez[1], Nelly Alba de Sanchez[1]* and Julian Arnaldo Avila Diaz[2]

*Address all correspondence to: nalba@uao.edu.co

1 Autónoma de Occidente University (UAO), Cali, Colombia

2 São Paulo State University (UNESP), São Paulo, Brazil

References

[1] Koch CC. The synthesis and structure of nanocrystalline materials produced by mechanical attrition: A review. Nanostructured Materials. 1993;**2**(2):109-129

[2] Murty BS, Ranganathan S. Novel materials synthesis by mechanical alloying/milling. International Materials Reviews. 1998;**43**(3):101-141

[3] DCNM by MA Techniques. New Materials by Mechanical Alloying Techniques. Oberursel: Ir Pubns Ltd; 1989

[4] Cahn RW. Materials Science and Technology, Processing of Metals and Alloys. Vol. 15. Weinheim: Wiley-VCH; 1996

[5] Zhang L, Shen H-F, Rong Y, Huang T-Y. Numerical simulation on solidification and thermal stress of continuous casting billet in mold based on meshless methods. Materials Science and Engineering: A. 2007;**466**(1):71-78

[6] Ye LL, Quan MX. Synthesis of nanocrystalline TiC powders by mechanical alloying. Nanostructured Materials. 1995;**5**(1):25-31

[7] Hack GAJ. Dispersion strengthened alloys for aerospace. Metals and Materials. 1987;**3**(457): 457-462

[8] Dossett JL, Luetje RE. Heat Treating: Proceedings of the 16th Conference. ASM International. OH, USA: ASM Press; 1996

[9] Froes FH, DeBarbadillo JJ. Structural Applications of Mechanical Alloying: Proceedings of an ASM International Conference; Myrtle Beach, South Carolina; 27-29 March 1990. ASM International; 1990

[10] Botero F, Torres JG, Jaramillo HE, de Sanchez NA, Sanchez SH. Diseño de un molino de bolas tipo atritor. Latin American Journal of Metallurgy and Materials. 2009;**S1**(4): 1423-1431

[11] El-Eskandarany MS. Mechanical Alloying: Nanotechnology, Materials Science and Powder Metallurgy. NY, USA: Elsevier Ltd; 2015

[12] Lü L, Lai MO. Mechanical Alloying. NY, USA: Springer Science & Business Media; 2013

[13] Angelo PC, Subramanian R. Powder Metallurgy: Science, Technology and Applications. New Delhi, India: PHI Learning Private Limited; 2008

Chapter 8

Powder Process with Photoresist for Ceramic Electronic Components

Minami Kaneko, Ken Saito and Fumio Uchikoba

Additional information is available at the end of the chapter

http://dx.doi.org/10.5772/intechopen.76881

Abstract

This chapter proposed a patterning process for ceramic electronic components. The proposed process uses a photoresist, and it is combined with the photolithography process and the printing process. By using both technologies, a high-aspect-ratio and fine conductive pattern is achieved because the patterned photoresist hold the filling paste during the dry process. Moreover, a different material pattern in a ceramic sheet can be formed simultaneously when the photoresist covers on the ceramic sheet with a through-hole pattern. The examples of the patterning process and the fabricated pattern are shown. The fine conductive pattern was formed by using a liquid photoresist, and the line width and the thickness were 10.3 and 1.85 μm, respectively. In the ceramic pattern, the conductive paste and low-temperature co-fired ceramic (LTCC) slurry were filled to the ferrite sheet. As a result, the ceramic sheet that had three different materials was achieved. It realizes the miniature ceramic inductor suppressing the minor loop. However, the photoresist process showed some problems with the fine pattern and the different material pattern. These problems are solved by adjusting the viscosity and the composite ratio of the slurry. The optimization of the type and thickness of the photoresist is required.

Keywords: photoresist, multilayer ceramic technology, fine conductive pattern, different material sheet

1. Introduction

Powder technology has been used as an industrial fabrication technology. For example, a metal powder combine with the binder or solvent, a conductive paste is achieved. Moreover, the conductive paste using the nanometer order metal powder realizes the low temperature fired. On the other hand, not only the metal material but also a ceramic material uses the powder

technology. The ceramic material is used for various fields. The most general product is a dinnerware. In addition, examples of being used as vehicle parts have also been reported because it is a high-temperature-tolerant material and it has a chemical resistance [1, 2]. Particularly, the ceramic material is paid attention as electronic components.

In the electronic components field, a miniaturization technology is an important factor. Communication devices such as a PC or smartphone have desired the miniaturization and a high functionalization. To miniaturize a device body, the miniature integrated components and the miniature control circuit are required. By realizing the miniature control system, many components and the large battery can set in the miniature communication devices. Moreover, the miniaturization of the control systems possible a low-loss system because circuits wire that connects to each electronic components become short length.

To achieve the miniature control system, the ceramic material is used for the integrated circuit (IC) packaging [3] and the miniature electronic components. The fine ceramic has some electronic characteristics. Ferrite ceramic shows magnetic characteristic, $BaTiO_3$ is ferroelectric ceramic, and Pb (ZrTi) O_3 is used as the piezoelectric ceramic. These ceramic materials support the miniaturization of passive components [4–8].

The conventional fabrication process of the ceramic passive components is the sheet process of the multi-layer ceramic technology [9]. The ceramic components are formed through a firing process. However, the fired ceramic is hard material and it is difficult for any processing. Therefore, it forms the ceramic sheet that is the mixture of the ceramic powder, a binder, and organic solvents, in the first step. The circuit wire patterns are printed on these sheets. After that, the printed sheets are stacked and laminated. In this process, the circuit patterns require a connection between an upper layer and a lower layer. The connection pattern is achieved by forming a through-hole pattern and filling the conductive paste at the printing process. The laminated ceramic sheets are dicing to the designed size, and then, the miniature multi-layer ceramic components are achieved by the firing process. The advantages of this technology are that the three-dimensional (3D) circuit pattern is realized inside the ceramic material, and the electronic characteristics can use for the components.

However, the conventional fabrication process has some problem for further miniaturization. The circuit pattern is formed by a screen printing process in general. This technology shows high productivity, it is suitable for the electronic components. The conductive pattern is made from a conductive paste and it is printed through a mesh pattern. The printed paste requires the leveling time for removing the mesh mark. It is the cause of a deformation of the conductive pattern. In the fine pattern, the adjacent conductors are connected and shorted. And then, to form a fine and high-aspect-ratio pattern is difficult.

Moreover, a high-functional device will be required, and a complex component that has various characteristics will be desired for the miniaturization. To achieve the complex component, the various materials are introduced. However, the conventional research of the different ceramic material pattern is inserting the ceramic sheet [10]. Therefore, it is difficult to form the one point different material pattern.

In this chapter, the photoresist process is proposed. It is possible to form the fine and high-aspect-ratio conductive pattern. The proposed process uses a photolithography process for the

patterning process, and printing process for the filling process is combined. The exposed and developed photoresist serves as a mask holding the paste. Moreover, this process is applied for forming the different material pattern. The example of the patterning process of the fine conductive pattern and the different ceramic material are shown with the fabricated pattern.

2. Photoresist process

In this chapter, the fabrication process for the ceramic electronic components is proposed. The multilayer ceramic technology is usually used for the fabrication process of the ceramic components, but it has some problems. Therefore, the photoresist process is proposed for the production process. The concept, base process and applications of the photoresist process as is following.

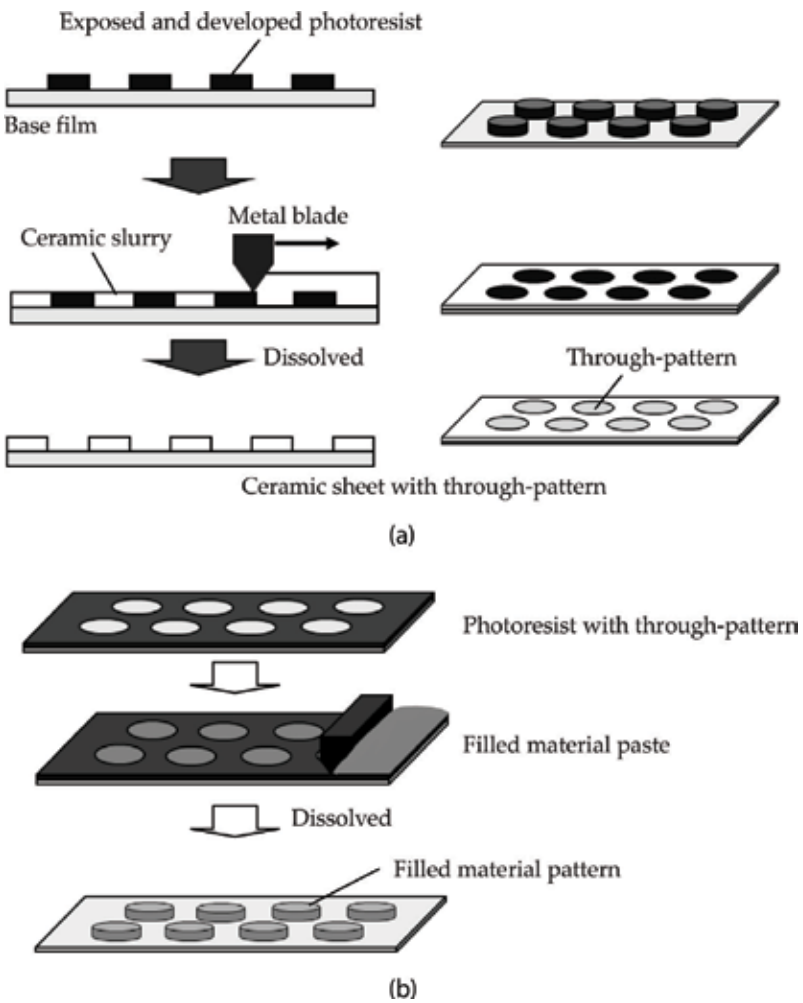

Figure 1. Schematic illustration of photoresist process (a) patterned ceramic sheet process, (b) patterning process.

2.1. Concept and base process of photoresist process

The proposed process uses the photoresist pattern. The first step, the photoresist is exposed for forming the designed pattern. The sacrifice patterns of the photoresist are obtained after development. In a case of a ceramic sheet with a through-pattern, the green sheet of the base material is formed using the doctor blade. At the time, the gap between the blade and the surface of the resist film is adjusted to zero. Therefore, the slurry fills surrounding the sacrifice pattern. Then, the specimens are dried. After the sacrifice pattern is dissolved, the green sheet of the base material with the through-pattern is achieved. To form the pattern, the through-pattern is exposed and developed on the photoresist. The ceramic slurry or conductive paste is filled into the through-pattern, after the dissolving process, the ceramic pattern, or conductive pattern is achieved. **Figure 1** shows the schematic illustration of the process for producing the patterned different material into the green sheet.

A liquid type photoresist and a film type photoresist are chosen for the achieved pattern. For a fine pattern, the liquid type photoresist is used. And then, the film type photoresist is employed for forming the sheet pattern because it realizes the uniform thickness. In this chapter, the different pattern process uses the film type photoresist, and the fine conductive pattern uses the liquid type.

The advantage of this process is that it uses a photolithography process. The photolithography process is used for the IC or microelectromechanical systems (MEMS) sensor fabrication process. Both products have a fine conductive pattern and miniature structure. Therefore, the proposed process that uses the photolithography process is suitable to miniaturize. Moreover, the flexible pattern designing is possible. In addition, the sacrifice resist pattern forms the through-hole pattern. On the other hand, it is a mask pattern that covered on the ceramic sheet. The photoresist mask pattern holds the filling paste as the ceramic slurry or conductive paste. It is possible to form the high-aspect-ratio pattern. These characteristics are used for the production process of the miniature ceramic components.

3. Fine conductive patterning process

The fine conductive pattern is desired for miniature electronic elements, a packaging ceramic, an interposer, and the furthermore. In the conventional process for forming the fine pattern, a vacuum process is used. However, this process has the issue that required the high fabrication cost and the extensive system. Therefore, the researcher focuses on the printed electronics. The screen printing process has been used for the ceramic electronic components already, and then, the gravure printing and ink-jet printing are introduced. However, it is difficult to realize the fine pattern and the low fabrication cost simultaneously only the printing technology. Therefore, the references the line widths of the fine pattern in the production and in the research field are 50 and 10–30 μm, respectively.

The proposed photoresist process can form the fine pattern by the simplified process that combined the photolithography process with the printing process. The fabrication process was base photoresist process (**Figure 1**), and a specific process is shown in **Figure 2**. For the fine pattern, liquid type photoresist was coated on a glass substrate. The designed line and

http://dx.doi.org/10.5772/intechopen.76881

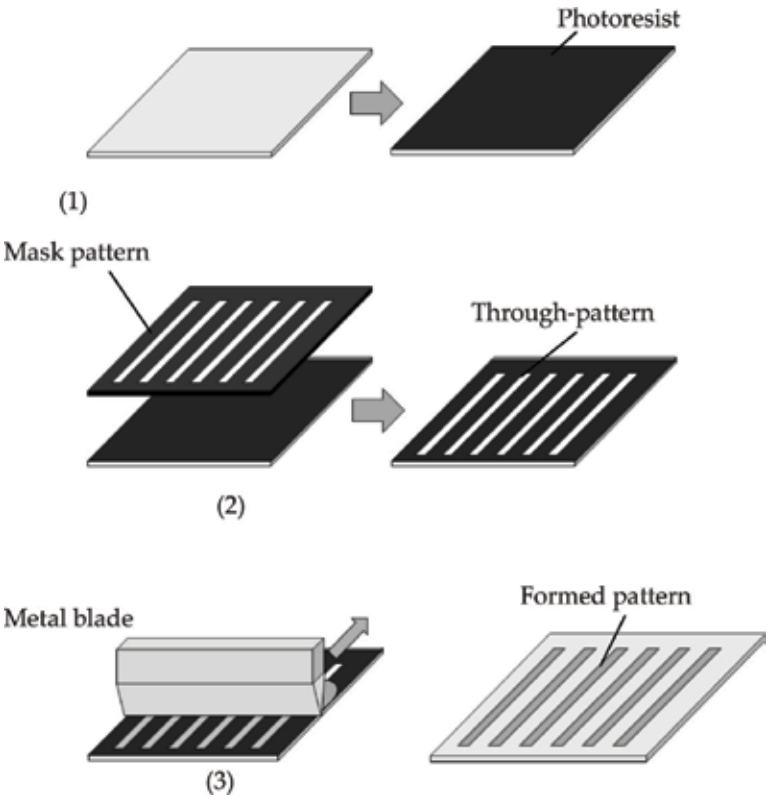

Figure 2. Fabrication process of fine conductive pattern. (1) glass substrate is coated with liquid type photoresist. (2) exposed and developed. (3) filled paste and dissolved.

space were 10 μm, respectively. The conductive paste that combined with microparticle metal powder (under 0.1 μm) was used. The filled conductive paste was dried on the hot plate keeping 60°. After that, the photoresist pattern was removed by remover.

The low viscosity paste was required for form the fine pattern, the photoresist pattern held the paste at the drying process. It can form the high-aspect-ratio pattern. The developed photoresist pattern and the conductive pattern on the glass substrate are shown in **Figures 3** and **4**.

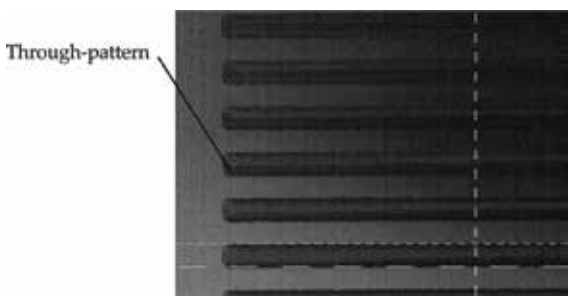

Figure 3. Patterned liquid type photoresist for fine conductive pattern.

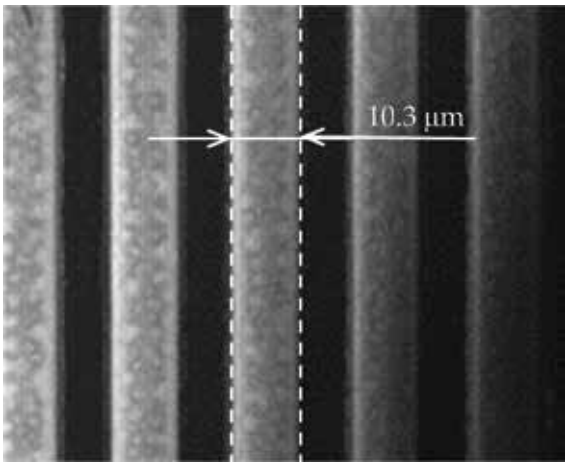

Figure 4. Formed fine conductive pattern.

These images were observed by the confocal microscope. The filling process was metal blade method. A pore and a crack were not shown on the surface of the conductive pattern, and the paste was filled completely. The width and height of the pattern were 10.3 and 1.85°μm, respectively. The fine and high-aspect-ratio pattern was achieved. However, a thin-film conductor around the line pattern was observed. It is a residual conductive paste that was coated on the resist pattern. When the conductive paste was filled, the gap between the metal blade and the resist pattern was occurred. And then, the dried paste on the resist remained with the side of the pattern. The schematic illustration of the mechanism of the residual pattern is shown in **Figure 5**. 3D measuring result of the conductive pattern using same fabrication process is shown in **Figure 6**. The side of the conductor formed the thin pattern. It is solved by adjusting the gap between the blade and the resist surface.

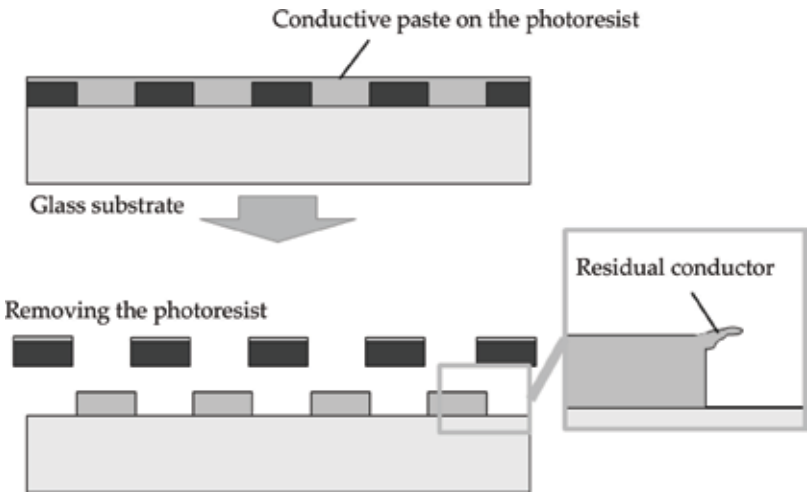

Figure 5. Schematic illustration of mechanism of residual pattern.

http://dx.doi.org/10.5772/intechopen.76881

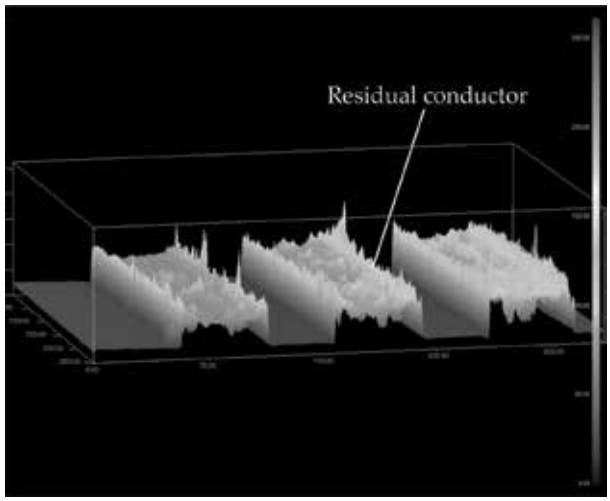

Figure 6. 3D measuring result of conductive pattern by photoresist process.

4. Different material patterning process

The different material patterning process can form some material patterns in one ceramic sheet without bump structure. The ceramic material is often used for the module circuit [11]. When the different ceramic materials are used, the module circuit with some electronic characteristics is realized. When the ceramic material and the conductive material are used, the conductive circuit pattern with high-aspect-ratio pattern and the flat surface pattern. **Figure 7** shows the patterning

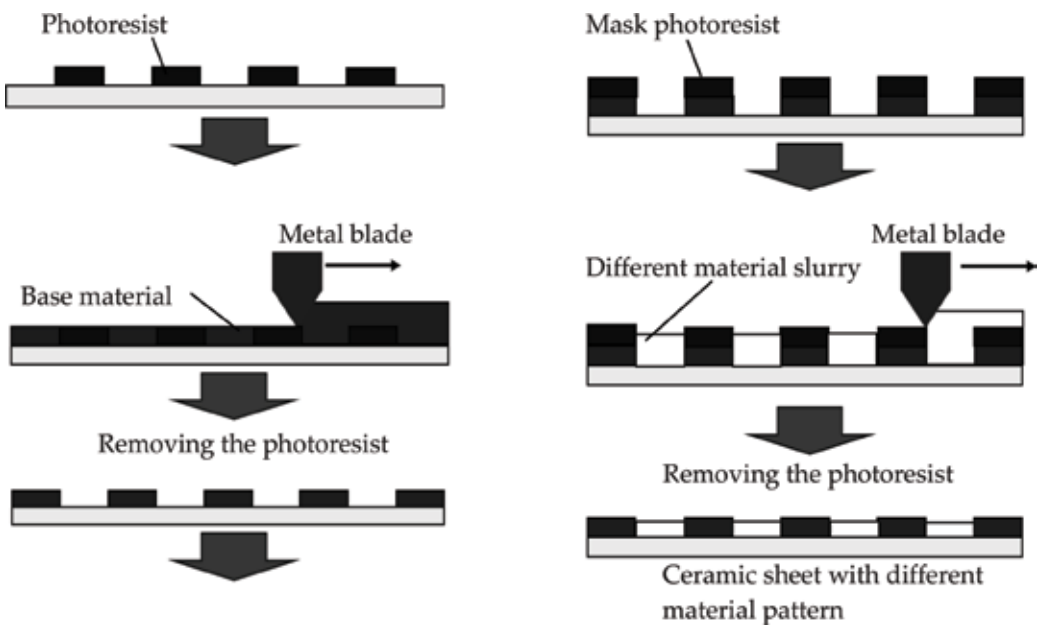

Figure 7. Schematic illustration of photoresist process for different material pattern.

process of the different material pattern. The first material sheet is formed by the base photoresist process. The ceramic sheet with the through-pattern is achieved. Another photoresist is prepared for covering the patterned ceramic sheet. In this time, the film type photoresist is used. The reversal pattern is exposed on the film type photoresist film, and then, the developed film is used for the mask film. The formed mask photoresist is laminated on the ceramic sheet with an alignment pattern. The different ceramic material slurry is filled in the only through-pattern because the first ceramic sheet is covered. After drying the sheet and removing the mask photoresist, the ceramic sheet with the patterned different material is achieved.

In the conventional patterning process for the different material, the pattern forms on the ceramic base sheet. **Figure 8** shows the schematic illustration of the conventional different pattern processing. Each material sheet is stacked, and it is difficult to form the different ceramic material pattern in the same ceramic sheet.

The proposed process for the different material pattern will be applied to a multilayer ferrite inductor. In the conventional multilayer ferrite inductor, the minor magnetic loop causes the degradation of the inductance and the Q factor because the ferrite magnetic ceramic covered around the internal conductor. When the nonmagnetic ceramic is inserted between the conductors of each layer, it is possible to suppress the minor magnetic loop. The mechanism of the minor loop and suppressing pattern is shown in **Figure 9**. The image of the minor loop suppressing multilayer inductor is shown in **Figure 10**.

Examples of the designed different material pattern with the photoresist process are shown in **Figure 11**. This design includes the different ceramic material pattern. The base material was the magnetic material and the patterned material was nonmagnetic material. The film type photoresist was used to form a thick pattern. The thickness of the photoresist film for the through-pattern was 90 μm and the mask film was 35 μm, respectively. The photoresist films were attached to the poly ethylene terephthalate (PET) carrier film.

The co-fired NiCuZn ferrite was used for the magnetic material. The start materials of the ferrite powder were NiO, ZnO, CuO, and Fe_2O_3 and the molecular ratio was 8.8–32–10–49.2, respectively. The particle diameter of ferrite powder was about 300 nm. low-temperature co-fired

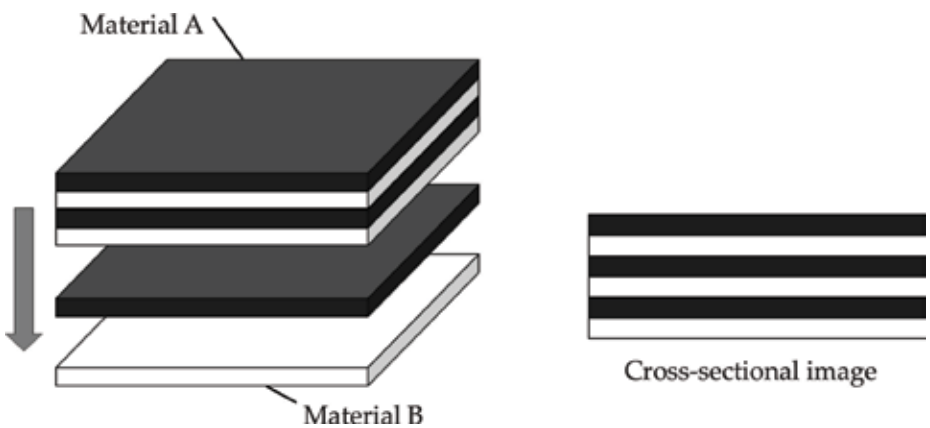

Figure 8. Conventional process to introduce a different ceramic material.

http://dx.doi.org/10.5772/intechopen.76881

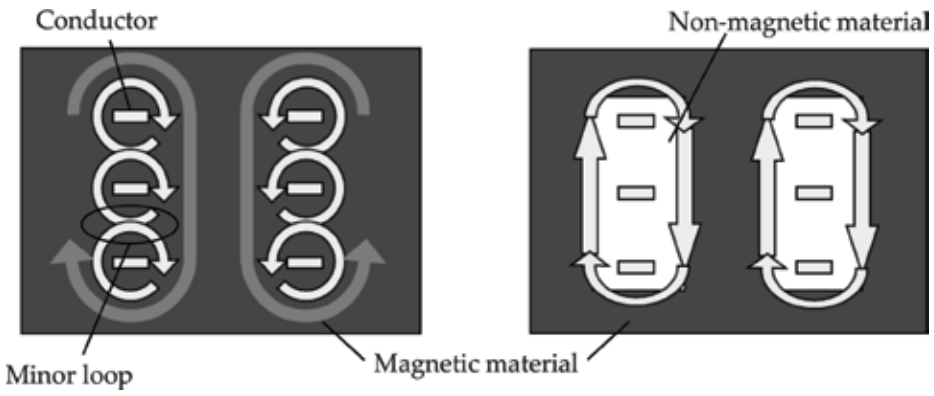

Figure 9. Mechanism of minor loop and suppressing pattern.

ceramic (LTCC) is mixed powder of a glass and an alumina ceramic, and it was used for the nonmagnetic pattern. The composite weight ratio of the glass powder and the alumina powder in the glass alumina composite material was 63 and 37. The glass powder was composed of $SrO\text{-}B_2O_3\text{-}Al_2O_3\text{-}SiO_2$. The particle diameter of LTCC powder 1 μm. The ceramic slurry of ferrite and LTCC was the mixture of the organic solvents and some additives. The composite material and composite weight ratio of each ceramic are shown in **Table 1**.

The microscope image of the fabricated LTCC pattern is shown in **Figure 12**. The complex pattern was shaped, and the different material slurry filled completely.

To achieve the suppressing inductor, the conductive pattern was formed by the photoresist process on the LTCC as the nonmagnetic material pattern. The fabrication process is shown

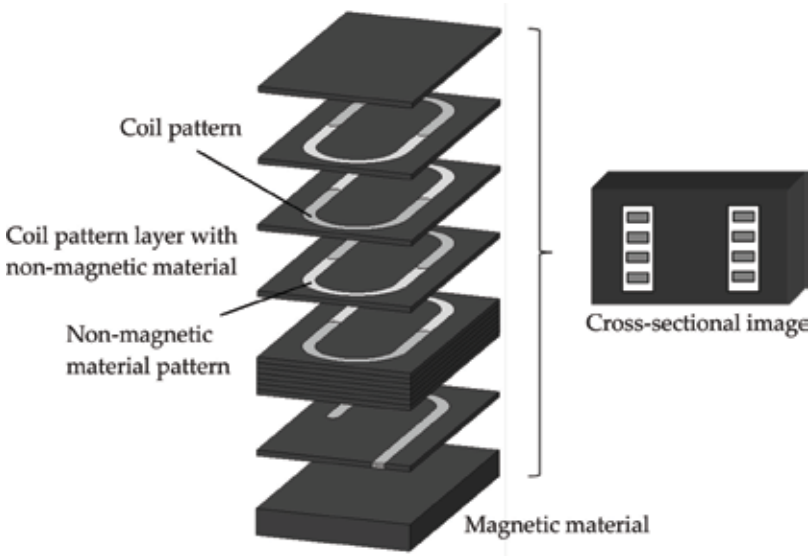

Figure 10. Image of minor loop suppressing multilayer ceramic inductor.

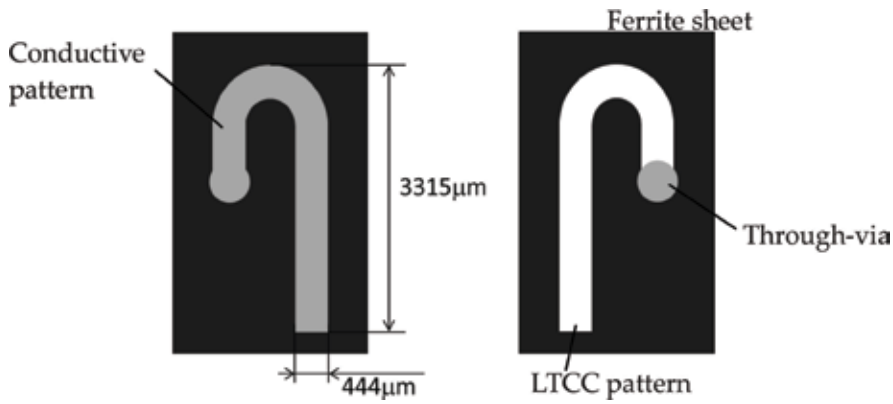

Figure 11. Designed different material patterns.

Material	Ferrite	LTCC
Ceramic powder	100	100
Binder	7	5
Dispersing agent	5	2.9
Plasticizer	1	1.3
Toluene	23	23
Xylene	23	23
Isopropyl alcohol	23	23

Table 1. Composition weight ratio of ceramic slurry.

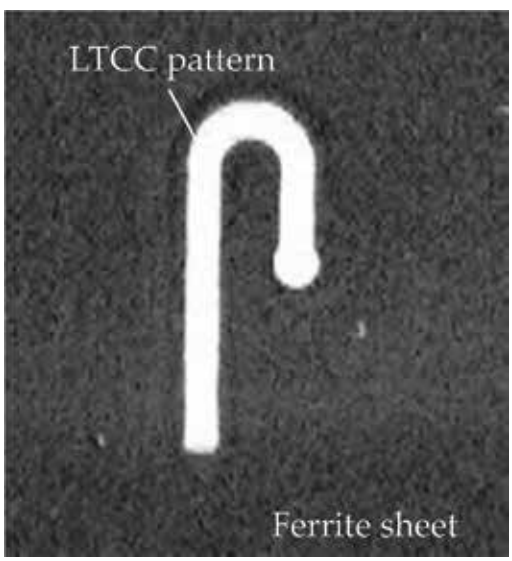

Figure 12. Microscope image of fabricated LTCC patterns on ferrite ceramic sheet.

in **Figure 13**. In this process, the through-hole to connect the circuit pattern on each layer was formed mechanically. The microscope image of the formed ceramic sheet is shown in **Figure 14**. The conductive pattern was formed on the LTCC pattern, and the through-hole was achieved by filling the conductive paste. By this result, the two different material patterns were formed on the ferrite sheet. However, the LTCC pattern is observed around the conductive pattern.

For the different material patterning process, the viscosity of the material slurry and the shrinking process are an important factor. **Figure 15** shows the cross-sectional image of the ferrite sheet by the microscope, and the round bump is observed around the edge of through-pattern. It is because of the surface tensions of the slurry. The proposed process requires the drying process the filled slurry was shrunk during the drying and peeling off the photoresist film. In this time, the edge part formed the round bump shape. It is easy to peel the resist pattern, but the thickness of the dried sheet or patterns become a nonflat pattern. By this reason, the LTCC pattern between the conductor and the ferrite pattern was formed. It is required that the viscosity is adjusted for form a clear pattern. **Figure 16** shows a schematic illustration of the shrinking process.

Moreover, the thickness of the mask photoresist influences the surface of the fabricated pattern. In this case, a thin film resist was 15 μm, and a thick film resist was 35 μm. The cross-sectional image of the fabricated patterns by the scanning electron microscope is shown in **Figure 17(a)** and **(b)**.

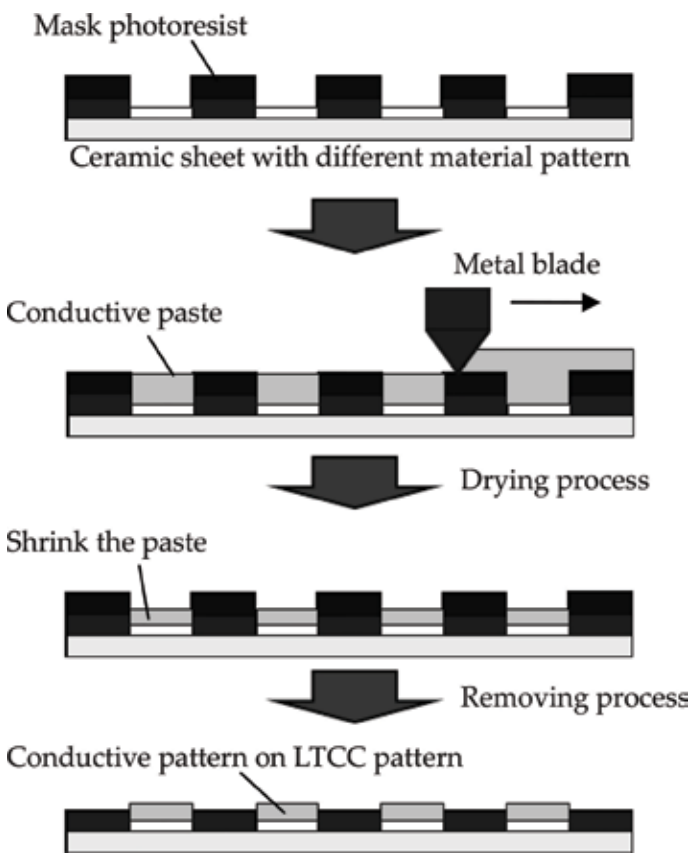

Figure 13. Fabrication process of filling conductive paste.

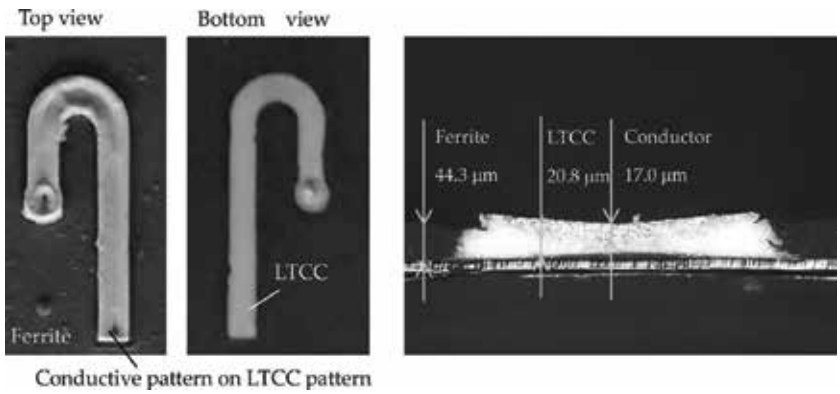

Figure 14. Microscope image of formed ferrite sheet with conductive pattern and LTCC pattern.

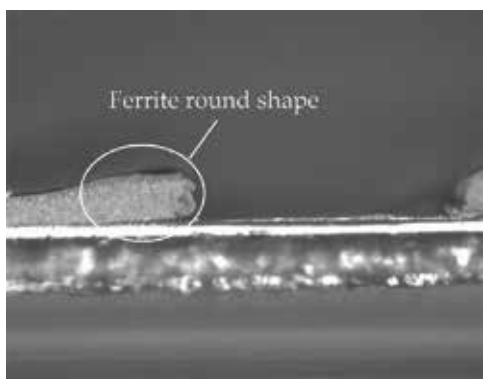

Figure 15. Cross-sectional image of fabricated ferrite sheet with through-pattern by microscope.

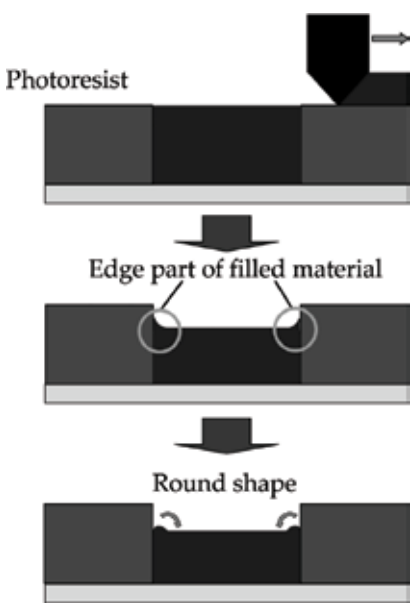

Figure 16. Schematic illustration of the shrinking process.

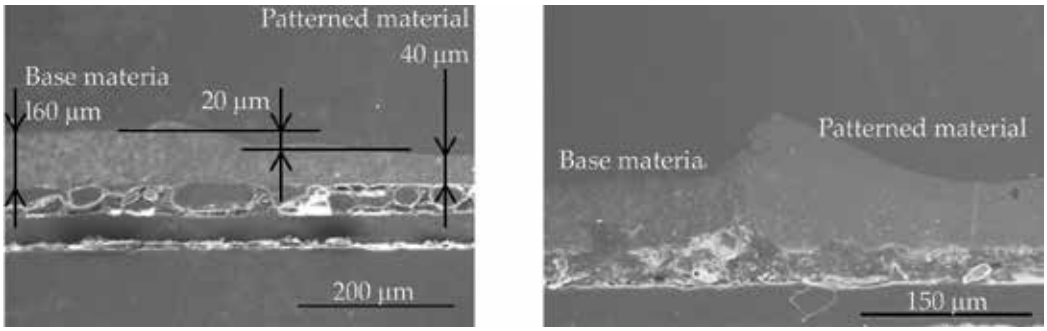

Figure 17. Cross-sectional image using each thickness mask photoresist film (a) 15 μm mask film, (b) 35 μm mask film.

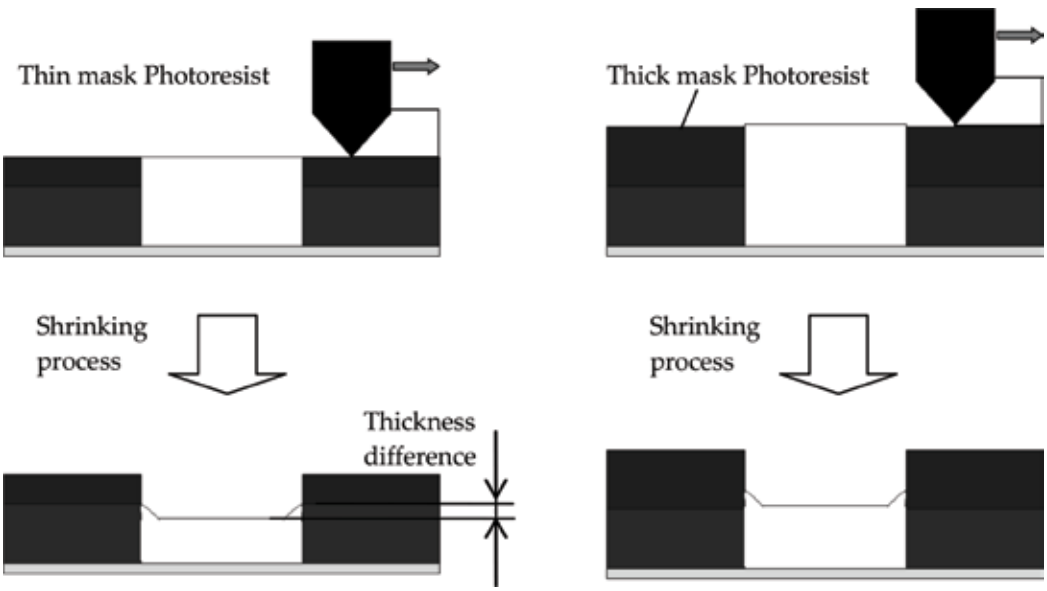

Figure 18. Schematic illustration of mechanism of the different thickness.

The result of using the thin mask resist showed the distance between the LTCC pattern surface and the ferrite pattern surface, and it was 20 μm. On the other hand, the flat surface of the different materials pattern was achieved by using the thick mask resist. The formed pattern showed the shrinking, the higher thickness than the base layer is required to hold the large volume of the filler material. The mechanism of the different thickness is shown in **Figure 18**.

5. Conclusions

In this chapter, the photoresist process was proposed. The proposed process is combined with the photolithography process and the printing process. The fine pattern for the conductor was formed by the photolithography process, because it is usually used for the production process of the IC. The printing process was used for the filling process as the conductive paste and the different material pattern.

The examples of the patterning process and the fabricated pattern were shown. In the conductor pattern, the fine pattern was formed, and the line width and thickness were 10.3 and 1.85 μm, respectively. The proposed process held the filled conductive pattern the high-aspect-ratio pattern was achieved. In the ceramic pattern, the ferrite ceramic sheet that had the LTCC pattern was achieved. It was realized by using the photoresist for the mask pattern. The fabricated pattern shaped complex pattern, and the LTCC was filled into the through-pattern on the ferrite sheet completely. Moreover, the conductive paste was filled with the LTCC pattern, and then, the ceramic sheet that had three different materials was achieved. By using the proposed process, it is possible to achieve the miniature multilayer ceramic inductor that suppresses the minor loop.

However, the patterning process combining the photoresist and material slurry showed some issues. The fabricated fine pattern was observed the thin-film conductor at the line edge. The fabricated different material pattern showed the round pattern. These problems can be solved by adjusting the viscosity and the composite ratio of the material slurry. In addition, the optimization of the type and thickness of the photoresist is required.

Acknowledgements

The sample of this study was fabricated by the facility at the Research Center for Micro Functional Devices, Nihon University. Part of this study was supported by the CST research project of Nihon University and by JSPS KAKENHI (16K18055).

Author details

Minami Kaneko*, Ken Saito and Fumio Uchikoba

*Address all correspondence to: takato@eme.cst.nihon-u.ac.jp

Department of Precision Machinery Engineering, Collage of Science and Technology, Nihon University, Chiba, Japan

References

[1] Okada A. Progress in automotive technology with ceramic materials. Japanese Journal of Ceramics Japan. 2012;**47**:398-405

[2] Okada A. Challenges of ceramics for structural application. Japanese Journal of Ceramics Japan. 2005;**40**:259-275

[3] Gongora-Rubio RM, Espinoza-Vallejos P, Sola-Laguna L, Santiago-Aviles JJ. Overview of low temperature co-fired ceramics tape technology for meso-system technology (MsST). Sensors and Actuators A: Physical. 2001;**89**:222-241

[4] Tamura T, Dohya A, Inoue. Combination of thick-film dielectric/thin film conductor for fine pat-tern formation of multilayer substrate. ElectroComponent Science and Technology. 1981;**8**:235-239

[5] Takahashi T, Takaya M. Laminated Electronics Parts and Process for Making the Same. US Patent No. 4322698. 1982

[6] Shimada Y, Utsumi K, Suzuki M, Takamizawa H, Nitta M, Watari T. Low firing temperature multilayer glass-ceramic substrate. IEEE Transaction on Components, Hybrids, and Manufacturing Technology. 1983;**CHMT-6**:382-388

[7] Bian JJ, Yu Q, He JJ. Tape casting and characterization of Li2.08TiO3-LiF glass free LTCC for microwave applications. Journal of the European Ceramic Society. 2017;**37**:647-653

[8] Baba Y, Higashiyama K, Segawa S, Ishida T, Nakatani S. Co-fireable copper multilayered ceramic substrates. In: Proceedings of Japan IEMT Symposium, Sixth IEEE/CHMT International Electronic Manufacturing Technology Symposium; 26-28 April 1989; Nara Japan. pp. 28-31

[9] Blodgett JA. A multilayer ceramic multi-Chip mod-ule. IEEE Transaction on Components, Hybrids, and Manufacturing Technology. 1980;**CHMT-3**:634-637

[10] Jao J-C, Li P, Wang S-F. Characterization of inductor with Ni–Zn–Cu ferrite embedded in B_2O_3–SiO_2 glass. Japanese Journal of Applied Physics. 2007;**46**:5792-5796

[11] Wang R, Lou R, Cheng K, Leung L, Lin J-R, Chung T. A compact 802.11b/g WLAN front-end module with integrated passive devices on modified ceramic substrate. Asia Pacific Microwave Conference (APMC); 7-10 December 2009; Singapore. 2009. pp. 1489-1492

Edited by Alberto Adriano Cavalheiro

Powder Technology comprehends several particulate solid systems, which must be controlled, from the nucleation stages to the final application of derivative materials. Powder characteristics depend on the synthesis method, which can be a simple solid-state reaction followed by attrition milling, mechanosynthesis, or chemical methods, such as the sol–gel method. Powder technology is an important interdisciplinary area, which can provide solutions to several application fields. The book *Powder Technology* contains several peer-reviewed chapters organized in two sections. Section 1 is focused on metal and composites powders and Section 2 contains chapters on non-metallic powders. I sincerely hope that the contents of this book will help in the dissemination of knowledge to researchers and students working with powder technology.

Published in London, UK

IntechOpen

ISBN 978-1-83881-681-0